THEORETICAL STUDIES OF WAVE INTERACTIONS IN THE SUN

A DISSERTATION
SUBMITTED TO THE DEPARTMENT OF MECHANICAL ENGINEERING
AND THE COMMITTEE ON GRADUATE STUDIES
OF STANFORD UNIVERSITY
IN PARTIAL FULFILLMENT OF THE REQUIREMENTS
FOR THE DEGREE OF
DOCTOR OF PHILOSOPHY

Shravan M. Hanasoge
September 2008

© Copyright by Shravan M. Hanasoge 2009
All Rights Reserved

I certify that I have read this dissertation and that, in my opinion, it is fully adequate in scope and quality as a dissertation for the degree of Doctor of Philosophy.

(Parviz Moin) Principal Adviser

I certify that I have read this dissertation and that, in my opinion, it is fully adequate in scope and quality as a dissertation for the degree of Doctor of Philosophy.

(Philip Scherrer)

I certify that I have read this dissertation and that, in my opinion, it is fully adequate in scope and quality as a dissertation for the degree of Doctor of Philosophy.

(Sanjiva Lele)

Approved for the University Committee on Graduate Studies.

Abstract

Direct observation of the solar subsurface is impossible due to the high degree of optical scattering by the partially ionized plasma that inhabits the near-surface layers of the Sun. The deepest part of the Sun visible to us, known as the photosphere (also the solar surface), appears as a roiling turbulent radiative magnetized convecting plasma. At first glance, it would seem therefore that subtle questions relating to the subsurface constitution of the Sun seem completely unanswerable and the interior properties unknowable. However, analogous to geoseismology, a great deal can be gleaned about the internal structure and dynamics of the Sun by carefully observing the waves that appear at the solar surface. This has been made possible over the last few decades through the development and application of powerful techniques of helioseismology which combine mathematical rigour and sophisticated guesswork. Analyses of the high quality observations made by the Michelson Doppler Imager (MDI) instrument onboard the Solar and Heliospheric Observatory (SOHO) satellite have led to continuous progress in our ability to infer subtle aspects of the recondite solar interior. This rush of discoveries has brought with it some skepticism and a need to determine whether the diagnostic agents, namely the waves, indeed behave as we expect them to. Moreover, it is instructive to develop an appreciation for the sensitivities of these waves to anomalies at various depths for it tells us what is detectable and how close we are to the detection.

Towards this goal, modeling wave behavior in the Sun using either numerical or analytical techniques is a useful way to proceed. Numerical methods are developed to simulate linear wave propagation in a solar-like stratified medium. Calculations

are performed in spherical and Cartesian geometry, where the former takes into account global, large wavelength, long lived waves and the latter, near-surface short wavelength, short lifetime waves. There are many numerical challenges encountered in these computations: steep density and pressure gradients, convective instabilities, aliasing, boundary conditions etc. that must be dealt with care. Since the problem is computationally intensive, the code is parallelized according to the Message Passing Interface (MPI) standard. Validation procedures to ensure that the reliability of the numerical algorithm are discussed in some detail. Results of analyses of helioseismology on this artificial data are reported and discussed.

The extent of the interaction of magnetic fields with waves is a leading question in helioseismology. Theoretical work that attempts to characterize and quantify these interactions provides a useful complement to the standard numerical approach invoked to address such problems. The Born approximation, a form of perturbation theory, is widely invoked in helioseismic inverse theory. We investigate the Born approximation in the context of magnetic fields and demonstrate its validity and determine the range of applicability. Of more involved theory is the estimation of the wave scattering matrix associated with a thin flux tube embedded in a solar-like medium. Evanescent waves known as jacket modes, which appear due the mathematical incompleteness of the set of resonant mode eigenfunctions are shown to be quite essential in calculating the extent of scatter in the wavefield.

Acknowledgements

It has been my privelege to work with the SOI group. I am thankful to Phil Scherrer for his continual support and guidance over the course of these somewhat drama-filled years. Tom Duvall, my advisor, has been a mentor non-pareil; I thank him for all that he has taught me about helioseismology and the scientific method in general. The many speculative excursions in the realm of helioseismology that we undertook have been a constant source of intellectual stimulation. Jesper Schou, with whom I am yet to climb a mountain, has contributed much toward making my time at Stanford fun; our many discussions relating to the Sun, science, politics, mountains, and gossip have been thoroughly entertaining. Many thanks to Rasmus Larsen, who showed me how enjoyable scientific computing could be. The inimitable Sébastien Couvidat, who added colour, great amusement, and a healthy dose of impropriety to life at SOI, has made getting here that much easier. Sébastien, Rajaguru, and Richard have taught me a good deal of solar physics; in particular, I thank them for the entertaining lunches that we have shared. In more ways than one, Prof. Parviz Moin made all of this possible; I am very thankful for his support and generosity at the crucial junctures. The many discussions with Prof. Sanjiva Lele greatly helped in clarifying several numerical and physical aspects of my work.

My life here would have been entirely incomplete were it not for close friends and good room-mates: Dev, Anderson, Gandalf, Rap, Anant, the Chain, Rob, K, Nolan, Neel, Vijay, Veronica, Shonali, Sylvia, Aaron, Filip, Namita, and Josh. Lastly, none of this would have been possible without the encouragement and support of my parents, to whom I extend a sense of deep gratitude.

Contents

Abstract v

Acknowledgements vii

1 Introduction 1

1.1 Time-distance helioseismology 4

1.2 Magnetic field interactions 6

1.3 The Forward method 7

1.4 Results Contained in This Work 9

2 Computations in spherical geometry 11

2.1 Introduction 11

2.2 The problem definition 13

2.3 Numerical method 15

2.3.1 Parallelism in OpenMP 15

2.3.2 Parallelism according to message passing 16

2.4 Acoustic wave propagation in the sun 17

2.4.1 Upper turning point: reflection at the surface 18

2.5 Computational issues 19

2.5.1 Choice of radial grid 19

2.5.2 Spectral blocking and radial dealiasing 24

2.5.3 CFL restrictions 25

2.5.4 Lower boundary issues 28

2.5.5 Buffer layer 28

2.5.6 Convective instabilities 29
2.6 Validation 31
2.6.1 ADIPACK 34
2.6.2 Shifts in frequencies due to rotation 34
2.7 Results and analyses 37
2.7.1 Travel times 37
2.7.2 Correlations 38
2.7.3 Line Asymmetry 38
2.8 Detectability of interior convection 40
2.9 Ray calculations 43
2.9.1 Deep convection model 43
2.9.2 Surface convection model 43
2.9.3 Travel times 45
2.9.4 Correlations 47
2.10 Summary and Conclusions 49

3 Near-surface oscillations **51**
3.1 Introduction 51
3.2 The Simulation 53
3.2.1 Numerical Algorithm 56
3.2.2 Power Spectrum 57
3.3 Noise Subtraction 57
3.4 Travel times with Surface Focusing 61
3.4.1 Results 62
3.4.2 Validation 64
3.5 Kernels 65
3.5.1 Source Kernels 68
3.5.2 Sound-Speed Kernels 71
3.6 Conclusions 73

4 The Born approximation for magnetic fields **76**
4.1 Introduction 76

4.2 The Problem . . . 78
4.2.1 Governing equations . . . 78
4.2.2 Steady background state . . . 78
4.2.3 Linear waves . . . 79
4.3 Exact Solution . . . 80
4.4 First Born approximation . . . 82
4.5 Born tends to the exact solution as $\epsilon \to 0$ . . . 86
4.6 Travel Times . . . 89
4.7 Discussion . . . 91

5 Scattering by a flux tube **95**
5.1 Introduction . . . 95
5.2 The model . . . 97
5.2.1 Flux tube . . . 98
5.2.2 Oscillations of the tube: the kink mode . . . 99
5.2.3 Jacket modes and a lower boundary . . . 99
5.2.4 The tube boundary . . . 100
5.3 Solution procedure . . . 102
5.4 Comparison . . . 104
5.5 Discussion . . . 104

6 Concluding remarks **110**
6.1 Forward modeling and helioseismology . . . 111
6.2 Magnetic field effects . . . 113

A Altering the background state **114**

B Code verification **116**
B.0.1 Eigenfunctions . . . 119
B.0.2 Efficacy of the transmitting boundary . . . 123
B.0.3 Evanescent behaviour . . . 125
B.0.4 Spherical Harmonics and the optimized R-K scheme . . . 132

B.0.5 Measuring reflection phases 133

C Kernels and Phase speeds **138**

C.1 Scaling Kernels 138

C.2 Phase Speeds 139

D The scattering coefficients **141**

D.1 Exact solution coefficients 141

D.2 Useful Integrals 141

D.3 Born approximation coefficients 142

E Eigenvalues **143**

E.1 Jacket mode eigenvalues 143

E.2 p-mode eigenvalues 144

List of Tables

5.1 Scattering coefficients 103

C.1 Annuli and Phase-Speed Filter Parameters 140

List of Figures

1.1 The Doppler velocity power spectrum of the Sun as observed by the MDI instrument. The lower horizontal axis is the spherical harmonic degree, l, an alternate measure of the wavelength of the wave, shown on the upper part of the graph as λ_b. The wavelength is expressed in Megameters while l is non-dimensional. The vertical axis is the frequency expressed in milli Hertz. Courtesy: the Solar Oscillations Investigation team. 3

1.2 A time-distance diagram obtained by analyzing MDI data (Duvall et al., 1997). The ridges seen in the figure correspond to the time (on the vertical axis) taken by wave packets to travel the distance (in degrees) shown on the horizontal axis. The wave packet structure is contained in the ridges. 5

2.1 Background properties from model S of the sun (Christensen-Dalsgaard et al., 1996) as functions of radius. The horizontal coordinate of all the panels above is the fractional radius, $r/R_\odot$. Panel (a) shows the dependence of sound speed (in $\mathrm{km \cdot s^{-1}}$) with $r/R_\odot$. Panel (b) contains the fractional pressure scale height variation ($H_p/R_\odot$; H_p has been defined in Eq. [2.12]) with the fractional radius. Note the rapidly decreasing scale height in the near-surface layers. Panel (c) and (d) show logarithmic variations in density and pressure as a function of the fractional radius. 20

2.2 Acoustic cutoff frequency $\omega_A/2\pi$ as a function of radius in the model. The steep rise in ω_A in the near-surface layers is due to rapid changes in the density scale height, and causes outward-propagating waves with frequencies $\omega < \omega_A$ to reflect and propagate inward. 21

2.3 Fractional grid spacing as a function of radius for $n_{rad} = 350$. Plotted is $dr/R_\odot$, where dr is the local grid spacing, as a function of the fractional radius, $r/R_\odot$. For $r \leq 0.99R_\odot$, the grid spacing is chosen to maintain the constancy of the travel time of an acoustic wave between adjacent grid points. To account for rapidly decreasing scale heights, the radial grid points from $0.9915R_\odot$ to the upper boundary are equally spaced in $\ln p$. Third order splines are used to vary the grid spacing between 0.99 and $0.9915R_\odot$ as smoothly as possible. 22

2.4 Spectral blocking in a linear simulation. This is a classic malaise affecting non-linear calculations, resulting in aphysical energy accumulation near and at the Nyquist. Although the amplitude at the spatial Nyquist (either end of the graph) is relatively small in this snapshot, the time evolution of this region of the spectrum is nonlinear. 26

2.5 Convective instability timescales, ($1/|N|$ in minutes) as a function of the non-dimensional radius. It can be seen that growth rates of the convective instabilities lie in the same range as the time-scales associated with the acoustic waves. The instability arises as a direct consequence of the super-adiabaticity of the background model, and since we are not modeling the nonlinear physics of convection, it is crucial that we prevent this linear instability (described in §2.5.6) from affecting the acoustic signal. 30

2.6 These panels show a comparison between the properties of the atmosphere given by model S (dot-dash line) and the artificial model (solid line) used in the computation. The horizontal coordinate of all the above panels is the fractional radius, $r/R_{\odot}$. Panel (a) shows the cutoff frequency dependence with radius; the reflective property of model S is recovered quite accurately by the artificial model. Panel (b) is a comparison of the first adiabatic exponents; Γ_1 has been altered to render the artificial atmosphere convectively stable. Panel (c) shows sound speed dependence with radius; the layer extending from $0.9998R_{\odot} \leq r \leq 1.0007R_{\odot}$ is isothermal and therefore the sound speed is constant in that region. Panel (d) displays the all-important measure of convective stability, the Brunt-Väisälä frequency; it can be seen that the artificial model is sub-adiabatic in the near surface layer, thus ensuring the convective stability of the outer layers. 32

2.7 These panels show a comparison between the properties of the atmosphere given by model S (dot-dash line) and the artificial model (solid line) used in the computation. The horizontal coordinate of all the above panels is the fractional radius, $r/R_{\odot}$. Panels (a) and (b) show the variation of the logarithmic density and pressure with radius; it can be seen that the two models are quite similar. Panel (c) is a comparison between temperature profiles - the isothermal nature of the outermost layers of the artificial model is visible. Panel (d) shows gravity dependence with radius; the gravity profile of the artificial model is seen to decay more rapidly than that of model S. 33

2.8 Logarithmic power spectrum for a model that extends from $0.24 - 1.00033 R_\odot$. The excitation spectrum is a band that approximately encompasses $2000 - 5500$ μHz in frequency and $0 - 80$ in l. The highest l's contain little or no power to avoid spatial aliasing. Modes with inner turning points deeper than the lower simulation boundary are absent from this spectrum. Note that because the short time-scale convective instabilities have been removed, as described in §2.5.6, we see no power at frequencies below 2000 μHz. This spectrum was extracted from a 24-hour-long simulation. 35

2.9 Comparison between resonant wave modes computed by ADIPACK and the simulation. The modes extracted from the simulation are depicted as contours of power and the ADIPACK frequencies for this model are shown as stars. Note that for ease of comparison, only one in every five modes that are predicted by ADIPACK are depicted. The mode frequencies, located at contour centers are seen to match closely the frequencies given by ADIPACK. The ridge shapes of the power spectrum extracted from the simulation agree well with those predicted by ADIPACK. 36

2.10 The $m - \nu$ power spectrum with $l = 52$ for a simulation with pure rotation, the rate being $\Omega/2\pi = 4300$ nHz. The solid line shows the analytically calculated trend in the frequency shifts. The frequency resolution of this simulation was 28 μHz. In the absence of background flows, contours of maximum power would be lines parallel to the y-axis. Rotation causes frequency splitting, shifting pro-grade modes by $+m\Omega$ and retrograde modes by $-m\Omega$, as indicated by the solid line. Note that as expected, all the (shifted) lines are parallel. 37

2.11 Comparison of various ridges obtained from South pole (data first described in Schrijver et al., 1996) and simulated data. 39

2.12 Displayed are correlations obtained from MDI Medium-l data on the left panel and simulation data on the right panel. The x-axis is distance in Mega-meters, the y-axis time in minutes and the scale corresponds to the correlation coefficient. 40

2.13 Line asymmetry for wave modes with spherical harmonic degree $l = 30$. The mode amplitude is expressed in arbitrary units. The solid line shows modes captured in the velocity spectrum and the dashed line shows modes in intensity (essentially temperature fluctuations). These lines are asymmetric at low frequencies (< 4000 μHz) and become more symmetric as frequency increases (~ 4200 μHz). 41

2.14 Sections of velocity profiles, dimensions of the scale are in m/s. The upper panel shows the longitudinal velocity taken from the ASH simulation at a single radial cut, corresponding to $r = 0.92R_\odot$. The lower panel shows the cellular pattern exhibited by the longitudinal velocity at the surface, a crude model for supergranular activity. We use 4 times as many 'supergranules' in our calculations. 44

2.15 Quadrants used for travel time averaging. East-west rays are defined as those which propagate to from one horizontal quadrant to the other. Similarly, rays that span the vertical quadrants are north-south propagating. After computing the travel times for rays propagating in various directions, they are then averaged and classified according to the quadrant in which they propagate. 46

2.16 East-west travel-time difference map for a ray with $\omega/2\pi = 3.2$ mHz and $l = 128$ (inner turning point $r_1 = 0.92R_\odot$). The correlation of the travel-time map with the longitudinal velocity map (see figure 2.14) at the inner turning point radius is around 0.95, indicating that convective signals are strongly imprinted onto the travel-time differences. 47

2.17 The RMS east-west and north-south travel times on the left panel and correlations with corresponding velocity maps on the right panel, as a function of the inner turning point of the diagnostic ray. It can be seen that the east-west RMS travel times are consistently larger than the north-south travel times for a given ray, sometimes by as much as a factor of 2. The correlations do not follow such a clear pattern though. 48

2.18 Average power of convective velocities from the ASH simulation (in arbitrary units) for each degree, l at $r = 0.92R_\odot$. While the power increases from the bottom of the domain to the top, the distribution profile is almost constant with radius. The variation of power with wavenumber indicates the extent of the scattering caused by the convection on the propagating rays. The longitudinal velocity power is strongly focused around $l = 1$, indicating that the travel times will preserve the velocity structure of the convection. 48

2.19 RMS convective radial, latitudinal and longitudinal velocities from the ASH simulation, as a function of depth. The solid line shows the longitudinal RMS velocity, the dots show radial velocity and the symbols depict the latitudinal RMS velocity. 49

3.1 Comparison of wavenumber averaged power profiles of MDI high-resolution data (dot-dash line) and simulations (solid line) as a function of frequency. The f-mode power distribution in panel (a) is quite representative of the observations. Because of the lack of damping, the p-mode power distribution in panel (b) does not do quite so well. A phase-speed filter (Filter 'B' of Birch, Kosovichev & Duvall (2004)) was applied to obtain panel (b). 54

3.2 'Quiet' power spectrum obtained from a simulation in a $200 \times 200 \times 30$ Mm^3 box. The horizontal axis is spherical harmonic degree, l and the vertical axis is the frequency in milli-Hertz. 58

3.3 Vertical cut in the sound-speed perturbation discussed in Figure 3.4 and section 3.4.1. The labels on the isocontours show the amplitude of $\delta c^2/c^2$. 59

3.4 Panel (a): the time averaged RMS velocity of the wavefield interacting with a 12 Mm-sized sound-speed increase (shown in Figure 3.3), centered around $(x, y, z) = (100\ \mathrm{Mm}, 100\ \mathrm{Mm}, -10\ \mathrm{Mm})$. The sound-speed anomaly is entirely invisible in panel (a). The darkening towards the spatial edges of the frame is due to the absorbent sponge at work. Panel (b): the time averaged RMS velocity difference of the perturbed datacube and its quiet counterpart. The difference between the quiet and perturbed datacubes is greatest at the location of the perturbation due to enhanced scattering. Panel (c): the instantaneous difference between the perturbed and related quiet data 100 (solar) minutes into the simulation. The anomaly is a scatterer, creating ripples in the wavefield just like a pebble dropped onto the surface of still water. Fine wave structure is visible at the location of perturbation. 60

3.5 The spatial RMS velocity at the photosphere of a simulation (thick line) as compared to MDI high-resolution data (thin line) as a function of time. The system appears to achieve statistical stationarity 4.5 hours into the simulation. Because the system is linear, we can scale velocities by an arbitrary factor; in this case, velocities have been scaled so as to allow comparison with solar values. 61

3.6 Example of mean travel-time perturbation map $\delta\tau_{\mathrm{mean}}(\mathbf{r}, \Delta)$ for $\Delta =$ 30.55 Mm. Left panel: before quiet map subtraction. Right panel: after subtraction. 63

3.7 Cut across mean travel-time perturbation map $\delta\tau_{\mathrm{mean}}(\mathbf{r}, \Delta)$ from Figure 3.6 at $y = 50$ Mm. Thin line: before quiet map subtraction, thick line: after subtraction. 64

3.8 Azimuthal average of $\delta\tau_{\mathrm{mean}}(\mathbf{r},\Delta)$ (thick solid line) and $\delta\tau_{\mathrm{diff}}(\mathbf{r},\Delta)$ (thin solid line) for $\Delta = 30.55$ Mm, as a function of the radial distance to the sound-speed perturbation center (simulation). The dot-dash line is the mean travel-time shift computed with ray kernels for the background model in the simulation. The dashed lines are the solution to the forward problem using Born sensitivity kernels. The solar model in the simulation is slightly different from the model used to compute the Born kernels, contributing to the difference between the two travel-time curves. 66

3.9 The time averaged RMS of the difference in velocities from a simulation with one thousand randomly located 1 Mm-sized source suppressions and its unperturbed counterpart. In the vicinity of a source suppression, acoustic velocities are altered; therefore, the hundreds of local maxima in this difference map show where the sources are diminished. The perturbations are approximately limited to a 150×150 Mm^2 interior square, allowing for travel-time shifts associated with all the anomalies to be computed. 69

3.10 Source perturbations kernels for the f-mode. The panels (a) and (b) show the mean and left to right one-way kernels from Gizon & Birch (2002) respectively. Crosses show the measurement points. Upon systematically de-rotating and averaging the travel-time shifts associated with the thousand locally deactivated sources from Figure 3.9, subtracting the noise and scaling the travel times as described in appendix C.1, the kernels in panels (c) and (d) emerge. The lack of elliptical features in these kernels is perhaps explained by the independence of the sources from the wavefield, in the theory of Gizon & Birch (2002) and in the simulations. Panel (d) is especially compelling because according to theory, left to right one-way travel-times should only be shifted for those points which lie closer to the left measurement point. The power profile of the f-ridge used to recover the travel-time shifts is shown in Figure 3.1. 70

3.11 The source kernel obtained by the suppressing approximately half the sources and doubling the strengths of the rest. The integral of the kernel is an order of magnitude smaller than the amplitude of the kernel. 72

3.12 Panel (a): sound-speed kernel from 24 hours of simulated data (12 perturbed + 12 quiet). Panel (b): sound-speed kernel reproduced from the lower-right panel of Figure (10) of Birch, Kosovichev & Duvall (2004). The crosses mark the measurement points. The kernels have been multiplied by the sound speed at the photospheric level in both cases; units are in $10^{-2}\mathrm{Mm}^{-2}$. The agreement is striking. The circular features in panel (a) are generated by the repeated de-rotation of travel-time shifts and hence are mainly noise. Both hyperbolic and elliptic features are visible in this kernel. The power profile of the modes utilized to construct the kernel in panel (a) is shown in Figure 3.1(b). 73

4.1 Coefficients $|A_m|$ as a function of m for $R = 2$ Mm and $R = 0.5$ Mm (thick lines). Only the $m > 0$ values are shown since $|A_{-m}| = |A_m|$. The magnetic field is $B = 1$ kG, $\omega/2\pi = 3$ mHz, and $k_z = 0$. The coefficients A_m are negligible for $m > 5$ in the case $R = 2$ Mm and for $m > 2$ in the case $R = 0.5$ Mm. The open circles are the Born approximation to these coefficients ($|A_m^{\mathrm{Born}}|$, see section 4.4). 82

4.2 a) Real and b) imaginary parts of the scattered pressure field in the Born approximation (dashed line) and the exact solution (solid line). In this case the incoming wave is of the form $\tilde{p}_{\mathrm{inc}} = J_0(kr)$ $(m = 0)$ and we used $B = 1$ kG, $R = 2$ Mm, $k_z = 0$, and $\omega/2\pi = 3$ mHz. . . . 85

4.3 The fractional error $\eta_m = |A_m^{\mathrm{Born}} - A_m|/|A_m|$ as a function of ϵ for $m = 0$ (solid line), $m = 1$ (dotted line), and $m = 2$ (dashed line) for the case $R = 2$ Mm, $\omega/2\pi = 3$ mHz, and $k_z = 0$. 88

4.4 Plots of the pressure field of the unperturbed (a) and scattered (b - c) wavepackets at time $t = 8.9$ min after the unperturbed wavepacket has crossed the center of the magnetic cylinder. The wavepacket parameters are described in the text. The wavevector is normal to the axis of the magnetic cylinder and in the $+\hat{\mathbf{x}}$ direction. The strength of the magnetic perturbation is $\epsilon = 0.13$. In panel (b) the tube radius is $R = 0.2$ Mm and in panel (c) is the tube radius is $R = 2$ Mm. The circles outline the cross-section of the tube. Notice that the gray scales are different in each panel. The backscattered wave is more prominent for the tube with the smaller radius (panel b). 90

4.5 Local travel-time shifts $\delta t(\mathbf{r})$ caused by the magnetic cylinder ($\epsilon = 0.13$). The travel times are measured at positions $\mathbf{r}$ in a plane perpendicular to both the cylinder axis. The incoming wavepacket, which moves in the $+\hat{\mathbf{x}}$ direction, is the same as in figure 4.4a. The radius of the tube is $R = 2$ Mm and the tube axis is $(x, y) = (0, 0)$, as shown in figure 4.4c. In both panels the heavy solid line is the exact travel-time shifts, the circles are the Born travel-time shifts, and the light line gives the ray approximation. The left panel shows the travel-time shifts as a function of x at fixed $y = 0$. The right panel shows the travel-time shifts as a function of y at fixed $x = 10$ Mm. The Born approximation is reasonable for this value of ϵ. The ray-approximation does not capture finite-wavelength effects and fails to describe wavefront healing (Nolet & Dahlen, 2000). 91

4.6 Ratio $A_m^{\rm Born}/A_m$ in the complex plane at fixed $\epsilon = 1$ and $k_z = 0$. The ratio is plotted for varying values of the tube radius in the cases $m = 0$ (thick line), $m = 1$ (thin line), and $2 \leq m \leq 5$ (dashed lines). The big circles show the limit $kR \to 0$ given by equation (4.50). If the Born approximation were correct for small tube radii, the big circles would coincide with the cross. The small and medium-size circles are for $kR = 1$ and $kR = 1/2$ respectively. 93

5.1 The upper panels show comparisons of real and imaginary parts of the fit (labeled 'matched' in the figure) to the corresponding real and imaginary parts of the right hand side (RHS) for $\beta = 1$ and $\nu = 5$ mHz. Contributions to the real and imaginary parts of the right hand side (RHS) respectively from the jacket and resonant modes are shown in the lower panels. The lower boundary was placed at a depth of 98 Mm; the surface gravity mode with 13 acoustic and 857 jacket modes were used in this matching. 105

5.2 The amplitudes of the scattered resonant modes as a function of mode number shown for various values of plasma-β and frequency, ν. The legend applies to all panels. 106

5.3 The amplitudes of the scattered resonant modes as a function of mode number shown for various values of plasma-β and frequency, ν. The legend applies to all panels. 107

5.4 The phases of the scattered resonant modes a function of mode number shown for various values of plasma-β and frequency, ν. The legend applies to all panels. 107

5.5 The kink mode for $\nu = 5$mHz. The magnetically dominated case with $\beta = 0.1$ is seen to be very stiff, as opposed to the $\beta = 10$ case. 108

B.1 Resolution in the radial direction as a function of the non-dimensional radius; the solid line shows the grid spacing of the simulation. The wavelength in the radial direction is calculated from equation 2.7. We only display the grid spacing of a small fraction of the solar model, which actually extends from $r = 0.2R_\odot$ to $1.002R_\odot$ ($n_{rad} = 400$). The wavelength becomes a non-trivial fraction of the solar radius by about $r = 0.8R_\odot$, and the resolution monotonically increases with decreasing radius. 117

B.2 Spatial convergence rate of the compact finite differences with fifth-order accurate boundary conditions. The solid line shows the accuracy of the scheme, while the dashed line is the theoretical fifth-order accuracy curve. 119

B.3 Experiment to determine the spatial error convergence rate. The initial condition, a Gaussian wavelet in velocity, is shown in panel (a). In (b), the temporally evolved wavelet at time $t = 2$ min is displayed. Simulations are performed with varying numbers of grid points, $n = 721, 361, 181, 145$, and 121, so that each grid is a downsampled version (i.e., every other point, every third point etc.) of the $n = 721$ case. Errors are computed at $t = 2$ min using a downsampled version of the $n = 721, t = 2$ min solution as a template (panel b). In panels (c) and (d), the differences between the $n = 121$ solution and the downsampled $n = 721$ template at $t = 12$ min are displayed; it is seen that the difference, interpreted as the error, is greater in the unfiltered case in panel (d) than in the filtered version in panel (c), where the filter is applied to dealias variables in the radial direction (§ 2.5.2). The difference between (c) and (d), which although appears harmless, continues to grow, eventually overwhelming the simulation unless a de-aliasing filter is applied frequently. 120

B.4 Spatial error convergence rate (with radial dealiasing) based on the experiment of Figure B.3; the time step was $\Delta t = 0.05$ seconds. The solid line is the error of the compact finite differences and the dashed line is a theoretical sixth-order accuracy accuracy curve. It is somewhat surprising that the scheme obeys a sixth-order accuracy law despite the use of fifth-order boundary conditions. Partly, the reason could be that the problem is a consistent initial-boundary value problem, i.e. $v = 0$ and $\partial_z p = -\rho g$ at the boundaries. 121

B.5 Comparison of eigenfunctions for a resonant mode of frequency $\nu = 6.6111$ mHz, obtained analytically (solid line) and through simulation (dot-dash line) with $n = 121$. At higher resolutions, the two curves are virtually indistinguishable and hence are not shown here. Including the two boundaries, the eigenfunction contains only eleven nodes, far smaller than the number of grid points. With fewer ($\lesssim 80$) points, the system develops instabilities because of the steep density gradient. . . 124

B.6 Simulated (solid line) and analytical (dot-dash line) eigenfunctions for $\nu = 1.68$ mHz, for the model described above. It is seen that the boundary conditions and sponge do not affect the eigenfunction over the region of interest; although there is an amplitude error of a few % in the upper-most layers of the polytrope, the interior nodes are oblivious to the boundary conditions. This eigenfunction was obtained from a 24-hour simulation wherein the waves were constantly excited over a small region in the interior. 129

B.7 The sponge (solid line) and the upper boundary of the polytrope (and lower boundary of the isothermal atmosphere) at $s = 1$ (dot-dash line). In simulations with the altered solar model, the sponge is slightly sharper (spatially) and pushed a little farther outward. 130

B.8 Efficacy of the transmitting boundary. The initial condition is a Gaussian-shaped velocity impulse. Panel a shows the situation at $t = 10$ min, and the successive panels show the impulses at later instants in time. The amplitude in panel d is of the order of 10^{-6}, significantly smaller than in panels a through c. Together with the test of Figure B.6, the boundary seems to do a relatively good job of removing outward propagating waves while the interior portion of the eigenfunction is seen to be mostly undisturbed. 131

B.9 Error convergence rate of the temporal scheme. The solid line is the error of the second-order five-stage scheme of Hu et al. (1996) and the dashed line is the theoretical second-order accuracy curve. 133

B.10 Error convergence rate plotted against the spherical-harmonic bandwidth, l_{max}. The solid line displays the spherical-harmonic error in evaluating the latitudinal derivative and the dashed line shows the exponential convergence behaviour at high bandwidth. The onset of exponential convergence in the case of (sine/cosine) Fourier series occurs when the grid resolution reaches approximately π points per wavelength. We expect a similar effect to apply to the spherical harmonic basis. Since the number of latitudes n_{lat} must satisfy $n_{lat} \geq l_{max}$, and because $l_{max} = 19$ is sufficient to capture the function $-12 \cos^{11}\theta \sin\theta \sin^6\phi$, we expect the onset of exponential convergence to occur at $n_{lat} = l_{max} \sim 60$. The vertical dot-dash line indicates this location in the figure. 134

B.11 Power spectrum from a simulation. The dots show frequencies as estimated by ADIPACK (Christensen-Dalsgaard & Berthomieu, 1991). At lower frequencies, we observe a good match between the predicted and simulated dispersion relations, while the agreement is not quite so good at higher frequencies. 135

B.12 Duvall's Law (Duvall, 1982) for a solar model (panel a) and the altered model (panel b). Resonant modes (obtained using ADIPACK) of the artificial model used in the simulations collapse onto a single curve as seen in b. $\alpha = 1.05$, minimizes the spread in the altered model, while $\alpha = 1.13$ is the optimal value for the solar frequencies (panel a). The spread in panel a is defined relative to a fifth-order polynomial fit (dot-dash line) to the solar frequencies. The error in the reflection phase is 7%. 136

B.13 Envelope (group) travel times for differing numbers of bounces; simulated or artificial data (ART) and GONG data (GONG). Due to the altered solar model, a systematic difference between the travel times associated with real and artificial data is observed. In each of the comparisons, the modes of the simulated data possess lower travel times (private communication, Olga Burtseva and Shukur Kholikov). 137

Chapter 1

Introduction

The Sun, our nearest star, serves as an astrophysical benchmark, contributing to the development of our understanding of stellar evolution, stellar interiors, coronae etc. After the discovery of oscillations on the solar surface almost five decades ago (Leighton, Noyes, & Simon, 1962), there have been significant strides in uncovering various properties of the Sun. Helioseismology (see Christensen-Dalsgaard, 2002; Gizon & Birch, 2005, for reviews), somewhat analogous to geo-seismology, is a collection of methods applied to infer the interior structure and dynamics of the Sun through the study and observation of surface oscillations. The earliest efforts in this field were channeled towards determining the solar stratification and characterizing the nature of the observed modes. With the development of methods such as ring analysis (Hill, 1988), acoustic holography (Lindsey & Braun, 1997), and time-distance helioseismology (Duvall et al., 1993), it became possible in theory to study the fine structure of the Sun. Theory became reality with the advent of observations by the Solar Oscillations Investigations/Michelson Doppler Imager (SOI/MDI) instrument (Scherrer et al., 1995) onboard the Solar and Heliospheric observatory (SOHO) satellite, leading to putative discoveries of the subtle dynamics of local inhomogeneities like sunspots and active regions (e.g. Duvall et al., 1996). This branch of seismology came to be termed as local helioseismology, the study of which shall occupy a significant fraction of this dissertation.

Observations in the Sun begin at the photosphere, where the density is sufficiently low that radiation becomes the predominant energy transport mechanism. This surface is in continual motion due to the interaction, impact and reflection of millions of wave modes. The primary source of wave generation is the intense turbulence present in the convecting uppermost surface layers. In the sun, detected waves that possess diagnostic value are either surface gravity or acoustic modes. While surface gravity modes are constrained to sample only the surface layers, acoustic modes plumb the depths of the solar interior and re-emerge altered by the structure and dynamics of the solar interior. Because the Sun is stratified in a manner that the sound speed monotonically increases from the solar surface to the core, acoustic waves that begin their journey near the photosphere are perpetually refracted away from the center, being redirected towards the surface. This implies that most waves that are directed towards the interior propagate some distance following which they undergo the process of total internal refraction, turning around to return to the surface (e.g. Christensen-Dalsgaard, 2003). The acoustic power spectrum, a measure of the power distribution of the various resonant modes of the Sun, is shown in Figure 1.1.

Because density plummets in the near-surface regions, a large fraction of the acoustic wave spectrum is unable to propagate further, and is reflected, forced to repeat this process of alternate internal refraction and reflection till it is damped out by convective, radiative and other processes. The typical time scale of existence of large wave-length waves is about 5-7 days while small wave-length waves are damped much more quickly and presumably replaced by other waves created by the overturning convective cells (known as granules) at the photosphere. One of the most consequential results to emerge as a side-effect from the theory of solar oscillations is that neutrinos possess three flavours and a non-zero mass. Of less monumental but no doubt interesting and important set of results belong inversions of sunspot dynamics and structure, subsurface solar weather, traveling-wave convection, to name a few.

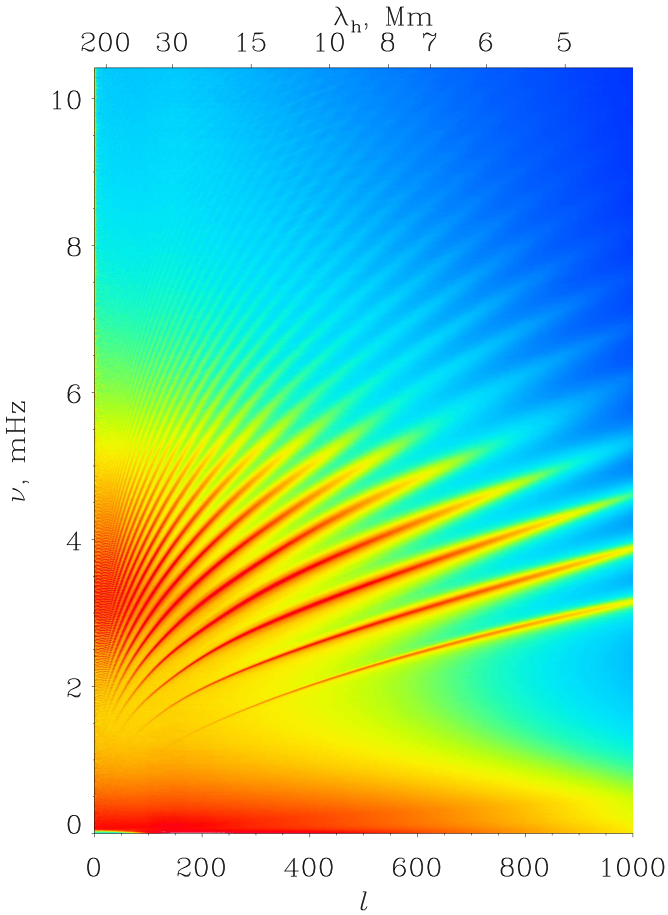

Figure 1.1 The Doppler velocity power spectrum of the Sun as observed by the MDI instrument. The lower horizontal axis is the spherical harmonic degree, l, an alternate measure of the wavelength of the wave, shown on the upper part of the graph as λ_b. The wavelength is expressed in Megameters while l is non-dimensional. The vertical axis is the frequency expressed in milli Hertz. Courtesy: the Solar Oscillations Investigation team.

1.1 Time-distance helioseismology

Time-distance helioseismology in particular has proven to be a very successful and robust method of inferring properties of the solar interior, involving careful manipulations of observations to coax travel times from data. Travel times are the consequential helioseismic metrics in the case of time-distance seismology. Cross correlations of velocity signals (obtained from observations) at pairs of points are computed and averaged in a coherent manner to increase the signal to noise ratio; subsequently these cross correlations are fitted by a standard cross-correlation function or more popularly, a Gabor wavelet (Chou & Duvall, 2000) to obtain travel times (see Figure 1.2).

In a complex and myriad system such as the Sun, the idea of an individual propagating wave makes little sense; a more fitting description may be achieved through the concept of a wave packet. A collection of waves of differing frequencies and wavelengths with one binding condition, that they satisfy a common dispersion relation, is defined as a wave packet. Although many definitions exist for travel times, an approximate (and sometimes misleading; see e.g., Hanasoge, Couvidat, Rajaguru, & Birch, 2007) 'physical' interpretation is the time taken for a wavepacket to travel between two specified points. The travel times of the 'quiet Sun' (where no systematic magnetic activity exists in the region of study) can be computed by tracing rays through a standard model of solar stratification. When travel times deviate in a consistent manner from these standard travel times, there is most likely a perturbation, a local disturbance or inhomogeneity that is the source of these anomalies. Inverse theory then attempts to recover these perturbations from the observed travel-time shifts.

To set up an inverse problem, the connection between perturbations and travel times must be determined; the devices that accomplish this feat are known as kernels. While establishing kernels in the ray approximation (e.g. Giles, 2000) is a relatively easy task, computing them in the limit of finite bandwidth wavepackets (e.g. Birch & Kosovichev, 2000) can be quite difficult. Once the kernel has been determined, the data is averaged in various ways to maximize the signal to noise ratio (SNR); subsequently, the linear inverse problem describing the anomaly of interest can be

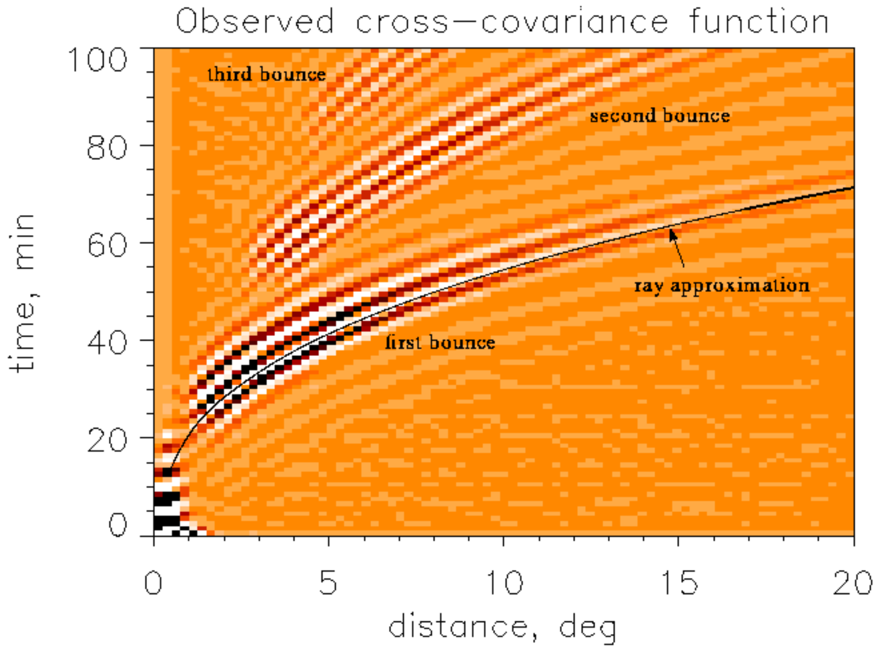

Figure 1.2 A time-distance diagram obtained by analyzing MDI data (Duvall et al., 1997). The ridges seen in the figure correspond to the time (on the vertical axis) taken by wave packets to travel the distance (in degrees) shown on the horizontal axis. The wave packet structure is contained in the ridges.

posed. Inverse problems in helioseismology are invariably ill-conditioned and require considerable regularization to extract solutions. Inverse methods are popular in helioseismology since one can directly seek answers to the question of what lies beneath.

1.2 Magnetic field interactions

Understanding the existence and variability of magnetic activity in the Sun is a problem of wide significance. The ability to predict the solar dynamo, i.e., the regeneration followed by dissipation of magnetic fields in 11 year cycles, is one of the holy grails of solar physics. Another problem of considerable interest and more recently, controversy, relates to the influence of magnetic fields on acoustic waves in the near surface regions of the Sun. In these sub-photospheric magnetic regions, the ratio of magnetic to gas pressure could be very close to unity, leading to the contention that magnetic field effects are systematic and significant. However, due to the difficulties involved in modeling magnetic field effects, most helioseismic analyses tend to ignore these effects, lumping them all into a ‘surface term’. Several results that invoke this assumption have come into question and in particular, inversions of the interior structure of sunspots have attracted much debate.

Owing to the intense magnetic field strengths and the inclination of the field in the penumbra (e.g. Schunker et al., 2003), sunspot structure and dynamics inversions (e.g. Duvall et al., 1996; Couvidat, Birch, & Kosovichev, 2006) have been a source of considerable discussion. The very question of how a penumbra is formed around a central umbra in a sunspot is as yet unexplained; current 3D Radiative-Magneto-Hydrodynamic simulations of sunspots are unable to replicate the penumbra. Some of these inversions (Couvidat, Birch, & Kosovichev, 2006) use finite-wavelength descriptions of the acoustic wavefield derived from the approximated constituent equations in the Born limit (Birch & Kosovichev, 2000). Gizon, Hanasoge, & Birch (2006) showed that although the first Born approximation may be valid in regions where the magnetic to gas pressure ratio is much less than unity, its applicability in regions of high magnetic to gas pressure ratios such as sunspots is highly debatable.

Mode conversion (e.g. Barnes & Cally, 2000) is a phenomenon commonly associated with magnetic field induced scattering. From one acoustic mode to another, from acoustic modes to Alfvèn waves and so on, it is estimated that acoustic energy is somewhat redistributed and otherwise lost (in the conversion to Alfvèn waves), contributing perhaps to p-mode absorption observed in sunspots (Braun, 1995). The mode absorption in sunspots detected by Braun (1995) is substantial and until the causal factors are conclusively determined, the relatively simplistic pure acoustic approach in the handling of active regions and sunspots is further threatened.

In terms of taking small steps towards comprehending the influence of magnetic fields on observations, it can be very insightful to estimate the effect of magnetic flux concentrations on waves, the diagnostic agents of the interior. When these interactions are well understood, the next steps will be to use this knowledge to infer interior magnetic structures. Once tomography of the magnetic interior is made possible, views of the interior magnetic field can be used to attempt answers to larger issues such as the existence of the dynamo. However, this is easier said than done because mathematically, it is a difficult proposition to build a clear understanding from the wave equations due to the complex nature of the Lorentz force term and the induction equation. Magnetic forces are tensorial by very nature; consequently parametrizing the effects of competing factors such as the angle of inclination, field strength, size of the flux tube etc. is not an easy task. In fact, even devising a fully magneto-gravito-hydro-static model of a sunspot in the near-surface layers is a highly non-trivial affair.

1.3 The Forward method

One way to address these intricate questions is to numerically compute the interactions of waves with these perturbations. By constructing computational models that mimic the interactions of the solar wave spectrum with various perturbations as closely as possible, it will be possible to lend a clearer interpretation to the observations. This alternative approach to the inverse method (described previously) is known as *forward* modeling. The wavefield is theoretically computed in the presence of various sizes, magnitudes and (perhaps) types of perturbations; shifts in the helioseismic metrics (like travel times) obtained thereof are compared to shifts seen in observational data. These calculations are carried out with the outlook that a close approximation to observations is reason to believe that the structure of the test perturbations are to some extent, representative of reality. However, the uniqueness of the structure is not easy to ensure.

As observations have become increasingly sophisticated, the need for refined forward modeling has become apparent. One reason the forward approach is crucial is that although the resonant mechanical modes of the Sun (the diagnostic agents of helioseismology) have been studied carefully, there are still many curious wave properties neglected in models that may prove significant. For example, finite wavelength effects cast doubt on the validity of the ray approximation in some situations; magnetic fields in the case of sunspots are potentially non-trivial contributors to the wavefield. Because the sound speed in the deep interior is very large, the wavelength, which increases in direct proportion to the sound speed (linear wave propagation), becomes a sizeable fraction of the solar radius. The resolving ability of the wave, commonly estimated to be half to one wavelength for mechanical waves, also decreases, making it impossible to image small-scale dynamics of the deep interior. The fact that waves have very little time (scaling inversely with the sound speed) to sample the structures at these great depths does not aid our cause either. Other wave properties that prove to be a hindrance are geometric spreading and wavefront healing. The former means that the signal is even harder to recover from observations and the latter that the waves are likely to 'forget' that they interacted with a convective cell or some such other structure. In such murky waters (quite literally!), these calculations are very useful because they will likely provide insight into the nature of the signal and the extent of the noise. We can set bounds on detectability and determine the sensitivity of diagnostic agent waves. Although these implications have been known for a while now, a systematic means of investigating such factors have only recently been constructed. Such studies are difficult to conduct by purely analytical means, requiring the introduction of numerical methods to solve the constituent governing equations of wave motion. A significant part of this dissertation attempts to develop and apply techniques specifically to study the solar interior through forward models.

1.4 Results Contained in This Work

The results in this dissertation all fit under the umbrella of wave interactions in the Sun: with flows, thermal asphericities and magnetic fields. Chapter 1 attempts to deliver an overview of helioseismology, the approaches and motivation behind the various problems selected for investigation. In Chapter 2, I describe the numerical methods applied to perform wave calculations in spherical geometry; some validation tests are constructed to ensure the accuracy of the algorithm. Since wave propagation in the Sun is mostly a linear phenomenon and due to the expensive nature of non-linear computations, a linear wave calculation is strongly preferred. However, the near-surface layers of the Sun are so convectively unstable that the stratification in this region must be reconfigured for these simulations to be bounded. A realistic wave excitation mechanism is discussed, the acoustic wave spectrum recovered upon simulations is shown to possess many properties similar to the Sun. The detection of (deep) interior convection has for long, eluded observational efforts. Using 3D non-linear Anelastic Spherical Harmonic (ASH) simulations of interior convection, the question of the detectability of these structures is broached via the ray approximation and wave theory in chapter 2. We determine the signal to noise properties of structures at various depths and estimate the chances of detecting deep convective cells. The focus of this chapter is on the numerical method and basic results with a section on the detectability of flows.

From this point, we make a switch in the geometry, from spherical to Cartesian. In chapter 3, the very useful concept of noise subtraction is introduced, along with a host of other results and validation tests for simulations in Cartesian geometry. Because of the stochastic nature of wave excitation in the Sun, there is a great deal of realization noise in actual data that reduces the signal to noise ratio substantially. In the Cartesian box based computations, we strive to attain similar realization noise properties so as to allow clear interpretations of these simulated results in the context of helioseismology. However, because of finite computational resources, only a limited number of simulations are possible, and this might appear to be a bottleneck. It is shown that with a non-recurrent initial computational cost, the realization noise problem can be considerably mitigated. Applying techniques of time-distance helioseismology, we also show how to recover kernels (used typically to solve inverse problems) from relatively short simulations. Further, a test to verify that the experimental method of extracting kernels from observations is constructed; it shown that indeed, this experimental technique is valid.

Having stated the strong case for pursuing the forward problem, I shall take a tangential step towards theoretical methods of understanding wave interactions with magnetic fields. The validity of the Born approximation, widely used in geophysics and helioseismology, is tested on magnetic fields in chapter 4. Using a simple model of a magnetic flux tube placed in a homogeneous infinite medium, the scattering properties of waves incident on the flux tube are recovered using the Born approximation and independently, an exact solution in the linear limit of small fluctuations. The effect of wavefront healing is also demonstrated.

Continuing with the study of magneto-wave interactions, the scattering matrix and scattering cross-section of a thin flux tube embedded in a realistic polytrope are computed in chapter 5. Scattering measurements in similar situations have been observationally estimated; comparing our theoretical model with actual observations is useful in determining if we possess a sound understanding of this complicated scattering phenomenon. Both numerical and analytical techniques are applied to obtain these scattering properties.

Chapter 2

Computations in spherical geometry

2.1 Introduction*

Solar oscillations possess abundant diagnostic information about the solar interior. Helioseismology is the study of the variations in the internal structure and properties of the dynamics of the sun from measurements of its surface oscillations. Sophisticated observations of these oscillations have led to the inference of the solar structure, the rotation-rate and large-scale dynamics with considerable accuracy. For example, a major result of helioseismology has been the constraint on the solar neutrino flux which led to a re-evaluation of the properties of the neutrino. Helioseismic analyses use the line of sight Doppler velocity of plasma at the solar photosphere. This surface is in continual motion due to the interaction, impact and reflection of millions of wave modes. The primary source of wave generation is the intense turbulence present in the convecting uppermost surface layers. In the sun, detected waves that possess diagnostic value are either surface gravity or acoustic modes. While surface gravity

**The results of this chapter are reproduced from Hanasoge et al. (2006), Hanasoge & Duvall (2006), Hanasoge et al. (2007), and Hanasoge & Duvall (2007). I performed all the simulation work and wrote most of the content; J. Christensen-Dalsgaard helped compute the ADIPACK data, Tom Duvall, Jr. extracted travel times from the simulations and analyzed south-pole data. The ASH profiles were provided by Marc DeRosa.*

modes are constrained to sample only the surface layers, acoustic modes plumb the depths of the solar interior and re-emerge altered by the structure and dynamics of the solar interior. A substantial part of the wave modes that comprise the acoustic wave spectrum travel distances large enough that incorporating sphericity into the model becomes unavoidable.

The first time-distance (Duvall et al., 1993) validation test involving acoustic simulations, of time-distance helioseismology was performed by Jensen et al. (2003), who computed a 3D wavefield in a solar-like atmosphere in the presence of a finite sized sound-speed perturbation. The inverted data recovered the main features of the perturbation but was still quite noisy. Little has been done, however, in the context of the forward problem in spherical domains to complement the extensive inversion analyses applied to data obtained from the Michelson Doppler Imager (MDI) onboard the Solar and Heliospheric Observatory (SOHO), in operation since 1996.

Our objective is to construct a numerical model that allows waves to propagate within a spherically stratified domain, from which the wavefield can be analyzed. The physics of the sun is governed by an enormous dynamic range, with scales stretching from as short as a meter to as long as several million meters. It is not yet computationally feasible to model this plethora of scales and the phenomena associated with them. Consequently, the goal of this effort is not to produce accurate absolute frequencies to compare with the observations. The aim is to design a careful means to perform *differential* studies on the effects of large-scale flows and asphericities, in the context of global and local helioseismology. The expectation is that the helioseismic signatures of the differences in the acoustic wavefield induced by the presence of flows or asphericities are mostly insensitive to the physics we have chosen to discard. Simulations of the wavefield in the presence of large-scale perturbations can be compared with a reference case that corresponds to a computation of the wavefield in the absence of any flows or perturbations. It is important that the forward model be designed to mimic the Sun as closely as possible because data produced from such a model will likely easily lend themselves to interpretation in the context of the solar case. On the other hand, it is equally useful to leave the system simple enough that we are able to understand the individual contributions of various perturbations on helioseismic metrics such as travel times, mode frequencies etc.

The utility of the forward approach cannot be understated, for it paves the way for us to gauge the ability of helio- and astero-seismology to infer the interior properties of the Sun and other stars. In relation to the Sun, we are already investigating the signal to noise properties of deep active regions, holographic far-side signatures of active regions (sunspots and the like), detection of convection and line-of-sight projection anomalies.

In this chapter, we discuss computational techniques and the issues that are encountered in a system where thermodynamic properties such as temperature, pressure, and density are strongly spatially varying. We also present techniques of validation that were used to demonstrate the verity of this computation. The problem is defined in §2, §3 describes the numerical techniques, §4 introduces the reader to wave behavior in a solar like medium, §5 addresses various computational difficulties, §6 discusses methods of validation and in §7, we summarize and draw conclusions.

2.2 The problem definition

We solve the three-dimensional linearized Euler equations of fluid motion in a spherical shell encompassing $0.24 - 1.0004 R_\odot$, expanded around the spherically symmetric background state described by Model S of the sun (Christensen-Dalsgaard et al., 1996). The assumption of linearity is justifiable since acoustic wave velocity amplitudes are much smaller than the background sound speed within the bulk of the computational domain. Because timescales of acoustic propagation are much smaller than the timescale over which large-scale flows or features (of interest to us) change, we assume that the background state is stationary. In the equations that follow, all background quantities are subscripted with a 0, and all other components are fluctuating.

$$\frac{\partial \rho}{\partial t} = -\boldsymbol{\nabla}\cdot(\rho_0 \mathbf{v}) - \boldsymbol{\nabla}\cdot(\rho \mathbf{v}_0), \tag{2.1}$$

$$\frac{\partial \mathbf{v}}{\partial t} = - \boldsymbol{\nabla}(\mathbf{v}_0\boldsymbol{\cdot}\mathbf{v}) - \boldsymbol{\omega}_0\times\mathbf{v} - \mathbf{v}_0\times\boldsymbol{\omega} - \frac{\rho}{\rho_0}\left(\boldsymbol{\nabla}(\frac{1}{2}v_0^2) + \boldsymbol{\omega}_0\times\mathbf{v}_0\right) - \frac{1}{\rho_0}\boldsymbol{\nabla}p - \frac{\rho}{\rho_0}g\hat{\mathbf{r}} - \Gamma(r)\mathbf{v} + S(r,\theta,\phi,t)\hat{\mathbf{r}}, \tag{2.2}$$

$$\frac{\partial p}{\partial t} = -\mathbf{v}_0\boldsymbol{\cdot}\boldsymbol{\nabla}p - \mathbf{v}\boldsymbol{\cdot}\boldsymbol{\nabla}p_0 - \Gamma_1 p_0\boldsymbol{\nabla}\boldsymbol{\cdot}\mathbf{v} - \Gamma_1 p\boldsymbol{\nabla}\boldsymbol{\cdot}\mathbf{v}_0, \tag{2.3}$$

$$\Gamma_1 = \left(\frac{\partial \ln p}{\partial \ln \rho}\right)_{ad}. \tag{2.4}$$

Equations (2.1), (2.2), and (2.3) are equations of continuity, momentum and energy respectively. The derivative on the right-hand side of equation (2.4) is evaluated along an adiabatic process curve (as denoted by the subscript 'ad'). The nomenclature is as follows: ρ is the density, p the pressure, $\boldsymbol{\omega}$ the vorticity, $\Gamma_1 = \Gamma_1(r)$ is the first adiabatic exponent, g is gravity, and $\mathbf{v}$ is the vector velocity. Equation (2.3), which states that wave propagation is adiabatic, is justified because the viscous and heat transfer timescales are long in comparison to the acoustic timescales, over much of the computational domain.

The term $\Gamma(r)\mathbf{v}$ in equation (2.2) plays the role of a damping agent and $S(r,\theta,\phi)\hat{\mathbf{r}}$ is the radially directed dipole source. It is believed that wave excitation in the sun occurs in an extremely narrow spherical envelope (200 km thick) bounded by the surface (e.g., Skartlien & Rast, 1999), and we assume therefore, $S(r,\theta,\phi,t) = \tilde{S}(\theta,\phi,t)\delta(r - r_{ex})$, where $r_{ex} = 0.9997R_\odot$ was chosen to be the radial location of the source. $\tilde{S}$ is a spatially broadband random function for all but the largest horizontal wavenumbers, which are not included so as to avoid any issues of spatial aliasing. The solar wave power spectrum possesses maximum power in the range $2000 - 5500\mu$Hz with a peak in power around 3200 μHz. In order to mimic this excitation behavior, we generate a Gaussian distributed power spectrum with a mean of 3200 μHz and a standard deviation of 1000 μHz in frequency space, which we then Fourier transform to produce a time series with the appropriate source spectrum.

In this study, we perform simulations over a time period that exceeds the time at which the acoustic energy reaches a statistical steady state. The other requirement for the temporal length of the simulation is that the frequency resolution be sufficient for the application at hand. The velocity time series, extracted at the surface, is projected onto a line of sight and used as artificial Doppler velocity data.

2.3 Numerical method

The procedure we employ is pseudo-spectral; we use a spherical-harmonic representation of the spherical surface, sixth-order compact finite differences in the radial direction (see Lele, 1992) and a second-order, five-stage Low Dissipation and Dispersion Runge-Kutta (LDDRK) time-stepping scheme (see Hu et al., 1996). Latitudes are Gaussian collocation points and longitudes are equidistant. The radial grid is mostly based on the sound speed distribution and is discussed further in § 5.1. The code was developed and run on a multiprocessor SGI-Altix machine at Stanford.

2.3.1 Parallelism in OpenMP

One of the parallel implementations is in OpenMP (shared memory) with radial locations domain distributed, allowing all the spherical-harmonic transforms to be performed in-processor. Spherical-harmonic transforms are computed in two steps: longitudinal FFTs at each latitude and radius followed by Legendre transforms for each Fourier coefficient and radius. FFTs are performed using the Guru routines provided in FFTW 3.0 and Legendre transforms using matrix-matrix multiplication techniques implemented in Level 3 Basic Linear Algebra Subroutines (BLAS). The associated Legendre polynomials P_l^m, where l and m are the spherical-harmonic degree and order respectively, are divided into a series of matrices corresponding to different m's, each of which is further divided into two matrices according to whether $(l - m)$ is even or not. This is done to exploit the symmetry of the associated Legendre polynomials about the equator, which speeds up the transform by a significant amount.

The associated Legendre polynomials are computed according to a highly stable four term recurrence algorithm given by Belousov (1962), available at netlib (the STSWM package). Each transform is a computation of order $O(n_{lon}^2 \cdot n_{lat} \cdot n_{rad} \cdot \log(n_{lon}))$, where n_{lon} is the number of longitudinal gridpoints, n_{lat} the number of latitudinal gridpoints and n_{rad} the number of radial gridpoints. To prevent aliasing, we apply the two-thirds rule (Orszag, 1970) which sets the lower bound on the number of latitudes at $3l_{max}/2$ where l_{max} is the maximum l of the simulation. To ensure equal resolution in the latitudinal and longitudinal directions, we set $n_{lon} = 2n_{lat}$. Recasting the minimum operation count in term of l_{max}, we obtain an expensive operation count of $O(n_{rad} \cdot l_{max}^3)$; it is therefore important to minimize the number of times spherical-harmonic transforms are performed. Every timestep requires the computation of a curl, divergence, and four gradients, each of which involves a computational equivalent of a forward-inverse transform pair. Level 3 BLAS is known to operate near the peak performance of the processor, so these computations are generally very efficient, when they are performed in-processor.

2.3.2 Parallelism according to message passing

The code was re-written according to the Message Passing Interface (MPI) standard, a version that runs well on large numbers of processors, and at large values of l, as opposed to the OpenMP version, which does not do quiet so well on large problems. In the MPI version, data is domain distributed according to latitudes in real space, and Fourier coefficients in Fourier space. Spherical-harmonic transforms are computed in two steps:

1. Longitudinal FFTs at each radius (all located in-processor) and the in-processor latitudes.

2. The data is transposed and redistributed across processors, so that all latitudes and radial points corresponding to a Fourier coefficient are in-processor. This is to ensure that the Legendre transforms for each Fourier coefficient and radius are computed optimally.

The FFTs and Legendre transform are implemented in the same manner as described in §2.3.1. Spherical harmonic coefficients are divided across processors using the algorithm described by Foster & Worley (1997).

We place transmitting boundary conditions (Thompson, 1990) at both radial boundaries of the computational domain. While this particular boundary condition is most effective at absorbing waves that are of normal incidence, it reflects a significant percentage of all other waves. To mitigate this effect, we introduce an absorbent buffer zone (for example, see Lui, 2003; Colonius & Lele, 2004), placed in the evanescent region, that damps waves out substantially before they reach the boundary. This is one of the purposes that the term $\Gamma(r)$ in equation (2.2) fulfils.

2.4 Acoustic wave propagation in the sun

Acoustic modes are uniquely identified by three parameters, the spherical-harmonic degree l, azimuthal order m, and radial order n. A detailed description of this classification system and more on wave behavior as a function of these parameters can be found in chap. 5 of Christensen-Dalsgaard (2003). Because sound speed increases with depth, waves that are initially propagating at a non-zero angle to the upper boundary refract continually as they propagate deeper until they undergo total internal refraction at some depth and re-emerge at the surface. At the point of total internal refraction, also known as the inner turning point, the wave is propagating purely horizontally. To determine the location of the inner turning point we proceed as follows. The dispersion relation is

$$\omega = ck, \tag{2.5}$$

where ω is the frequency, c the sound speed, and $k = |\mathbf{k}|$, where $\mathbf{k}$ is the vector wavenumber. We decompose $\mathbf{k}$ into a radial ($k_r\hat{\mathbf{r}}$) and a horizontal ($\mathbf{k_h}$) component according to

$$\mathbf{k} = k_r\hat{\mathbf{r}} + \mathbf{k_h}. \tag{2.6}$$

We have, using equations (2.5) and (2.6),

$$k_r^2 + k_h^2 = \frac{\omega^2}{c^2}, \tag{2.7}$$

where $k_h = |\mathbf{k_h}|$, the horizontal wavenumber, is given by

$$k_h(r) = \frac{\sqrt{l(l+1)}}{r}. \tag{2.8}$$

To determine the inner turning point, r_t, we set $k_r = 0$, and obtain

$$\frac{c(r_t)}{r_t} = \frac{\omega}{\sqrt{l(l+1)}}. \tag{2.9}$$

This relation thus provides us a means to identify the maximum penetration depth of each wave mode. The inverse is true as well: the frequency-wavenumber range of waves that can access a given depth may be determined from equation (2.9).

2.4.1 Upper turning point: reflection at the surface

The acoustic cutoff frequency ω_A, below which waves become evanescent, is related to the density scale height, H_ρ, in the following manner (Deubner & Gough, 1984)

$$\omega_A = \frac{c}{2H_\rho}\left(1 - 2\frac{dH_\rho}{dr}\right)^{\frac{1}{2}}. \tag{2.10}$$

We define H_ρ as

$$H_\rho = -\left(\frac{d\ln\rho}{dr}\right)^{-1}, \tag{2.11}$$

and in a similar manner, the pressure scale height, H_p, as

$$H_p = -\left(\frac{d\ln p}{dr}\right)^{-1}. \tag{2.12}$$

As waves propagate towards the surface, the density and pressure scale heights become increasingly small, as depicted in Figure 2.1. The dependence of the cutoff frequency as a function of radius is shown in Figure 2.2. Waves possessing frequencies higher than 5500 μHz or so escape into the atmospheric layers and they are of little interest to us. The rest of the spectrum is reflected at locations, also known as the upper turning points, where the wave frequency equals the cutoff frequency. This property was taken into account when choosing the excitation parameters. A useful consequence of this arrangement is that above their upper turning points, waves with frequencies less than the cutoff become evanescent. This aids the design of a transparent boundary condition, since these waves can be damped into non-existence much more easily.

2.5 Computational issues

Computationally speaking, the properties of the sun are relatively well behaved and comparatively easy to model up to about $r = 0.98R_\odot$. The near-surface layers however, introduce the multiple difficulties of rapidly dropping density height scales, increasingly unstable stratification, the presence of an ionization zone, complexity in the equation of state, and nonlinearities into the wave propagation physics. Added to these issues is the fact that acoustic waves spend most of their time in the near-surface layers because the sound speed is smallest here. The consequences of not taking into account some or all of the complex near-surface dynamics is not entirely clear because the issues listed above are inextricably linked to each other.

Keeping in mind the important issue of computational feasibility, we cannot hope to resolve the complex small-scale physics of the near-surface layers or model the convecting solar interior. In fact, we see the formalism presented in this article as complementary to the work of, e.g., Rosenthal et al. (1999), Georgobiani et al. (2003), who perform detailed hydrodynamical simulations of the near-surface layers to extract information about their effects on the frequencies and excitation of the modes. We reiterate that the method presented herein is a means to study the *differential* effects of flows and asphericities on various helioseismic measures, such as resonant frequencies, travel-time anomalies etc..

2.5.1 Choice of radial grid

To determine an appropriate radial grid, we have taken into account the strong radial dependence of background solar properties such as pressure, density and sound speed. Consider a wave propagating at the speed of sound in the radial direction according

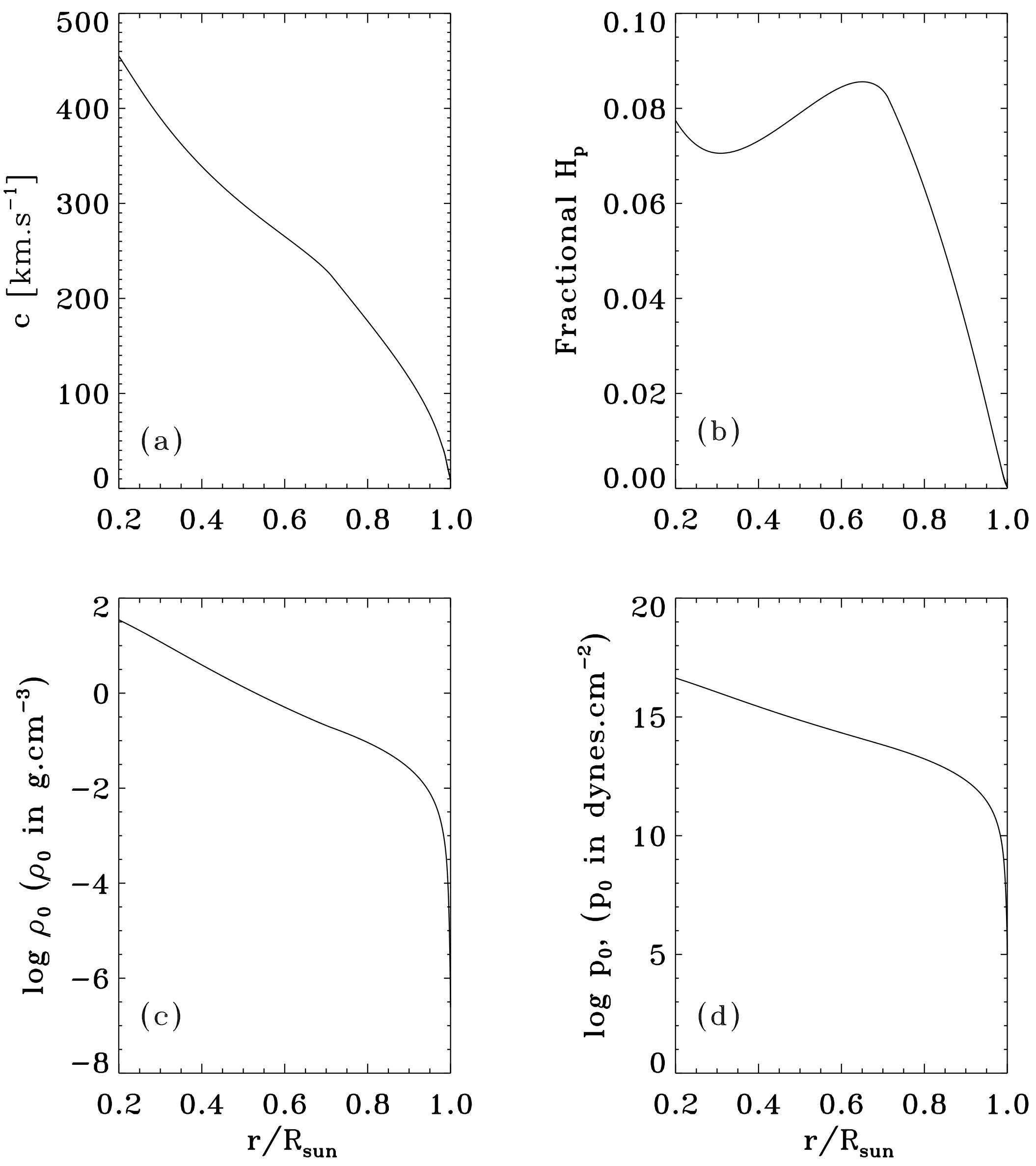

Figure 2.1 Background properties from model S of the sun (Christensen-Dalsgaard et al., 1996) as functions of radius. The horizontal coordinate of all the panels above is the fractional radius, $r/R_\odot$. Panel (a) shows the dependence of sound speed (in $\mathrm{km \cdot s^{-1}}$) with $r/R_\odot$. Panel (b) contains the fractional pressure scale height variation ($H_p/R_\odot$; H_p has been defined in Eq. [2.12]) with the fractional radius. Note the rapidly decreasing scale height in the near-surface layers. Panel (c) and (d) show logarithmic variations in density and pressure as a function of the fractional radius.

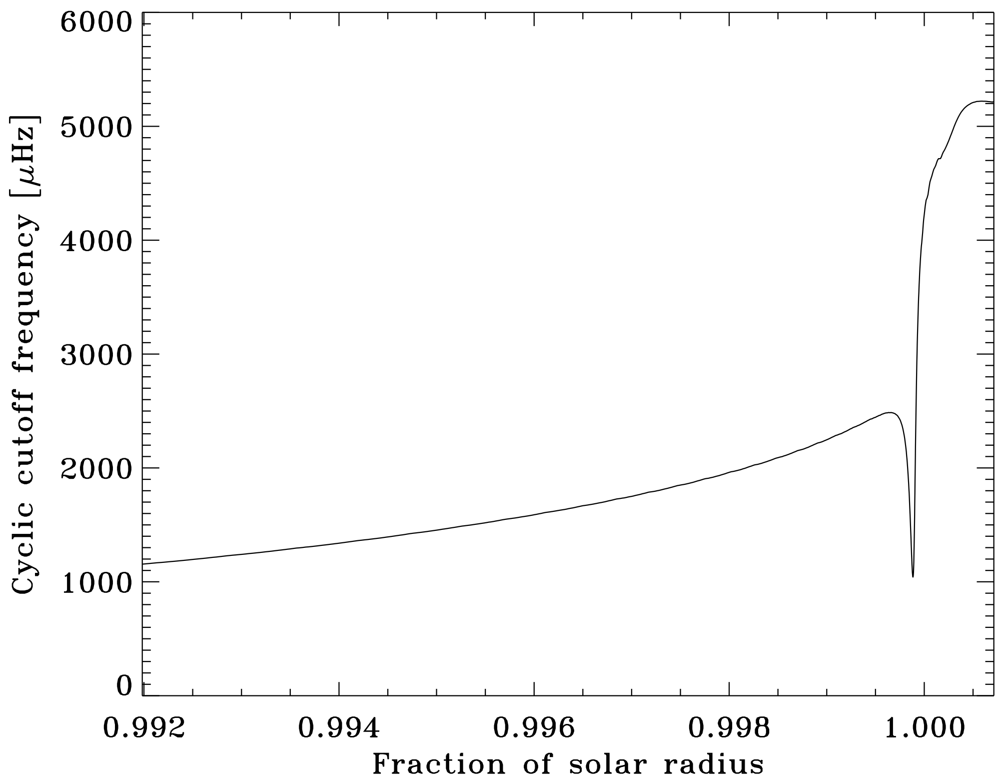

Figure 2.2 Acoustic cutoff frequency $\omega_A/2\pi$ as a function of radius in the model. The steep rise in ω_A in the near-surface layers is due to rapid changes in the density scale height, and causes outward-propagating waves with frequencies $\omega < \omega_A$ to reflect and propagate inward.

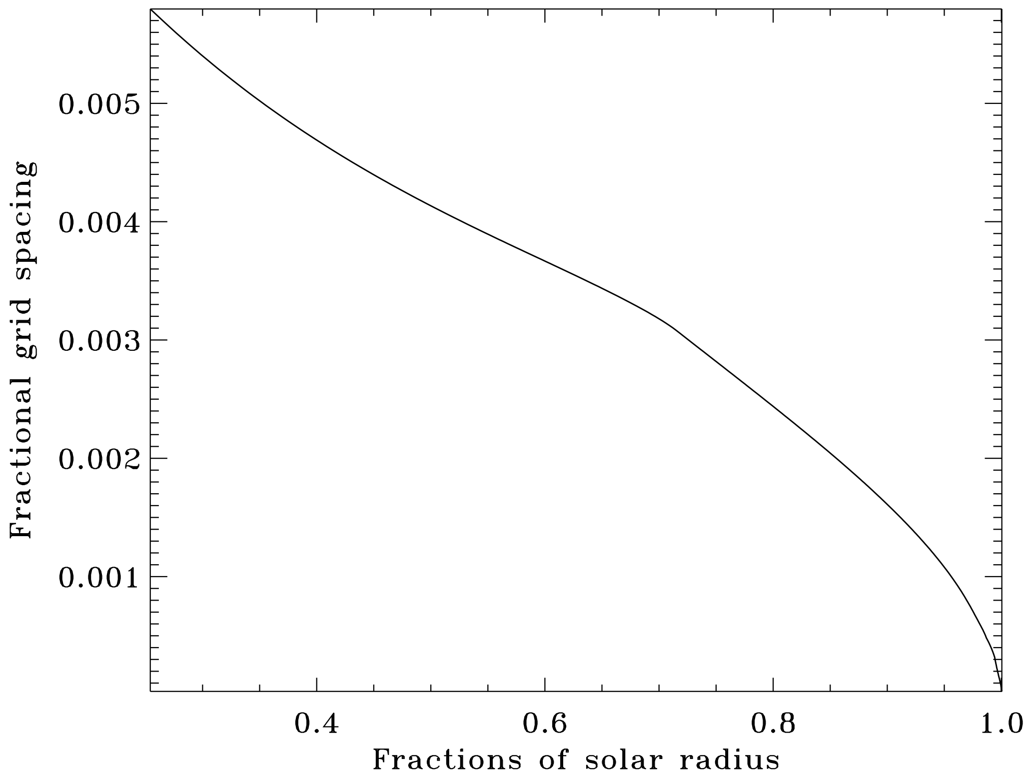

Figure 2.3 Fractional grid spacing as a function of radius for $n_{rad} = 350$. Plotted is $dr/R_{\odot}$, where dr is the local grid spacing, as a function of the fractional radius, $r/R_{\odot}$. For $r \leq 0.99R_{\odot}$, the grid spacing is chosen to maintain the constancy of the travel time of an acoustic wave between adjacent grid points. To account for rapidly decreasing scale heights, the radial grid points from $0.9915R_{\odot}$ to the upper boundary are equally spaced in $\ln p$. Third order splines are used to vary the grid spacing between 0.99 and $0.9915R_{\odot}$ as smoothly as possible.

to the simple advection equation

$$\frac{\partial u}{\partial t} + c(r)\frac{\partial u}{\partial r} = 0. \tag{2.13}$$

It makes immediate sense to choose a grid stretching function

$$\tau(r) = \int_r \frac{dx}{c(x)}, \tag{2.14}$$

that transforms equation (2.13) to

$$\frac{\partial u}{\partial t} + \frac{\partial u}{\partial \tau} = 0, \tag{2.15}$$

a form that is much easier to handle. The relation between two adjacent grid points then is

$$\int_{r_i}^{r_{i+1}} \frac{dr}{c} = \delta, \tag{2.16}$$

$$\delta = \frac{1}{n_{rad} - 1} \int_{r_{in}}^{r_{out}} \frac{dr}{c}, \tag{2.17}$$

where r_{in}, r_{out} are the inner and outer radii respectively and n_{rad} is the number of radial grid points including the boundaries. Since sound speed is a monotonically decreasing function of radius, the radial grid spacing becomes larger at depth. Also important to note is that gradients of background quantities become smaller with depth and it makes sense that the grid is coarser.

However, as noted in §4, pressure and density scale heights tend to become very small at the surface and pressure and density fall much more rapidly with radius than sound speed. It is therefore useful to choose a different heuristic for the grid spacing for the outer layers, perhaps along the lines of a logarithmic pressure grid. In this simulation, we have adopted a constant travel-time grid for $r \leq 0.99R_\odot$, patched smoothly with one equally spaced in $\ln p$ from $0.9915R_\odot$ to the upper boundary. Third order splines are used to vary the grad spacing between 0.99 and $0.9915R_\odot$ as smoothly as possible. Figure 2.3 displays the grid spacing as a function of radius.

2.5.2 Spectral blocking and radial dealiasing

Spectral blocking is an aliasing phenomenon that commonly occurs in non-linear calculations, wherein the lack of resolution results in a super-linear accumulation of energy near the Nyquist frequency. It poses a serious numerical challenge, since the energy growth is very rapid, leaving the computation unstable and inaccurate. We discuss its appearance in our *linear* calculations and how we deal with this issue. Standard Fourier transforms are defined on grids where the travel time for waves between adjacent grid points is a constant over the grid. In the solar case, the sound speed is a strong function of radius and consequently, it makes little sense to speak of a Fourier transform on a uniformly spaced radial grid. The Fourier transform in this situation is only made meaningful on a grid stretched such that the travel time between adjacent grid-points is constant over the grid. The rest of the discussion in this section follows as a consequence of this grid stretching and the consequent interpretation of the Fourier transform on this grid.

As described above, the source function is highly limited in the radial direction resulting in the excitation of waves with a wide spectrum of radial orders. The resolution in the radial direction is restricted by the finiteness of computational resources at our disposal and the scientific interest in investigating these high radial orders. For the applications that we are interested in, both these criteria indicate that these high radial orders are best done away with. Associated with the inability of the radial grid to capture modes containing rapid variations is the phenomenon of aliasing which causes waves beyond the resolvable limit of the grid to fold back across the Nyquist onto the resolvable waves near the Nyquist. This by itself is not a serious problem since we are only interested in a small number of ridges that are situated well away from the radial Nyquist. Typically, aliasing in linear problems is relatively harmless and usually only results in a slight increase in power near the Nyquist.

Interestingly however, in our calculations, Fourier transforms in the radial direction display spectral blocking (shown in figure 2.4), an effect that occurs in numerical solutions of non-linear equations, commonly seen in simulations of turbulence and other non-linear phenomena. It is seen in our computations because of the highly non-constant terms (in the solar case) of the Euler equations, density, pressure and sound speed, that pre-multiply the linear fluctuation terms, like the first term on the right-hand-side of equation (2.1). These non-constant terms act as conveyor belts across the radial spectrum, transferring energy between disparate wavenumbers, and eventually cause this aphysical energy build-up at the Nyquist. The energy accumulation occurs at a non-linear rate, rapidly posing a threat to the accuracy and stability of the calculation.

In order to dealias the variables, we apply the 11 point de-aliasing filter (Vichnevetsky & Bowles 1982) given in equation [2.18], where $\hat{u}_n$ and u_n are the filtered and unfiltered variables at grid point n, every few time-steps so that any growth near the Nyquist is suppressed. Because of the high order of the filter, the portion of radial spectrum of interest is left largely unaffected. Note that because of the varying sound speed, we can only apply the filter on the stretched grid over which the acoustic travel time between adjacent grid points is constant.

$$\begin{aligned}
\hat{u}_n &= a_0 u_n + \frac{a_1}{2}(u_{n-1} + u_{n+1}) + \frac{a_1}{2}(u_{n-2} + u_{n+2}) \\
&+ \frac{a_2}{2}(u_{n-2} + u_{n+2}) + \frac{a_3}{2}(u_{n-3} + u_{n+3}) \\
&+ \frac{a_4}{2}(u_{n-4} + u_{n+4}) + \frac{a_5}{2}(u_{n-5} + u_{n+5}) \qquad (2.18) \\
a_0 &= 0.753906,\ a_1 = 0.410155,\ a_2 = -0.234375, \\
a_3 &= 0.087890,\ a_4 = -0.019531,\ a_5 = 0.001953
\end{aligned}$$

2.5.3 CFL restrictions

The Courant-Friedrich-Lewy (CFL) condition determines the maximum size of the timestep based on spatial resolution and, in this case, sound speed. The timestep is limited by the more restrictive of the accuracy and stability conditions (see Hu et al., 1996). The accuracy condition requires that well resolved waves are captured to within accepted numerical error and the stability condition ensures that the highest resolved wavenumber is stable. Since waves travel at various angles, we must consider limitations due to the horizontal wavenumber as well.

The shortest wavelength that can be accommodated on the radial grid (without

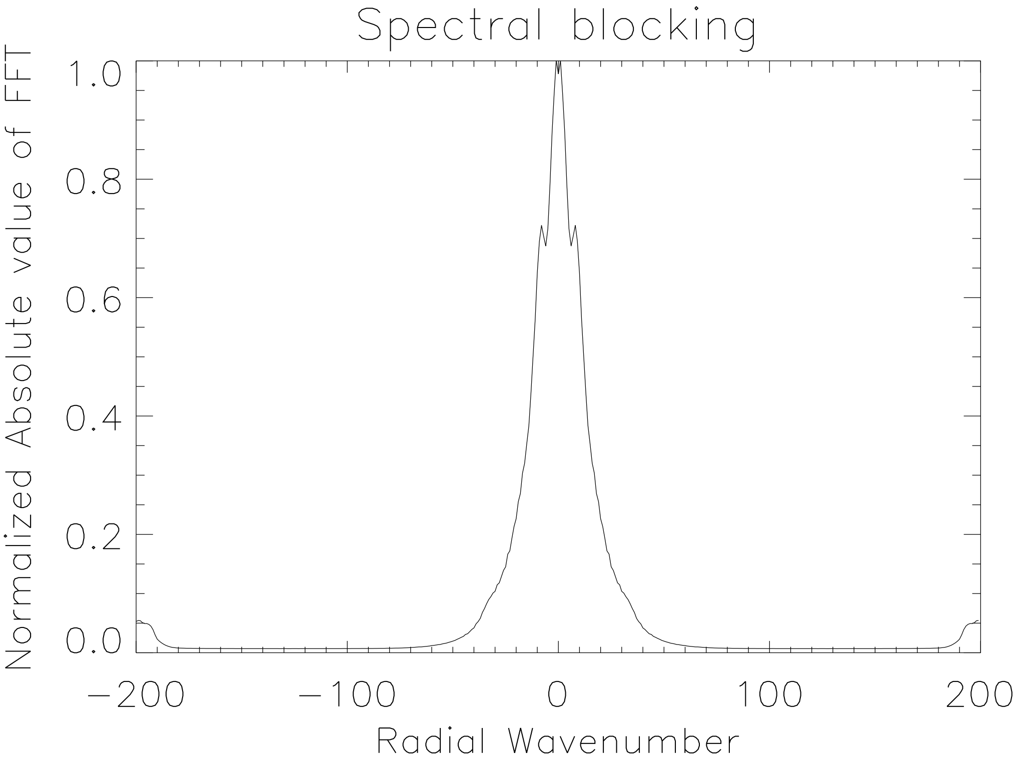

Figure 2.4 Spectral blocking in a linear simulation. This is a classic malaise affecting non-linear calculations, resulting in aphysical energy accumulation near and at the Nyquist. Although the amplitude at the spatial Nyquist (either end of the graph) is relatively small in this snapshot, the time evolution of this region of the spectrum is nonlinear.

any aliasing) is twice the largest grid spacing, which is the distance between the deepest two grid points. Since the spatial differencing scheme can only capture derivatives with wavenumbers in a given range, we introduce two relevant measures (e.g., Lele, 1992; Lui, 2003) used to describe this effect: the highest well-resolved wavenumber and the highest resolved wavenumber. The highest well-resolved wavenumber represents the largest wavenumber which is resolved accurately by the differencing scheme. The highest resolved wavenumber is the maximum effective wavenumber of the spatial differencing scheme. The highest well-resolved radial wavenumber, which we refer to as k_w, and highest resolved radial wavenumber, k_{wn} for the choice of our differencing scheme are $k_w h = 1.7$ and $k_{wn} h = 2.0$, where h is the local radial grid spacing. The highest well-resolved horizontal wavenumber (for a spectral method, there is no difference between the highest resolved and highest well-resolved wavenumbers) is given by

$$k_{h,max} = \frac{\sqrt{l_{max}(l_{max}+1)}}{r_{in}}, \tag{2.19}$$

where l_{max} is the spherical-harmonic bandwidth. The timestep restriction is given by

$$\Delta t \leq \min\left[\frac{L}{(ck_w)_{max}}, \frac{R}{(ck_{wn})_{max}}, \frac{L}{(ck_h)_{max}}\right], \tag{2.20}$$

where R and L are limited by the boundary of the stability foot-print and the accuracy limit respectively (Hu et al., 1996). The time-stepping scheme adopted in this calculation is accurate and stable for $L \leq 1.35$ and $R \leq 3.54$, and therefore the largest allowed timestep is given by

$$\Delta t = \min\left[1.67\left(\frac{h}{c}\right)_{min}, \frac{1.35}{\sqrt{l_{max}(l_{max}+1)}}\frac{r_{in}}{c_{max}}\right], \tag{2.21}$$

where h and c are functions of radius and $c_{max} = c(r_{in})$ is the maximum sound speed in the domain. In practice, we have succeeded in using larger timesteps than that allowed by the CFL condition; in most simulations, we use $\Delta t = 4$ seconds.

2.5.4 Lower boundary issues

Pushing the lower boundary deep (like $0.24R_\odot$) is certain to ensure a tight CFL restriction, especially if there is a horizontal background structure (like a density inhomogeneity or a flow) that interacts with the acoustics. Consider equations (2.19) and (2.20) - as one proceeds deeper, the inner radius r_{in} reduces and sound speed (see Figure 2.1) increases. The timestep restriction becomes tighter and consequently the computation becomes very expensive. We have therefore actively made the choice of a spherically symmetric background model with no flows at this depth. Consider also the fact that a large number of waves have already undergone total internal refraction. For example, at a frequency of 5000 μHz, the highest l that penetrates a depth of 0.24 $R_\odot$ is 10, which means that when determining the CFL condition from equation (2.21), one need not use the entire spherical bandwidth. In other words, one may replace l_{max} by $l_{max}(r)$ denoting the highest l that can propagate at a given radius (given by Eq. [2.9]), a number which deep in the sun is much smaller than the bandwidth. The resulting time-step increase one can obtain by applying this property can be as large as a factor of 2 depending on l_{max} and the number of radial gridpoints.

2.5.5 Buffer layer

It was mentioned in §2.3 that the transmitting boundary conditions employed in this calculation reflect a large percentage of waves that impact it at significant angles (as opposed to purely radially propagating waves). The effect poses a serious threat to both the stability and accuracy of the simulation because of this aphysical reflection of waves. To deal with this problem, we insert a buffer layer adjoining the upper boundary in which upward traveling waves are significantly damped out prior to reaching the upper boundary. This ensures that even if these waves are reflected at the boundary, they will have to propagate through the buffer layer again to reach the computational region of interest. This layer serves to diminish the amplitudes of these aphysical waves to insignificance. Thus, in order to prevent unwanted reflections, we introduce buffer layers at each end of the computational domain via the damping term $\Gamma(r)\mathbf{v}$ in equation (2.2).

One problem associated with using such a lower boundary buffer layer is in dealing with waves that have inner turning points located in the midst of the buffer zone. These waves essentially sample the buffer zone and undergo a total internal reflection only to re-emerge corrupted by this aphysical layer. The task then is to identify and filter out these waves. As explained in §2.4 and specifically in equation (2.9), we can identify the frequency-wavenumber range of waves which propagate to this depth and nullify the corresponding part of the $k - \omega$ spectrum.

2.5.6 Convective instabilities

The Brunt-Väisälä frequency indicates whether a medium is unstable to convection. It is given by (e.g., Christensen-Dalsgaard, 2003, chap. 3)

$$N^2 = g\left(\frac{1}{\Gamma_1}\frac{\partial \ln p}{\partial r} - \frac{\partial \ln \rho}{\partial r}\right), \tag{2.22}$$

where g is gravity, N is the Brunt-Väisälä frequency and Γ_1 is the first adiabatic exponent, defined in equation (2.4). The solar convection zone extends all the way from roughly $0.7R_\odot$ to the surface. For purposes of discussion, we shall divide the convection zone into two regions, $0.7R_\odot < r < 0.996R_\odot$ where timescales of convective growth are considerably larger than acoustic timescales (5 minutes) and $0.996R_\odot < r < 1.0003R_\odot$ where the convective growth rate and acoustic timescales are about equal. Consider the inner region with slowly growing instabilities first. Since we are dealing with a linear system, it might at first sight seem odd that although we restrict acoustic excitation to the bandwidth $2000-5500$ μHz, we still see instabilities at much lower frequencies. The reasons for this are the finiteness of the excitation time series, which results in the broadening of the frequency response, and numerical round-off errors, which act as broadband sources.

The outer convective envelope introduces difficulties which must be treated with greater care. As can be seen in Figure 2.5, the instability time-scales very close to the surface coincide with the center of the acoustic bandwidth. Since our interest lies in capturing the interaction of the acoustics with the background dynamics and not in the direct computation of the convection, we must devise a means to remove this

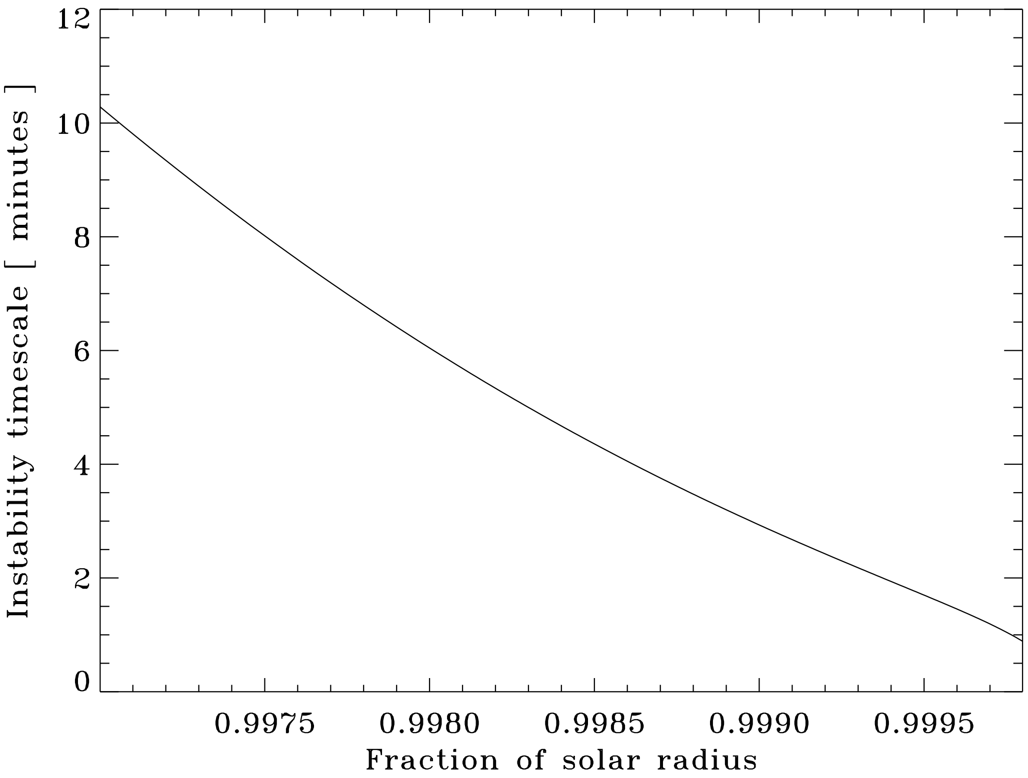

Figure 2.5 Convective instability timescales, ($1/|N|$ in minutes) as a function of the non-dimensional radius. It can be seen that growth rates of the convective instabilities lie in the same range as the time-scales associated with the acoustic waves. The instability arises as a direct consequence of the super-adiabaticity of the background model, and since we are not modeling the nonlinear physics of convection, it is crucial that we prevent this linear instability (described in §2.5.6) from affecting the acoustic signal.

instability without affecting the acoustics. One way to accomplish this is to alter the Brunt-Väisälä frequencies. A crucial requirement is that the acoustic impedance of the surface layers not be changed by much, since all the acoustic reflection occurs in and around these layers.

It is difficult to alter the timescales of convective growth in the near-surface layers of model S without rendering the background model inconsistent. We have therefore replaced the near-surface layers given by model S, more specifically, the region above $0.98R_\odot$, with an alternative empirical description that satisfies requirements of hydrostatic consistency, convective stability and preserves the crucial reflective property of the solar atmosphere. Equally essential is that the atmosphere be a smooth extension to the interior (given by model S). Some properties of the empirical model are shown in Figures 2.6 and 2.7 and listed in appendix A; more details may be found in Hanasoge (2006). It should be noted that this modification of the background model allows the temporal window of the simulation to be extended to several days; longer simulations, of the order of weeks, are still susceptible to the marginal super-adiabaticity exhibited by the interior.

2.6 Validation

An important indicator of solar wave structure (acoustic, surface-gravity) is the power spectrum, which embodies the frequency-wavenumber response of the system to a specific excitation. It is typically shown as the squared Doppler velocity as a function of ω and l. In other words, it is the frequency-wavenumber response of the system to a specific excitation. It can also be understood as a depiction of the resonant modes of the model. A mixture of surface-gravity and acoustic modes appear when solar surface (Doppler) velocities are analyzed. As stated before, the acoustic modes possess maximum power in the frequency range of $2000-5500$ μHz. In terms of spatial wavenumbers, the solar power spectrum stretches to extremely high harmonic orders (several thousand) which are at present computationally infeasible. The immediate aim is to replicate some part the low to medium-l ($0 < l < 400$) acoustic spectrum of the sun in the frequency range described above. We achieve this by exciting waves only

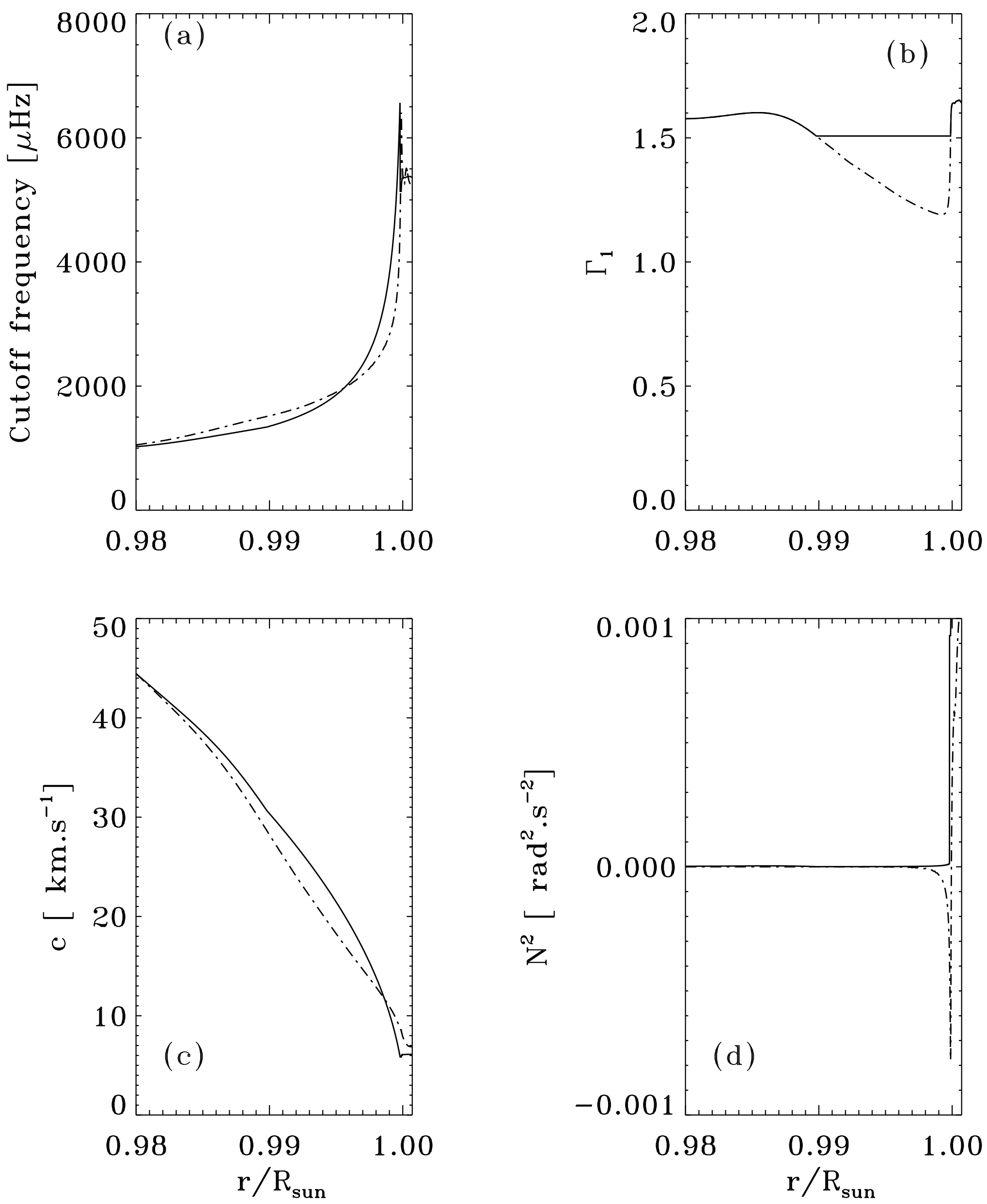

Figure 2.6 These panels show a comparison between the properties of the atmosphere given by model S (dot-dash line) and the artificial model (solid line) used in the computation. The horizontal coordinate of all the above panels is the fractional radius, $r/R_{\odot}$. Panel (a) shows the cutoff frequency dependence with radius; the reflective property of model S is recovered quite accurately by the artificial model. Panel (b) is a comparison of the first adiabatic exponents; Γ_1 has been altered to render the artificial atmosphere convectively stable. Panel (c) shows sound speed dependence with radius; the layer extending from $0.9998R_{\odot} \leq r \leq 1.0007R_{\odot}$ is isothermal and therefore the sound speed is constant in that region. Panel (d) displays the all-important measure of convective stability, the Brunt-Väisälä frequency; it can be seen that the artificial model is sub-adiabatic in the near surface layer, thus ensuring the convective stability of the outer layers.

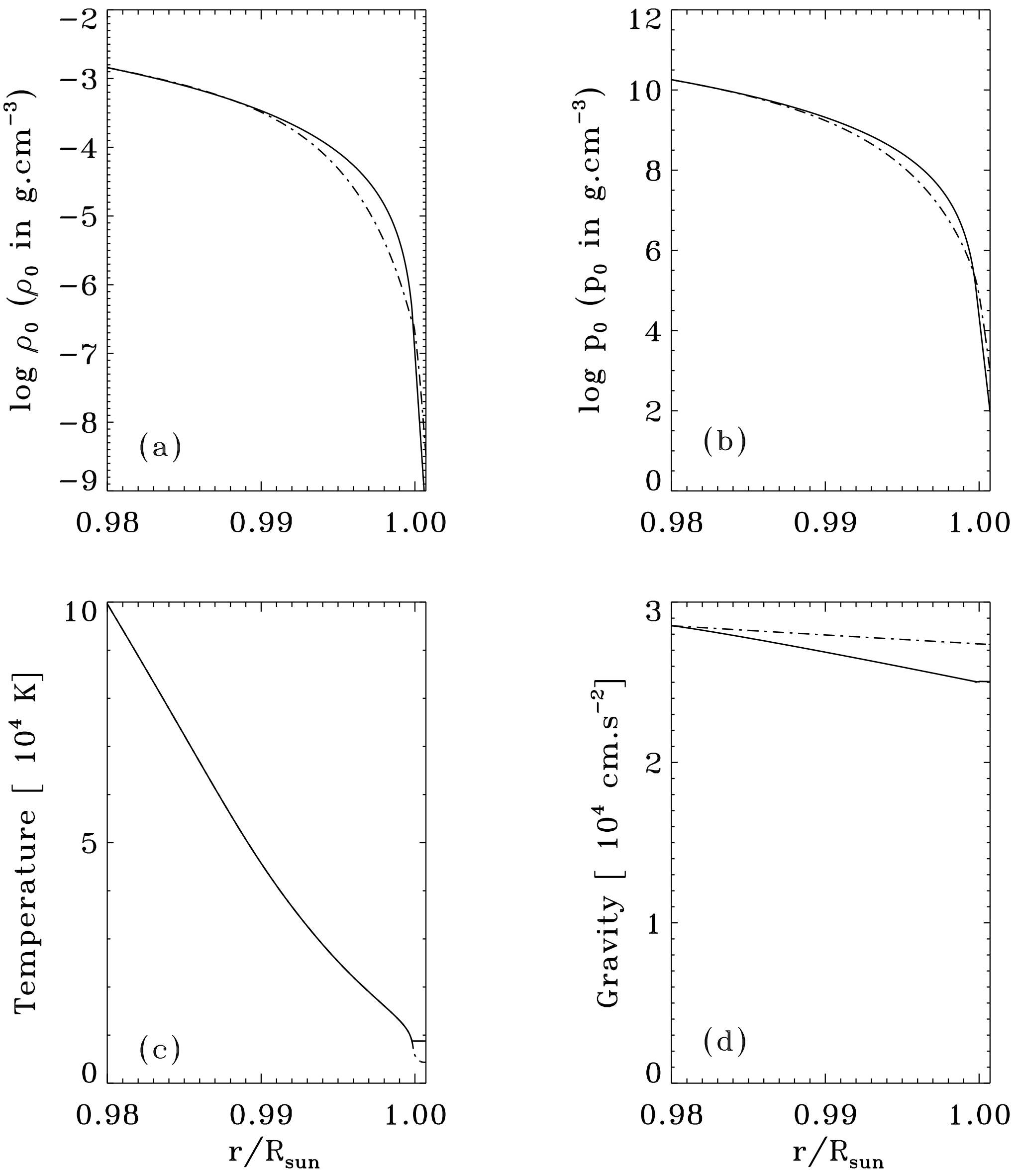

Figure 2.7 These panels show a comparison between the properties of the atmosphere given by model S (dot-dash line) and the artificial model (solid line) used in the computation. The horizontal coordinate of all the above panels is the fractional radius, $r/R_{\odot}$. Panels (a) and (b) show the variation of the logarithmic density and pressure with radius; it can be seen that the two models are quite similar. Panel (c) is a comparison between temperature profiles - the isothermal nature of the outermost layers of the artificial model is visible. Panel (d) shows gravity dependence with radius; the gravity profile of the artificial model is seen to decay more rapidly than that of model S.

in the specified frequency band. Figure 2.8 is the log power spectrum obtained from a 24 hour long simulation with transmitting lower and upper boundaries placed at $0.24R_\odot$ and $1.0002R_\odot$ respectively. Note that because the short time-scale convective instabilities present in the atmospheric region of the background model have been removed, we see no power at frequencies below 2000 μHz.

2.6.1 ADIPACK

A convincing validation of the model is an independent theoretical computation of the resonant modes followed by a comparison with the simulation. ADIPACK (Christensen-Dalsgaard & Berthomieu, 1991) is a software package that may be employed to produce resonant mode data for the spherical shell under investigation. The simulation was performed in a shell that extended from $0.2R_\odot$ to $0.975R_\odot$ with a transmitting lower boundary and a radially oscillating upper boundary. The eigenfrequencies for this simulation were extracted and compared with results from ADIPACK for a similar model. The comparison result in Figure 2.9, displays good agreement between the ADIPACK modes and the simulation.

2.6.2 Shifts in frequencies due to rotation

We now discuss the validation of the model in the presence of a background rotation profile. To ensure that these frequency shifts can be observed in a short simulation, we artificially amplify the average solar rotation rate by a factor of 10,

$$\frac{\Omega}{2\pi}(r,\theta,\phi) = 4300 \text{ nHz}. \tag{2.23}$$

In the absence of background flows, resonant wave-mode frequencies are characterized only by l, possessing no dependence on m. In general, flows induce changes in the resonant frequencies and specifically, rotation splits the mode frequencies by $\pm m\Omega$, where m is the azimuthal order, depending on whether the modes propagate prograde or retrograde with respect to the direction of rotation. We display the frequency shifts for the $l = 52$ set of modes in Figure 2.10. The frequency resolution of this simulation

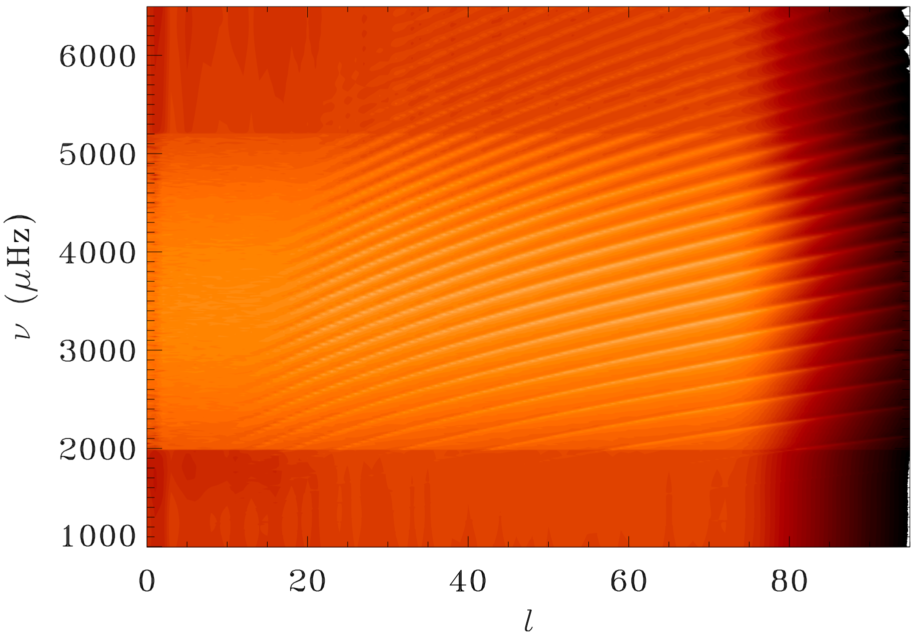

Figure 2.8 Logarithmic power spectrum for a model that extends from $0.24 - 1.00033R_{\odot}$. The excitation spectrum is a band that approximately encompasses $2000 - 5500$ μHz in frequency and $0 - 80$ in l. The highest l's contain little or no power to avoid spatial aliasing. Modes with inner turning points deeper than the lower simulation boundary are absent from this spectrum. Note that because the short time-scale convective instabilities have been removed, as described in §2.5.6, we see no power at frequencies below 2000 μHz. This spectrum was extracted from a 24-hour-long simulation.

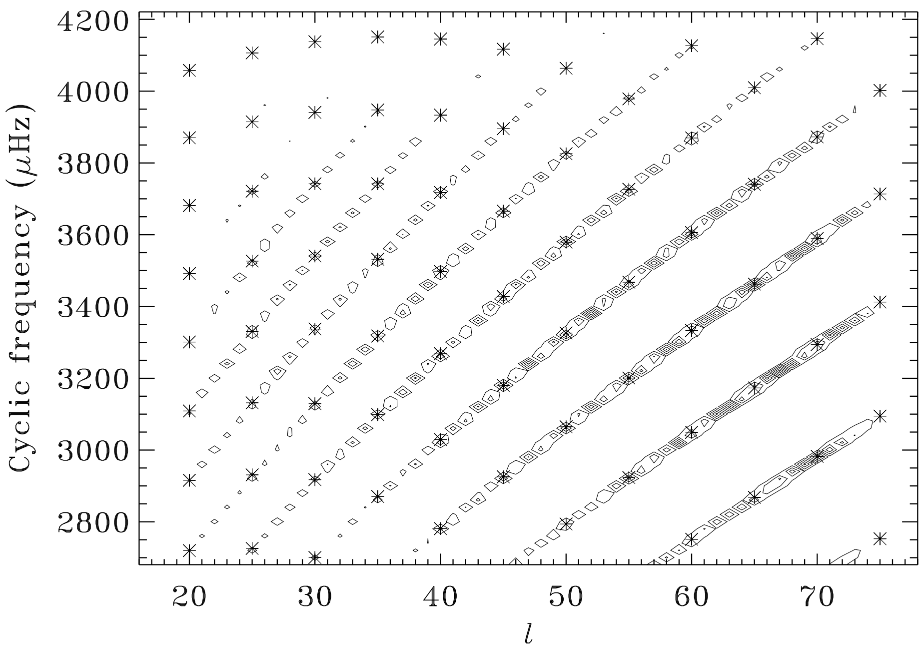

Figure 2.9 Comparison between resonant wave modes computed by ADIPACK and the simulation. The modes extracted from the simulation are depicted as contours of power and the ADIPACK frequencies for this model are shown as stars. Note that for ease of comparison, only one in every five modes that are predicted by ADIPACK are depicted. The mode frequencies, located at contour centers are seen to match closely the frequencies given by ADIPACK. The ridge shapes of the power spectrum extracted from the simulation agree well with those predicted by ADIPACK.

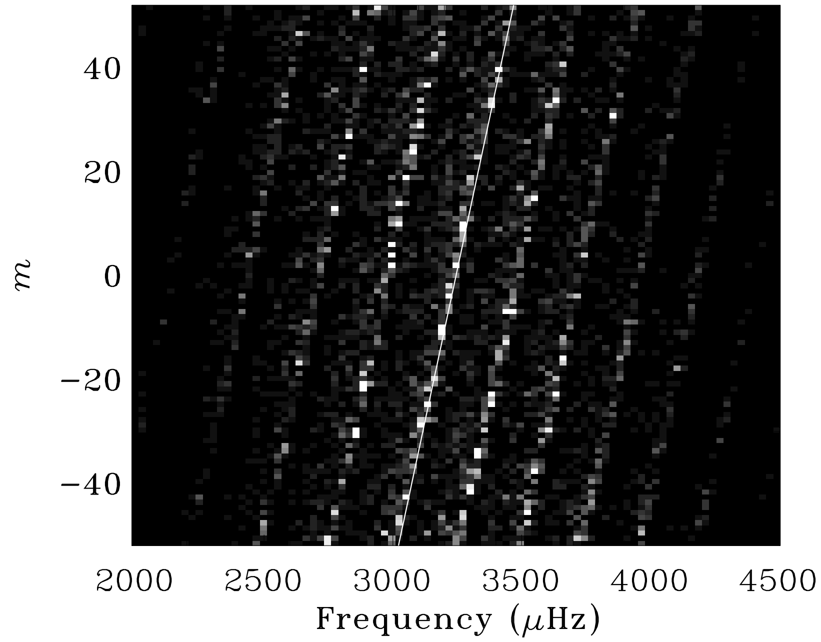

Figure 2.10 The $m - \nu$ power spectrum with $l = 52$ for a simulation with pure rotation, the rate being $\Omega/2\pi = 4300$ nHz. The solid line shows the analytically calculated trend in the frequency shifts. The frequency resolution of this simulation was 28 μHz. In the absence of background flows, contours of maximum power would be lines parallel to the y-axis. Rotation causes frequency splitting, shifting pro-grade modes by $+m\Omega$ and retrograde modes by $-m\Omega$, as indicated by the solid line. Note that as expected, all the (shifted) lines are parallel.

was 28 μHz. The frequency shifts extracted from the simulation match the predicted shifts to within the allowed frequency resolution.

2.7 Results and analyses

2.7.1 Travel times

Using full disk measurements, we were able to extract travel times (see Figure 2.7.1); a comparison between the South pole data (Schrijver et al., 1996) and a simulation datacube is presented. It can be seen that a large fraction of the features are reproduced in the simulation. It is important to note that we do not make a direct comparison between the simulation and actual data since we do not incorporate the full physics in the computation. Also, since the simulation domain extends only down to $r \sim 0.24R_\odot$, we see a phase speed filter like effect that essentially removes the part of the wave-spectrum that penetrates deeper than $0.24R_\odot$. The simulated data shows some ringing effects because the source spectrum in this case is somewhat sharply localized between 2 and 5.5 mHz.

It can also be seen that around the disk edge, the South pole data shows no signal whereas the ridges can be seen clearly right up to the limb in the simulation data. (A)-(C) amongst other ridges (with positive slopes) represent signatures of wave modes that circumnavigate the sun with differing numbers of bounces; several ridges seen in the data are not present in the simulation because these waves propagate deeper than the inner boundary. The ridges (D)-(G) amongst others (with negative slopes) represent wave modes with more complex reflection patterns (some mention of this in Duvall et al., 1993).

2.7.2 Correlations

Figure 2.12 compares time-distance correlations for MDI medium-l data with simulation data. It can be seen that correlations for a given time and distance are approximately the same in both cases. We do not make direct comparisons between the two datasets because we use an altered model of the Sun in simulations. It is interesting to note that the values of the correlation coefficients are comparable. This indicates that the source excitation model we apply is representative of the solar acoustic excitation mechanism in this range of wave-numbers.

2.7.3 Line Asymmetry

Power spectra of the Sun are obtained either through measurements of fluctuations in velocity or in intensity. Mode shapes and line asymmetries in the $l-\nu$ power spectrum are a strong function of source depth (e.g. Rast & Bogdan 1998), with velocity and

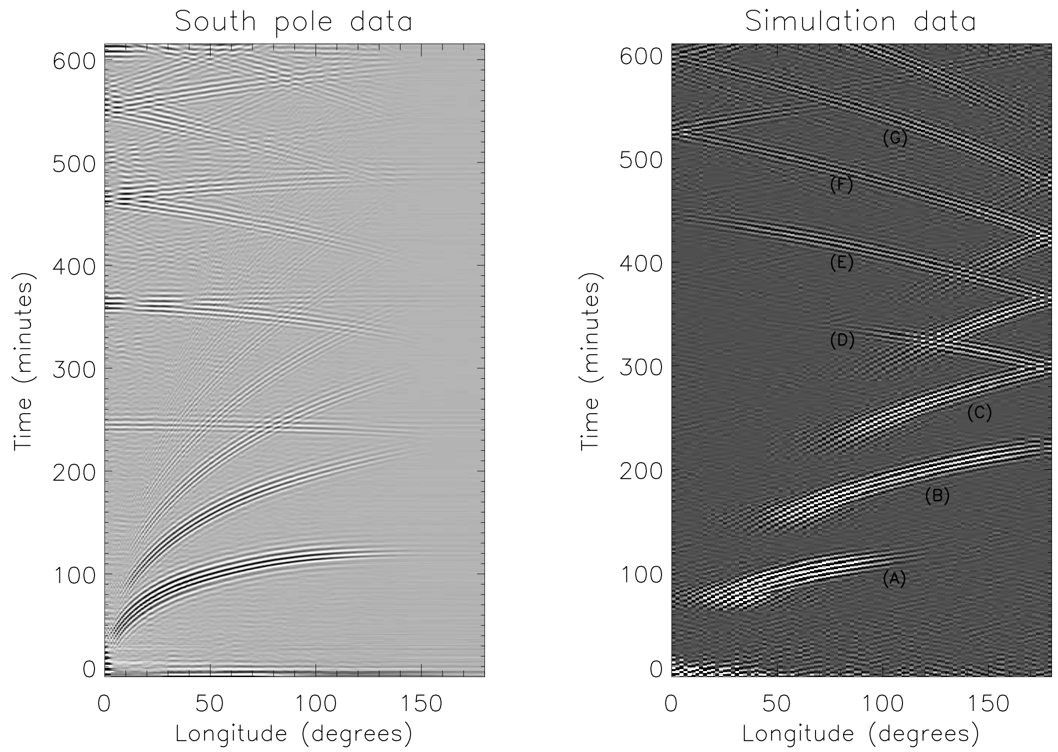

Figure 2.11 Comparison of various ridges obtained from South pole (data first described in Schrijver et al., 1996) and simulated data.

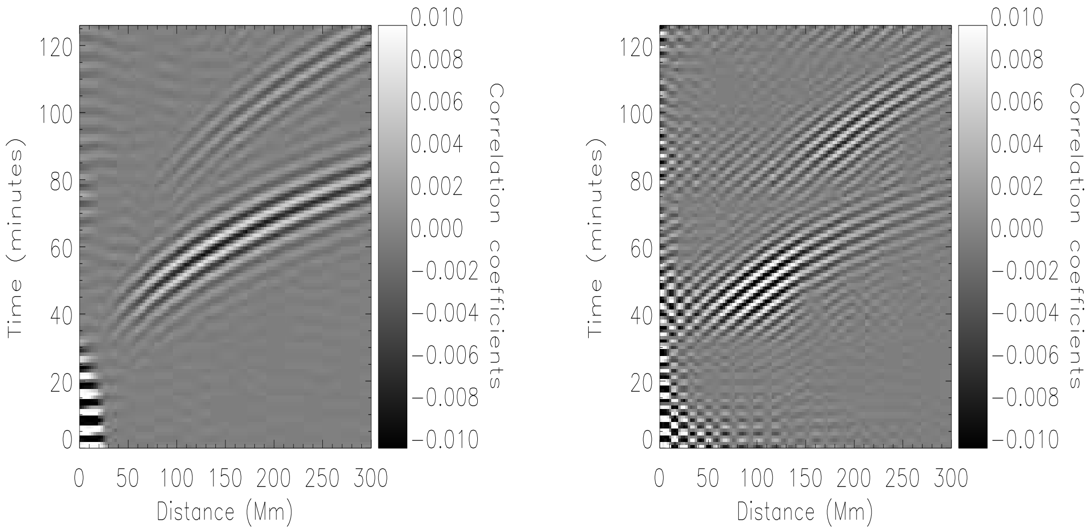

Figure 2.12 Displayed are correlations obtained from MDI Medium-l data on the left panel and simulation data on the right panel. The x-axis is distance in Mega-meters, the y-axis time in minutes and the scale corresponds to the correlation coefficient.

intensity lines displaying phase differences in the asymmetries. By choosing to place sources very close to the surface, we obtain velocity line asymmetries similar to those seen in the Sun, higher on the low frequency side of the mode. By assuming a direct correlation between temperature and intensity fluctuations, Rast & Bogdan (1998) have demonstrated that purely adiabatic oscillations (as in our simulations) result in identical intensity and velocity line asymmetries. An artefact of the simplicity of our adiabatic model and in direct contrast to the Sun, we also observe no phase difference between velocity and intensity asymmetries (figure 2.13).

2.8 Detectability of interior convection

Many investigators have attempted to detect deep convection (e.g., Zhao & Kosovichev, 2004), with some efforts focused on isolating giant cell signatures (e.g., Beck, Duvall and Scherrer, 1998) from solar data. Despite these efforts, giant cells have

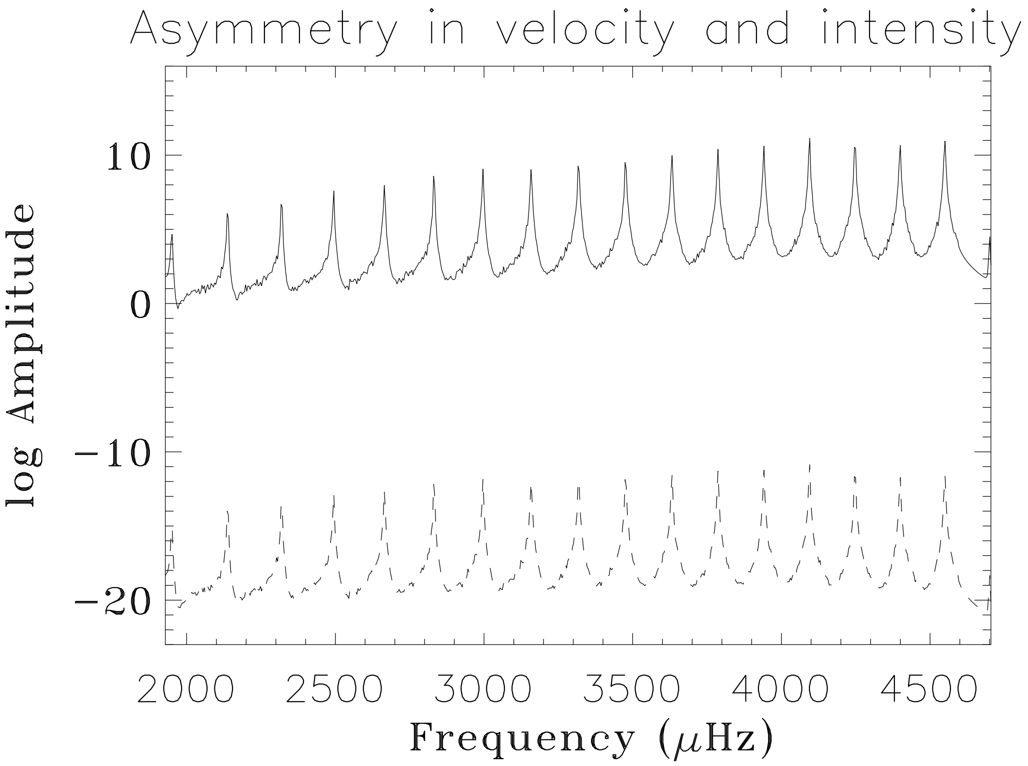

Figure 2.13 Line asymmetry for wave modes with spherical harmonic degree $l = 30$. The mode amplitude is expressed in arbitrary units. The solid line shows modes captured in the velocity spectrum and the dashed line shows modes in intensity (essentially temperature fluctuations). These lines are asymmetric at low frequencies (< 4000 μHz) and become more symmetric as frequency increases (~ 4200 μHz).

not been observed, perhaps due to the relatively small surface velocities they are estimated to possess (e.g., van Ballegooijen, 1985). Furthermore, there have been no convincing observations relating to sub-surface convective activity below the supergranular layer. Swisdak & Zweibel (1999) have shown that solar eigenfrequency shifts may also be poor diagnostic agents because of their weak sensitivity to large scale convection, the effects of which appear only at the second order.

We show in this paper that time-distance helioseismology (Duvall et al., 1993) applied to extract signatures of deep convection may prove to be a promising technique. Time-distance helioseismology is based on measuring wave travel times from one surface location to another to investigate properties along the wave propagation pathways between these locations. In rough summary, signals at these two regions are cross-correlated and analyzed to recover the wave travel times. There are two principal diagnostic agents, the mean travel time and the travel-time difference, the former being predominantly sensitive to sound-speed perturbations and the latter to flows.

It is known that very small thermal perturbations are sufficient to sustain deep convective activity. Convective velocities in the interior, estimated from simulations and otherwise, are placed at 100 ms^{-1}, which in terms of travel-time shifts is arguably a stronger effect than sound speed fluctuations, a direct effect of the convection induced thermal fluctuations. Keeping this in mind, we analyze only travel-time differences, which are sensitive to flows. In order to estimate these travel-time differences, we perform a calculation of a ray propagating through a model of solar convection, taken from the Anelastic Spherical Harmonic (ASH) code (Miesch et. al., 2000). Such a calculation also shows us the correlation between the travel-time maps and the convective velocities that the ray samples.

2.9 Ray calculations

To compute travel-time differences, $\delta\tau$, we use a standard method (e.g., Giles, 2000) that applies the following equation:

$$\delta\tau = 2\left[\int_{r_1}^{r_2} \frac{u_h}{c^2}\left(\frac{\omega^2 r^2}{l(l+1)} - c^2\right)^{-\frac{1}{2}} dr + \int_{r_1}^{r_2} \frac{u_r}{c^2} dr\right], \qquad (2.24)$$

where r is the radius, u_h is the horizontal flow velocity component in the direction of the propagating ray, u_r is the radial velocity component along the ray path, ω the circular frequency of the acoustic wave, l the spherical harmonic order, c the sound speed, r_1 the lower turning point and r_2 is the upper turning point. For calculations presented here, we approximate $r_2/R_\odot = 1$. The first and second terms on the right-hand-side denote travel time contributions from the horizontal and radial components of the flow, respectively.

2.9.1 Deep convection model

The ASH code computes acoustics-free convection in a spherical shell. By neglecting the rapidly propagating acoustic waves in the convection zone, Miesch et. al. (2000) are able to obtain a significant increase in the computational timestep of the convection simulation. For the ASH profile used in the ray calculation, the computational boundaries were placed at $0.76R_\odot$ and $0.96R_\odot$ and act as no-slip, impenetrable walls. Because of these boundary conditions, the radial velocity vanishes at both ends and it is important to keep this aspect in mind while interpreting the results from the ray calculations. The latitudinal velocity at a radial layer from the ASH simulation is shown on the upper panel of figure 2.14.

2.9.2 Surface convection model

Acoustic waves spend the longest time in the near-surface layers. These waves are strongly biased by supergranular activity in the sub-photospheric regions. In order to take this effect in account, we model supergranules by cell-like structures with

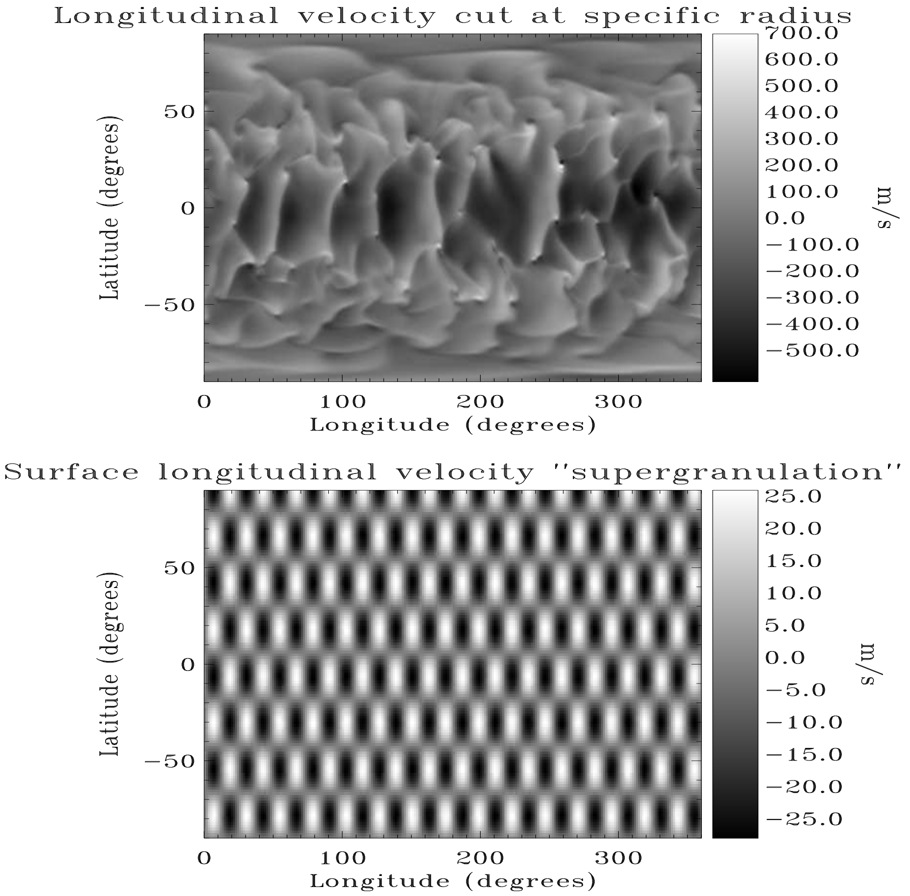

Figure 2.14 Sections of velocity profiles, dimensions of the scale are in m/s. The upper panel shows the longitudinal velocity taken from the ASH simulation at a single radial cut, corresponding to $r = 0.92R_{\odot}$. The lower panel shows the cellular pattern exhibited by the longitudinal velocity at the surface, a crude model for supergranular activity. We use 4 times as many 'supergranules' in our calculations.

an average horizontal cellular size of 30 Mm and depth of 15 Mm. Each unit acts a 'convective cell', with velocity profiles chosen to satisfy the continuity equation, $\boldsymbol{\nabla} \cdot (\rho_0 \mathbf{v}) = 0$ (e.g., Swisdak & Zweibel, 1999), where ρ_0 is the solar density, $\mathbf{v}$ the vector velocity and $\boldsymbol{\nabla}\cdot$ the divergence operator. The maximum velocity of a 'supergranular' cell is 200 ms^{-1}. The surface velocity profile is shown in figure 2.14.

For these calculations, we have taken a snapshot in time from the ASH simulation and apply a constant (in time) surface convection model. One of the reasons we may do this is the decoupling of timescales between the acoustics (5 minutes) and the turnover time of convective cells (several hours to days). Also the long convective cell lifetimes in comparison to the length of the time series of solar data we use to recover the travel-time differences, allows us to invoke the assumption of time constancy.

2.9.3 Travel times

To determine the travel-time difference associated with a point at a certain depth, we first center an annulus around the surface projection of the desired point. The diameter of the annulus is equal to the horizontal distance traversed by a wave whose inner turning point is r_1, as described in equation (2.24). As shown in figure 2.15, we then divide the annulus into 4 equal quadrants, two horizontal quadrants ($[2\pi - \pi/4, 2\pi) \cup [0, \pi/4)$ and $(3\pi/4,\ 5\pi/4]$), and two vertical quadrants ($[\pi/4, 3\pi/4]$ and $(5\pi/4, 2\pi - \pi/4)$). The travel-time differences are divided into two categories, east-west and north-south, based on whether the corresponding rays lie in the horizontal or vertical quadrants, respectively. All the east-west travel times are averaged to give a mean east-west travel-time difference. A similar procedure is implemented for the north-south travel-time difference. When dealing with solar data, this procedure helps in reducing the noise.

We use multiple rays with identical frequencies $\omega/2\pi = 3.2$ mHz but differing inner turning points. For a fixed ω, the inner turning point moves closer to the surface as the degree l increases. In figure 2.16, we show a sample east-west travel-time map for a ray with $l = 128$. On the left panel in figure 2.17, we show the dependence of the RMS travel times (east-west and north-south) with the inner turning point of the

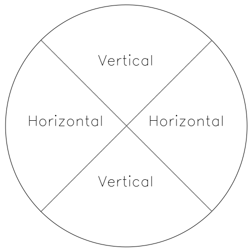

Figure 2.15 Quadrants used for travel time averaging. East-west rays are defined as those which propagate to from one horizontal quadrant to the other. Similarly, rays that span the vertical quadrants are north-south propagating. After computing the travel times for rays propagating in various directions, they are then averaged and classified according to the quadrant in which they propagate.

ray.

RMS travel time differences are shown on the left panel in figure 2.17. The horizontal co-ordinate represents the inner turning point of the ray used to recover these travel times. In general, one may expect that as the coherence of velocity map decreases, i.e. the velocity power is spread over a large range of wave-numbers, travel-time differences and correlations will also decrease. As can be seen in figure 2.18, the longitudinal velocity power peaks at very low l and decays rapidly with increasing l, while the latitudinal velocity power decays more slowly. The greater clustering of power in the convective longitudinal velocity than in latitudinal velocities may be the cause of relatively weaker scattering of waves propagating in the longitudinal direction, possibly leading to the differences in east-west and north-south travel times. Furthermore, it may be seen from figure 2.19 that the longitudinal velocity is consistently larger than latitudinal velocity over the simulation domain, contributing to the larger magnitudes of east-west travel-time differences.

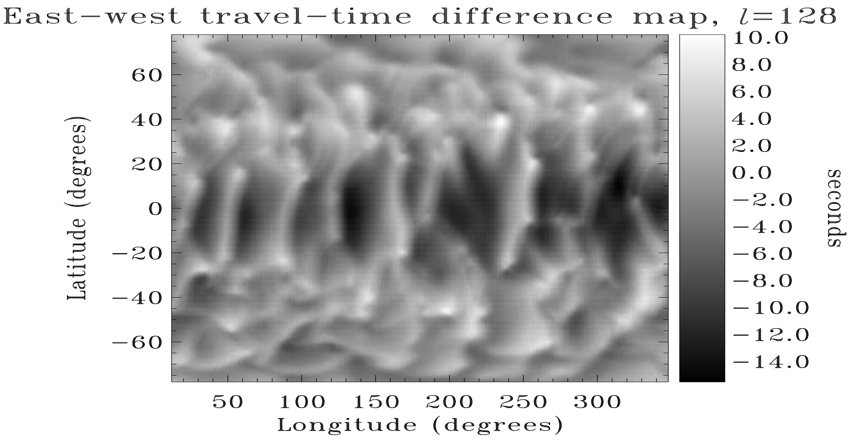

Figure 2.16 East-west travel-time difference map for a ray with $\omega/2\pi = 3.2$ mHz and $l = 128$ (inner turning point $r_1 = 0.92R_\odot$). The correlation of the travel-time map with the longitudinal velocity map (see figure 2.14) at the inner turning point radius is around 0.95, indicating that convective signals are strongly imprinted onto the travel-time differences.

2.9.4 Correlations

The east-west and north-south travel-time difference maps are then correlated with the longitudinal and latitudinal velocity maps at the lower turning point of the ray in question. Correlations as a function of the inner turning point of the ray are shown on the left panel in figure 2.17. The correlations decrease as rays with deeper inner turning points are used. It must be noted that the east-west correlations are not always larger than the north-south correlations, as was the case with RMS travel-time differences (see left panel, figure 2.17). It is interesting to note that the correlation of the shallow rays is very high, perhaps indicating that the convective signals are so well preserved in the travel times that inversions are not needed to recover convective structures at this depth.

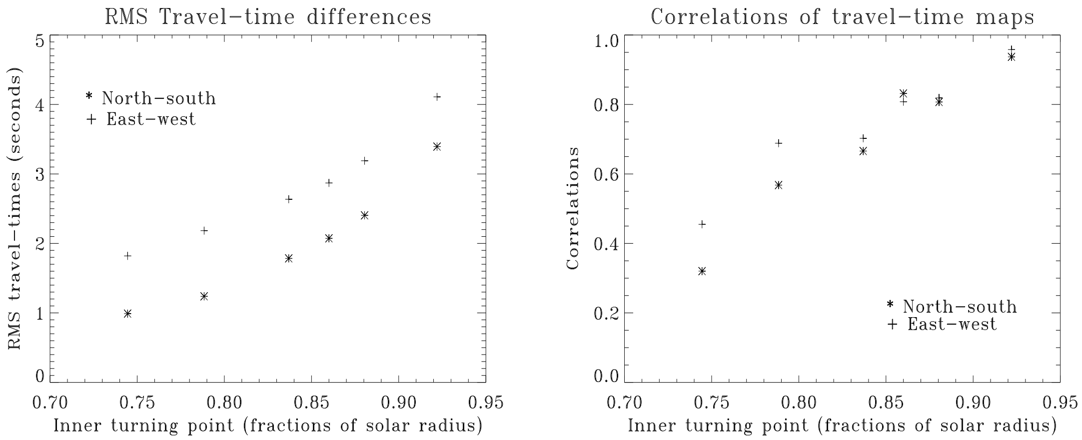

Figure 2.17 The RMS east-west and north-south travel times on the left panel and correlations with corresponding velocity maps on the right panel, as a function of the inner turning point of the diagnostic ray. It can be seen that the east-west RMS travel times are consistently larger than the north-south travel times for a given ray, sometimes by as much as a factor of 2. The correlations do not follow such a clear pattern though.

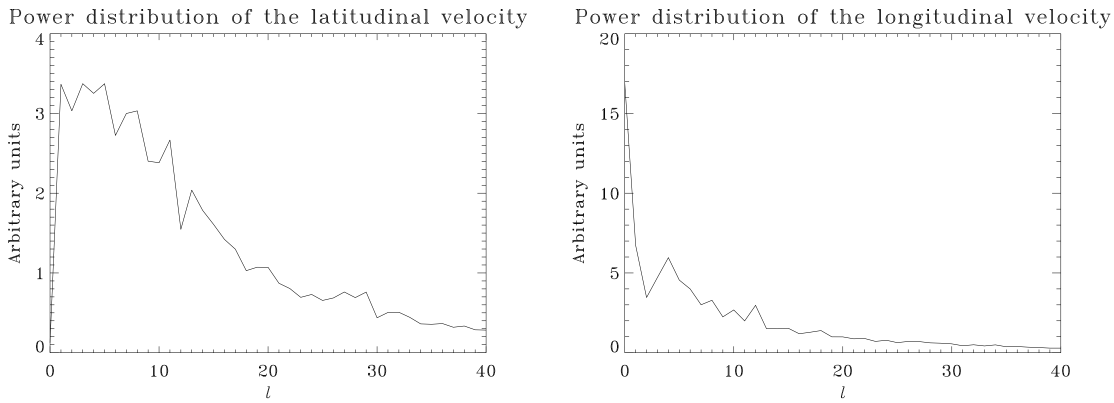

Figure 2.18 Average power of convective velocities from the ASH simulation (in arbitrary units) for each degree, l at $r = 0.92R_\odot$. While the power increases from the bottom of the domain to the top, the distribution profile is almost constant with radius. The variation of power with wavenumber indicates the extent of the scattering caused by the convection on the propagating rays. The longitudinal velocity power is strongly focused around $l = 1$, indicating that the travel times will preserve the velocity structure of the convection.

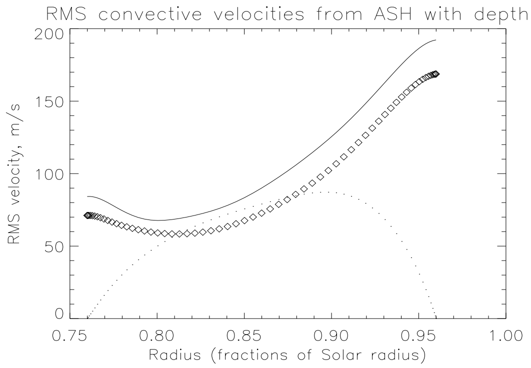

Figure 2.19 RMS convective radial, latitudinal and longitudinal velocities from the ASH simulation, as a function of depth. The solid line shows the longitudinal RMS velocity, the dots show radial velocity and the symbols depict the latitudinal RMS velocity.

2.10 Summary and Conclusions

A method to perform *differential* studies of the effects of flows and asphericities on the acoustic wavefield in full spherical geometry has been proposed. We have designed a technique to attempt the *forward* problem of helioseismology by performing linear acoustic simulations in an appropriately perturbed solar-like spherical shell. The utility of developing a means to independently test the ability of a helioseismic technique to probe various interior phenomena cannot be understated. From a practical standpoint, this technique is useful in understanding signatures of large scale phenomena such as meridional flow or the tachocline, and important in calibrating techniques that depend inherently on the geometry being spherical. Moreover, various systematics such as center to limb travel-time variations and fore-shortening can be investigated, given the availability of vector velocities and a 360^o view of the sphere.

In the past, there have been tests of helioseismology (for example, see Jensen et al., 2003) that have involved computations of acoustic wavefields but none have been performed in spherical geometry. From a practical standpoint, this technique is useful in understanding signatures of large scale phenomena such as meridional flows or the tachocline, and important in calibrating techniques that depend inherently on the geometry being spherical. Moreover, various systematics such as center to limb travel-time variations and fore-shortening can be investigated, given the availability of vector velocities and a 360^o view of the sphere.

We have discussed some of the issues associated with a computation of this kind, methods to overcome them and various techniques used in the validation process. The presence of a varying background medium introduces several complications that affect the stability and accuracy of the calculation. For example, the choice of an appropriate radial grid is somewhat crucial to the accuracy of the calculations given a motivation to minimize computational cost. Wave propagation in a such a medium is quite different in comparison to media that traditional aero-acoustic computations are accustomed to. Of course, the side-effects of a changing base state can ease and hinder the computation as has been noted.

We have demonstrated a way of filtering out waves based on their inner turning points, a technique of avoiding tight CFL restrictions and of circumventing instabilities created by an unstable background model. Important to a calculation of this kind is the need to validate the results. We have shown the utility of the process of extracting resonant modes of the domain and techniques to calculate the modes theoretically. The theoretical calculations confirmed the results of the numerical computation.

Observing interior convection in the Sun is a very exciting prospect. If we are indeed able to observe these convective cells, even if they are relatively close to the surface, we will be able to understand if current models accurately predict the characteristic sizes of these cells and the associated convective velocities. If we are to believe that the ASH simulations are representative of the solar convection zone, then from the results we obtain, convective signals are strongly imprinted onto the travel-time difference maps. The correlations we obtain in the near-surface regions are so high (~ 0.95) that inversions are not necessary to recover the structure of convection at this depth. In terms of real data, we will extract travel times using the deep-focusing technique described in Duvall (2003).

Chapter 3

Near-surface oscillations

3.1 Introduction†

For almost two decades, methods of local helioseismology (e.g, Hill, 1988; Braun, Duvall, & Labonte, 1987) have been applied to infer properties of the solar interior with varied degrees of success (for a comprehensive review, see Gizon & Birch (2005)). The predominant approach is to construct and subsequently invert models that relate observations to interior properties. As observations have become increasingly sophisticated, the need for refined forward modeling has become apparent. One reason the forward approach is crucial is that although the resonant mechanical modes of the Sun (the diagnostic agents of helioseismology) have been studied carefully, there are still many curious wave properties neglected in models that may prove significant. For example, finite wavelength effects cast doubt on the validity of the ray approximation in some situations (e.g., Hung, Dahlen, & Nolet, 2001; Couvidat et al., 2004); magnetic fields in the case of sunspots are potentially non-trivial contributors to the wavefield. Although these implications have been known for a while now, a systematic means of investigating such factors has only recently been constructed. Such studies

† *This chapter are reproduced from Hanasoge, Duvall, & Couvidat (2007). I was the first author and principally involved in the work. I constructed the code and performed all the simulations. Tom Duvall, Jr. computed the kernels and supplied data for Figures 3.1, 3.5, 3.11, and 3.12. S. Couvidat generated the following Figures 3.3, 3.6, 3.7, and 3.8.*

are difficult to conduct by purely analytical means, requiring the introduction of numerical methods to solve the constituent governing equations of wave motion (e.g., Tong et al., 2003; Hanasoge et al., 2006; Shelyag, 2006; Parchevsky & Kosovichev, 2006).

The effects of sound-speed perturbations on acoustic waves have been investigated in the past (e.g., Jensen et al., 2003; Jensen & Pijpers, 2003; Birch, Kosovichev & Duvall, 2004). In fact, Jensen et al. (2003) constructed a forward model to compute the wavefield associated with a sunspot-type sound-speed profile containing a near-surface decrease in the sound speed and an increase in the deeper layers.

Sensitivity kernels are mathematical structures that relate shifts in observational metrics such as travel times, resonant frequencies, etc. to the anomalies that cause them. Birch & Kosovichev (2000) and Gizon & Birch (2002) introduced finite frequency sensitivity kernels for helioseismology (note: we will use the terms 'finite wavelength' and 'finite frequency' interchangeably in future discussions) that include wave effects in the Born limit, to invert for p-mode interior sound speed, f-mode damping and source perturbations. The computation of these kernels is a non-trivial affair. Moreover, these kernels are obtained in the single scattering limit and the Born approximation itself may not be applicable for problems such as inversions of sunspots (Birch, private communication). In this chapter, we measure kernels at the photospheric level from simulations in two cases for which the Born limit is valid and published kernels are available for comparison (Gizon & Birch, 2002; Birch, Kosovichev & Duvall, 2004).

We also introduce the idea of noise subtraction, based on which we can obtain large signal to noise ratio (SNR) improvement in our simulations. Applying this concept, for certain problems, with as little as 40 hours of computing time, the signal can be boosted by so much that the eventual SNR is at the same level as that of two years of solar data. In §2 we discuss the numerical procedure applied to compute the wavefield. The idea of noise subtraction is introduced in §3.3 along with results that demonstrate its effectiveness. Travel times for the simulated wavefield are estimated with the technique of surface focusing in §3.4. We show how noise subtraction affects the travel times and also validate the results from the simulations in this section. An alternative method to compute kernels for helioseismology is shown to be effective in §3.5. We summarize our results and draw conclusions in §3.6.

3.2 The Simulation

The acoustic wavefield is simulated by numerically solving the linearized 3D Euler equations in Cartesian geometry:

$$\partial_t \rho = -\boldsymbol{\nabla}\boldsymbol{\cdot}(\rho_0 \mathbf{v}) - \Gamma\rho, \tag{3.1}$$

$$\partial_t \mathbf{v} = -\frac{1}{\rho_0}\boldsymbol{\nabla} p - \frac{\rho}{\rho_0} g\hat{\boldsymbol{z}} + \mathbf{S} - \Gamma\mathbf{v}, \tag{3.2}$$

$$\partial_t p = \rho_0 g v_z - \rho_0 c^2 \boldsymbol{\nabla}\boldsymbol{\cdot}\mathbf{v} - \Gamma p, \tag{3.3}$$

where ρ and ρ_0 are the fluctuating and time-stationary background density respectively, p and p_0 are the fluctuating and time-stationary background pressure respectively, $\mathbf{v}$ is the fluctuating vector velocity, $g = g(z)$ is gravity with direction vector $-\hat{\boldsymbol{z}}$, $c = c(x, y, z)$ is the sound speed, $\Gamma = \Gamma(x, y, z) > 0$ is a damping sponge that enhances wave absorption at the boundaries, and $\mathbf{S}$ is the source term. We employ a Cartesian coordinate system (x, y, z) with $\hat{\boldsymbol{z}}$ denoting the unit vector along the vertical or z axis and t, time. In sequential order, equations (3.1) through (3.3) enforce mass, momentum, and energy conservation respectively. In interior regions of the computational box (away from the boundaries), solutions to the above equations are adiabatic since equation (3.3) is applicable only in the case of adiabatic oscillations (e.g., Hanasoge et al., 2006) and there are no other damping terms.

In our computations, waves are excited by a vertically directed dipolar source function, $\mathbf{S} = S(x, y, z, t)\ \hat{\boldsymbol{z}}$, similar to the function described in Hanasoge et al. (2006). The function $S(x, y, z, t)$ is highly localized along the z axis, described by a Gaussian with full width at half maximum (FWHM) of 200 km. Adopting the approach described in Hanasoge et al. (2006), we start our analysis in the frequency

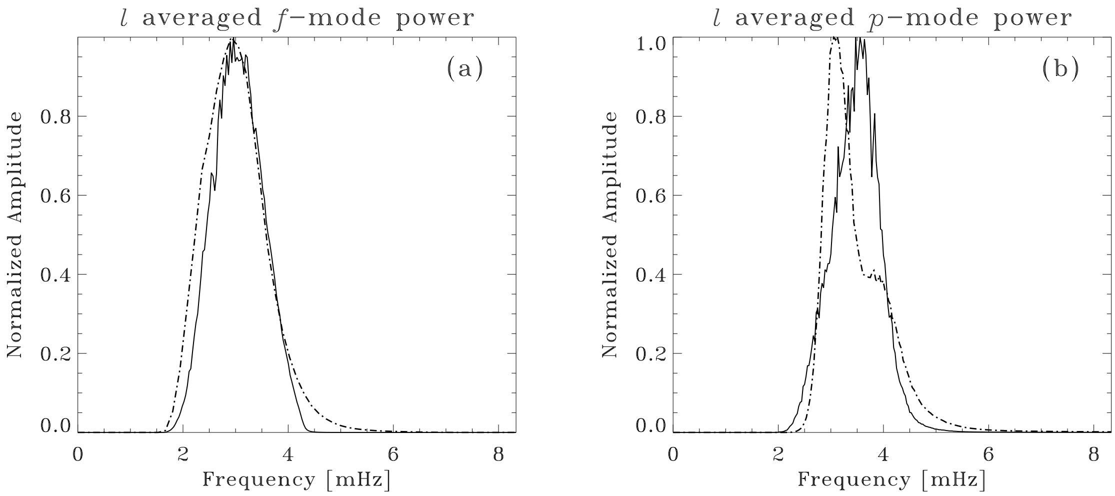

Figure 3.1 Comparison of wavenumber averaged power profiles of MDI high-resolution data (dot-dash line) and simulations (solid line) as a function of frequency. The f-mode power distribution in panel (a) is quite representative of the observations. Because of the lack of damping, the p-mode power distribution in panel (b) does not do quite so well. A phase-speed filter (Filter 'B' of Birch, Kosovichev & Duvall (2004)) was applied to obtain panel (b).

- horizontal wavenumber Fourier space. Because scattering processes are sensitive to the frequency and wavelengths of interacting waves, we attempt to mimic the solar acoustic power spectral distribution as closely as possible (see Figure 3.1). In the Sun, the competing effects of damping that has a super-linear frequency dependence and mode mass that decreases with frequency create a power maximum at $\nu = 3$mHz. However, one immediately realizes that solar damping rates are by no means simple functions of frequency with the consequence that fully including these dissipation rates in our time domain calculations is made all but impossible. Moreover, the aim of these calculations is to separate the influences of perturbative forces, one of which undoubtedly is damping (e.g., Gizon & Birch, 2002). Therefore, although approximate representations of the solar damping function could be incorporated into the equations above, we make the active choice to leave them out at present, with the full intention of pursuing a greater understanding of the effects of dissipation at a future occasion.

As for the dependence of the excitation function on horizontal wavenumbers, each coefficient in Fourier space is assigned a value from the output of a Gaussian distributed random number generator (the Ziggurat algorithm, available online from NETLIB). This results in uniform power across wavenumbers, which is somewhat different in the Sun because the sources are at granular scales and there is some dependence of power on wavenumber. To achieve the demands placed on the frequency dependence of the spectrum, we multiply these coefficients by an a priori specified frequency envelope. Lastly, we prescribe the excitation function so that it possesses no power beyond (to the right of) the f-mode ridge where modal power in the Sun is practically non-existent anyway.

Revisiting the background state, we use time-stationary properties p_0, ρ_0, g and c given by the convectively stable model of Hanasoge et al. (2006) based on model S (Christensen-Dalsgaard et al., 1996). Without additional artificial stabilization, simulations of wave activity in the near surface layers tend to blow up very rapidly due to exponentially growing linear convective instabilities. This stabilization results in a modified dispersion relation for p modes, not quite the same as it is for the Sun, but mercifully, close enough that existing methods of helioseismology may be applied with few alterations. The functional dependence of c presented in the model of Hanasoge et al. (2006) is entirely radial (vertical); for experiments with sound-speed perturbations, we alter c so that it becomes a 3D function of space while keeping p_0 and ρ_0 constant. The latter variables are kept constant so that the delicate hydrostatic balance remains undisturbed, which if tampered with, results in a Kelvin-Helmholtz instability. As seen in equation (3.4) this means that when we alter the sound speed and not the pressure or density, the first adiabatic index Γ_1 changes in the same sense, since

$$c = \sqrt{\frac{\Gamma_1 p_0}{\rho_0}}. \tag{3.4}$$

It can be shown that the degree of convective instability, characterized by the Brünt-Väisälä frequency N ($N^2 < 0$ means instability) in equation (3.5), increases when Γ_1 (or c) is reduced:

$$N^2 = g\left(\frac{1}{\Gamma_1}\frac{\partial \ln p_0}{\partial z} - \frac{\partial \ln \rho_0}{\partial z}\right). \tag{3.5}$$

Consequently, all our theoretical experiments are with local increases in sound speed. Our expectation is that decreases in sound speed affect helioseismic metrics in the opposite sense as corresponding increases would.

3.2.1 Numerical Algorithm

The computational domain is a cuboid that straddles the solar surface, extending from approximately 30 Mm below the photosphere to 2 Mm into the atmosphere. The vertical (radial) grid spacing is such that acoustic travel time between adjacent grid points is constant while the horizontal grid points are equally spaced. The damping sponge described in the previous section is placed adjacent to the six boundaries of the computational box. It is important that the function describing the damping layer decays sufficiently smoothly away from the boundary so that no wave reflections occur at the interface of the absorbent region. Absorbing boundary conditions (Thompson, 1990) are enforced at all boundaries. We choose absorbing over periodic boundaries because we want to avoid the issue of dealing with periodicities associated with the presence of a perturbation.

Derivatives are calculated using sixth-order compact finite differences (Lele, 1992). The solution is evolved in time using an optimized five-stage fourth-order Runge-Kutta scheme (Berland et al., 2006). To avoid aliasing, we apply the three-halves rule (Orszag, 1970), requiring that the number of grid points be at least three-halves the maximum captured wavenumber. In order to avoid vertical (radial) aliasing and the subsequent spectral blocking, we apply the de-aliasing procedure described in Hanasoge & Duvall (2007) every minute in solar time. We also de-alias variables in the horizontal directions by applying a smooth filter that diminishes the upper third of the spectrum and leaves the important lower two-thirds untouched (also at the rate of once per minute). All FFTs are performed using the freely distributed set of routines, the FFTW.

In order to achieve a comparable computation to wall clock time ratio, the code was parallelized according to the Message Passing Interface (MPI) Standard. The domain distribution algorithm is similar to the method described in Hanasoge &

Duvall (2006). The computational box is distributed along the y axis; all points on the x and z axes for a given point on the y axis are located in-processor. The data is transposed and redistributed between processors when the solution has to be filtered and when derivatives along the y axis need to be computed. It is probably true that greater parallel efficiencies may be achieved if the domain distribution is along all axes. However, incumbent to determining the optimal parallel configuration is the investment of considerable time, no doubt entailing many tedious hours of programming and debugging. At present, we only treat relatively small problems ($200 \times 200 \times 40$ Mm^3 is the biggest box) and achieve ratios of 1:1 (usually better) computing to real time. Seeing little merit in further code optimization, we have relegated such investigations to the future.

3.2.2 Power Spectrum

The modal distribution of power we recover upon putting together all the ideas discussed above and subsequently performing the computation is shown in Figure 3.2. We do not have a convincing explanation for the oddly shaped inter-ridge mode tails. Beyond the demarcation of the excitation profile, seen just below the f-mode ridge, excitation levels drop to zero. Also, in accordance with the three-halves rule, the excitation is Fourier limited, not extending beyond two-thirds of the spatial Nyquist wavenumber. The root mean squared (RMS) spatially averaged velocity as a function of time is shown in Figure 3.5; the simulation in this case is seen to achieve statistical stationarity in 4.5 hours. This timescale corresponds to at least a few bounces of the largest wavelength acoustic waves and presumably, full stationarity is reached when the balance between the forcing and the absorbent layers (at all boundaries) is struck.

3.3 Noise Subtraction

Given that we have full control over the excitation mechanism and source function, we can achieve high SNR in the artificial data by *subtracting* the noise out. In other words, having computed a source function, we perform two simulations, one with

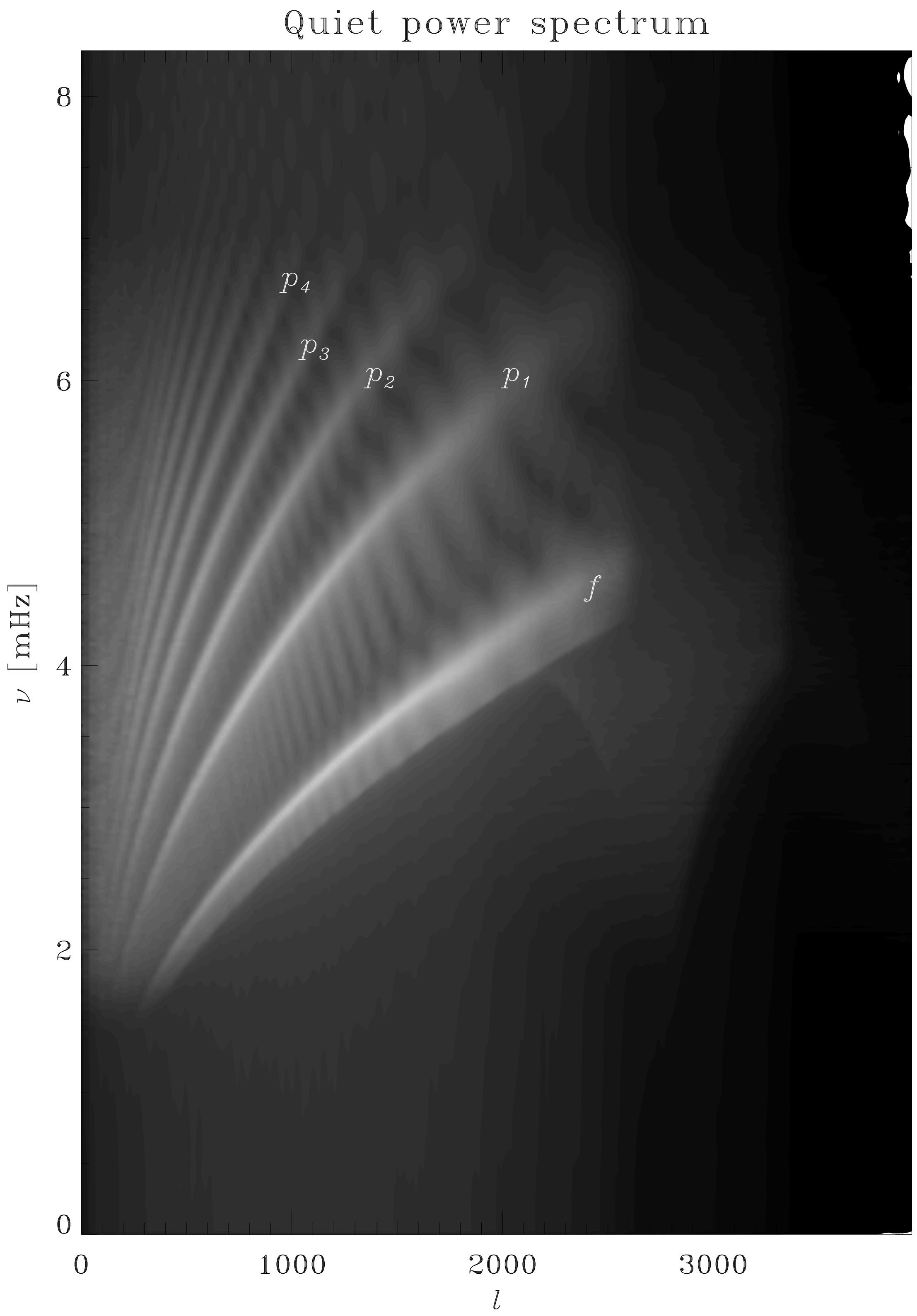

Figure 3.2 'Quiet' power spectrum obtained from a simulation in a $200 \times 200 \times 30$ Mm^3 box. The horizontal axis is spherical harmonic degree, l and the vertical axis is the frequency in milli-Hertz.

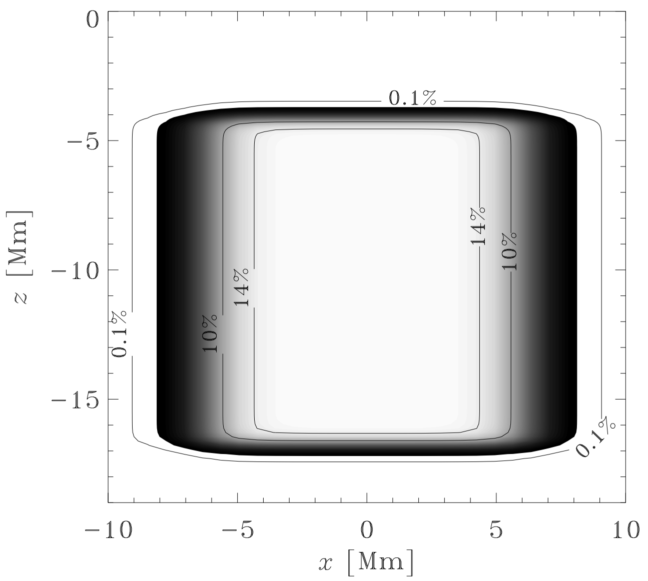

Figure 3.3 Vertical cut in the sound-speed perturbation discussed in Figure 3.4 and section 3.4.1. The labels on the isocontours show the amplitude of $\delta c^2/c^2$.

no perturbations ('quiet' simulation) and another with the perturbation of interest (shown in Figure 3.3). Evidence of the ability of this method is demonstrated by displaying the time-averaged RMS of the velocity differences between a quiet and perturbed model in Figure 3.4(b). Compare this to Figure 3.4(a) which is the time-averaged RMS velocity of the perturbed model. Subsequently, we can subtract the travel times of the quiet data from its perturbed cousin and depending on the size of the perturbation in comparison to the wavelength, excellent signal-to-noise properties can be achieved. The instantaneous difference is shown in panel (c) of Figure 3.4. In some cases where the perturbation is highly sub-wavelength in size, the SNR after noise subtraction is as much as 1000:1. In subsequent sections, we shall elaborate further upon the applications of this technique.

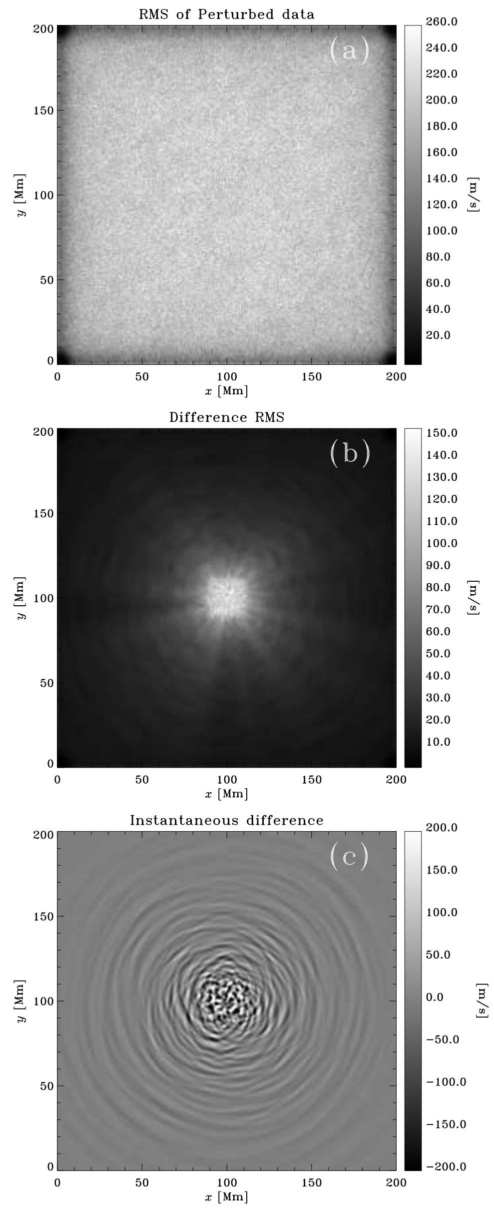

Figure 3.4 Panel (a): the time averaged RMS velocity of the wavefield interacting with a 12 Mm-sized sound-speed increase (shown in Figure 3.3), centered around $(x, y, z) = (100 \text{ Mm}, 100 \text{ Mm}, -10 \text{ Mm})$. The sound-speed anomaly is entirely invisible in panel (a). The darkening towards the spatial edges of the frame is due to the absorbent sponge at work. Panel (b): the time averaged RMS velocity difference of the perturbed datacube and its quiet counterpart. The difference between the quiet and perturbed datacubes is greatest at the location of the perturbation due to enhanced scattering. Panel (c): the instantaneous difference between the perturbed and related quiet data 100 (solar) minutes into the simulation. The anomaly is a scatterer, creating ripples in the wavefield just like a pebble dropped onto the surface of still water. Fine wave structure is visible at the location of perturbation.

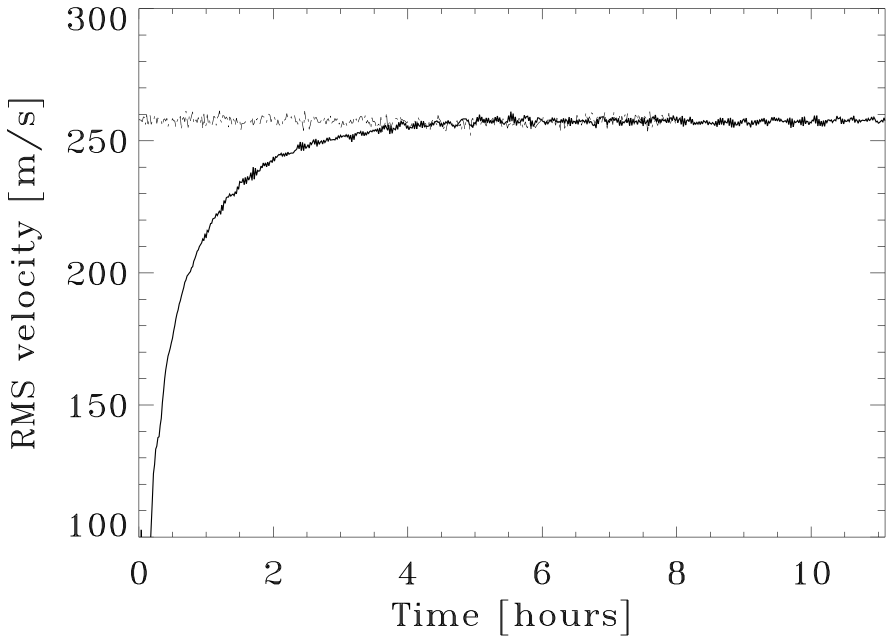

Figure 3.5 The spatial RMS velocity at the photosphere of a simulation (thick line) as compared to MDI high-resolution data (thin line) as a function of time. The system appears to achieve statistical stationarity 4.5 hours into the simulation. Because the system is linear, we can scale velocities by an arbitrary factor; in this case, velocities have been scaled so as to allow comparison with solar values.

3.4 Travel times with Surface Focusing

The time-distance helioseismic formalism introduced by Duvall et al. (1993) is based on the computation of cross-covariances between solar oscillation signals at two locations $\mathbf{r}_1$ and $\mathbf{r}_2$ on the solar surface ($z = 0$). Due to the stochastic excitation of acoustic waves (by convective motions in the Sun) and to the superposition of a large number of waves of different horizontal phase velocities $v_{ph} = \omega/k$, where k is the horizontal wavenumber and ω is the temporal angular frequency, the cross-covariances are very noisy and need to be phase-speed filtered and averaged (Duvall et al., 1997). The Doppler velocity datacube $\phi(\mathbf{r}, t)$ is phase-speed filtered in the Fourier domain using a Gaussian filter $F(k, \omega; \Delta)$ for each travel distance $\Delta = |\mathbf{r}_2 - \mathbf{r}_1|$:

$$F(k, \omega; \Delta) = \exp\left[-\frac{(\omega/k - v)^2}{2\delta v^2}\right], \tag{3.6}$$

where the central phase-speed v is derived from the solar model describing the oscillation power spectrum. For p modes in the ray approximation, v corresponds to ω/k at the lower turning point of a ray that traverses a horizontal distance Δ between successive reflections. The filter width δv is chosen empirically.

The standard method is then to average point-to-point cross-covariances over an annulus centered on $\mathbf{r_1}$ and with a radius Δ. Such point-to-annulus cross-covariances are computed for several distances Δ (55 in this chapter), and then averaged by groups of 5 distances to further increase their SNR. A detailed explanation of all the steps in the analysis process can be found in, e.g., Couvidat, Birch, & Kosovichev (2006). Table C.1 in appendix C.2 lists the distances Δ and phase-speed filter characteristics used here. These values are slightly different from the solar case because of the modified description of the background model.

The point-to-annulus cross-covariances are fitted by two Gabor wavelets (Kosovichev & Duvall, 1997): one each for the positive and negative times. To select the first-bounce ridge, we multiply the temporal cross-covariances by 14-minute wide rectangular window functions prior to the fit. The center t_0 of these windows is listed in Table C.1. The fitting procedure returns the ingoing (subscript i) and outgoing (subscript o) phase travel times $\tau_{\mathrm{i/o}}(\mathbf{r}, \Delta)$. The average of these two travel times, $\tau_{\mathrm{mean}}(\mathbf{r}, \Delta)$ is at first approximation sensitive only to the sound speed $c(\mathbf{r})$ in the region traversed by the wavepacket (see Eq. [3.7]), and similarly the difference $\tau_{\mathrm{diff}}(\mathbf{r}, \Delta)$ only to material flows. Note, by wavepacket, we mean a collection of waves of different frequencies and wavelengths that satisfy a specific dispersion relation, $\omega = \omega(k)$.

3.4.1 Results

We separately compute the acoustic wavefield in the presence of a sound-speed anomaly and the unperturbed counterpart with the same forcing function. Subsequently, we derive travel-time maps related to these datacubes by applying the method described

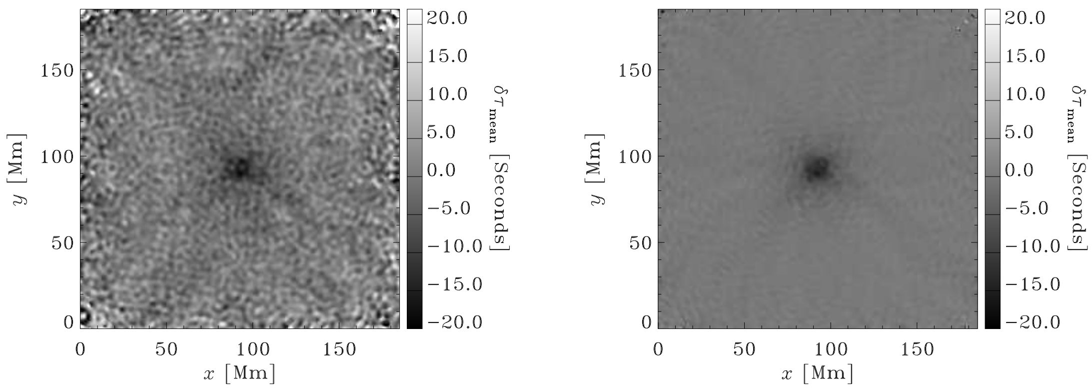

Figure 3.6 Example of mean travel-time perturbation map $\delta\tau_{\mathrm{mean}}(\mathbf{r}, \Delta)$ for $\Delta = 30.55$ Mm. Left panel: before quiet map subtraction. Right panel: after subtraction.

in §3.4. Here we shall focus on results related to a cylindrical sound-speed perturbation (see Figure 3.3) with a horizontal radius of about 6 Mm, a height of 12 Mm, centered at a depth of 10 Mm, and with a maximum amplitude of $\delta c^2/c^2 = 15\%$. The travel-time map corresponding to the distance $\Delta = 30.55$ Mm is shown on the left panel of Figure 3.6. On the right panel, the quiet travel-time map has been subtracted: the noise level is considerably reduced, as mentioned in §3.3. The travel-time map on the left panel looks very similar to maps computed for datacubes obtained from the Michelson Doppler Imager (MDI) instrument onboard the Solar and Heliospheric Observatory (SOHO) spacecraft, and because the noise levels between the artificial and real data are comparable, the choice of the excitation mechanism is somewhat justified. Figure 3.7 further shows the impact of the noise subtraction method on the travel-time maps.

In Figure 3.8, the dependence of the azimuthally averaged mean travel-time perturbations, $\delta\tau_{\mathrm{mean}}(\mathbf{r}, \Delta)$, on the radial distance from the center of the perturbation is shown by the thick solid line. The RMS variation σ of $\delta\tau_{\mathrm{mean}}(\mathbf{r}, \Delta)$ is an estimate of the uncertainty on this value (the error bars on Figure 3.8 are $\pm\sigma$). The thin solid line is the average of the difference travel-time perturbation $\delta\tau_{\mathrm{diff}}(\mathbf{r}, \Delta)$ and is close to zero, as expected from the absence of flows in our simulation.

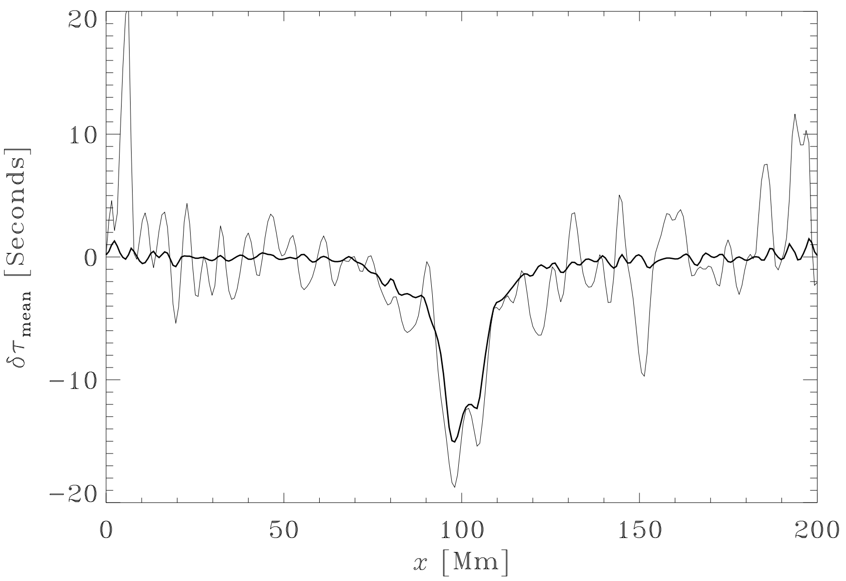

Figure 3.7 Cut across mean travel-time perturbation map $\delta\tau_{\mathrm{mean}}(\mathbf{r},\Delta)$ from Figure 3.6 at $y = 50$ Mm. Thin line: before quiet map subtraction, thick line: after subtraction.

3.4.2 Validation

A first test of the effectiveness of the numerical algorithm is to see if the simulated power spectrum looks reasonable in comparison to the solar modal spectrum. The spectrum shown in Figure 3.4(a) seems to satisfy this basic criterion. Secondly, through ray calculations, we can estimate the mean travel times associated with the background solar model. Although we do not show this here, comparisons between the ray predicted travel times and those obtained from the quiet simulations further fortify our confidence in the computational method. Next, using Born sensitivity kernels for sound-speed perturbations (Birch, Kosovichev & Duvall, 2004), we can derive the expected $\delta\tau_{\mathrm{mean}}(\mathbf{r},\Delta)$ (or $\delta\tau_{\mathrm{diff}}$) by evaluating the right-hand side of the following equation (forward problem):

$$\delta\tau_{\mathrm{mean/diff}}(\mathbf{r},\Delta) = \iint_S d\mathbf{r}' \int_{-d}^{0} dz\, K_{\mathrm{mean/diff}}(\mathbf{r}-\mathbf{r}', z;\Delta)\, \frac{\delta c^2}{c^2}(\mathbf{r}', z) \tag{3.7}$$

where S is the area of the Doppler velocity datacube, d is its depth, $K_{\mathrm{mean/diff}}(\mathbf{r} - \mathbf{r}', z; \Delta)$ are the sensitivity kernels for distance Δ, and $\delta\tau(\mathbf{r}; \Delta)$ is defined as the travel-time shift at the center of the annulus (whose radius is Δ). The kernels we use to calculate the right hand side of equation (3.7) were computed for the standard solar model S (Christensen-Dalsgaard et al., 1996), implying that the comparison is mostly qualitative, since we use a slightly altered description of the near-surface layers (Hanasoge et al., 2006). These are point-to-point kernels, azimuthally averaged the same way as the cross-covariances to produce point-to-annulus kernels. The ingoing and outgoing point-to-annulus kernels are then either averaged or subtracted in relation to $\delta\tau_{\mathrm{mean}}$ and $\delta\tau_{\mathrm{diff}}$.

In Figure 3.8, the dashed line shows the azimuthal average of $\delta\tau_{\mathrm{mean}}(\mathbf{r}, \Delta)$ obtained from equation (3.7) while the solid line is an azimuthal average of the mean travel-times obtained from the simulation. As expected, the two lines are not quite identical; this is perhaps due to small differences between phase-speed filter parameters and the background models in the two cases. Two independent methods were used in this comparison: the Born approximation to solve the forward problem, and the wavefield simulation in conjunction with a code to extract travel times from these calculations. Next, we check to see if the mean travel-time shifts computed with the ray approximation, shown as the dot-dash line in Figure 3.8, are comparable. As expected, ray theory, not accounting for wavefront healing (e.g., Hung, Dahlen, & Nolet, 2001), over-estimates these shifts but is still relatively accurate. It is gratifying to see that although the approaches in these methods differ greatly, there is still close agreement between the travel times. At this juncture, we consider the numerical method validated for the cases discussed here.

3.5 Kernels

Extending equation (3.7) to account for arbitrary perturbations, $\delta q(\mathbf{r}')$, we have:

$$\delta\tau_{\mathrm{mean/diff}}(\mathbf{r}; \Delta) = \int\int_S d\mathbf{r}' \int_{-d}^{0} dz K_{\mathrm{mean/diff}}(\mathbf{r} - \mathbf{r}', z; \Delta)\delta q(\mathbf{r}', z), \qquad (3.8)$$

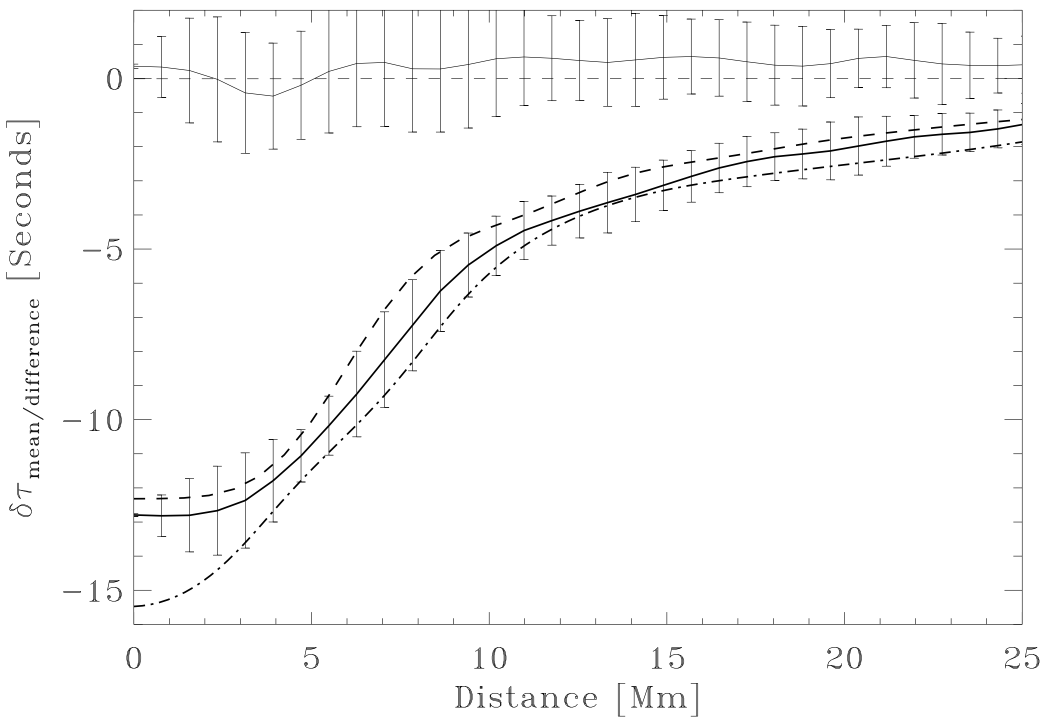

Figure 3.8 Azimuthal average of $\delta\tau_{\mathrm{mean}}(\mathbf{r}, \Delta)$ (thick solid line) and $\delta\tau_{\mathrm{diff}}(\mathbf{r}, \Delta)$ (thin solid line) for $\Delta = 30.55$ Mm, as a function of the radial distance to the sound-speed perturbation center (simulation). The dot-dash line is the mean travel-time shift computed with ray kernels for the background model in the simulation. The dashed lines are the solution to the forward problem using Born sensitivity kernels. The solar model in the simulation is slightly different from the model used to compute the Born kernels, contributing to the difference between the two travel-time curves.

where for future discussions, we adopt the notation of Duvall, Gizon & Birch (2006), namely that $\delta\tau(\mathbf{r};\Delta)$ is defined as the travel-time shift at position $\mathbf{r}$, located at the center of two observation points spaced distance Δ apart. With this change in definition of travel-times, we move from the center-to-annulus geometry of the previous section to a point-to-point description. There are numerous kinds of anomalies (changes in density, sound speed, pressure, source amplitude, magnetic fields to name a few) each of which is associated with a specific kernel. For perturbations that are spatial delta functions with magnitude M, of the form $\delta q(\mathbf{r}', z) = M\delta(\mathbf{r}')\delta(z - z_0)$, it may be verified from equation (3.8) that the convolution on the right hand side reduces to $(2\pi)^3 MK(\mathbf{r}, z_0; \Delta)$ (the 2π factors are dependent on the definition of the δ function), the conclusion being that the travel-time shifts and the kernel are identical to within a proportionality constant in this limit. Duvall, Gizon & Birch (2006) incorporated this approximation to derive a kernel from observations of thousands of thin magnetic elements on the Sun, justifying it through the argument that the magnetic flux tubes were all much smaller than the wavelength of the f modes used in the analysis. We apply the same technique to derive (1) a p-mode sound-speed kernel and (2) an f-mode source kernel from a thousand randomly placed small (1 Mm in size) source suppressions (see Figure 3.9) for the solar model and setup in our computations.

We choose this set of kernels to study because Gizon & Birch (2002) and Birch, Kosovichev & Duvall (2004) have constructed f-mode source disturbance and p-mode sound-speed perturbation kernels respectively, allowing us the luxury of comparison. In the source perturbation kernel of Gizon & Birch (2002), elliptical features are absent and only hyperbolic features associated with multiple sources are seen; the sound-speed kernels of Birch, Kosovichev & Duvall (2004) contain a mixture of both elliptical and hyperbolic ridges. The ability to recover a source kernel from the simulation of Figure 3.9 is important because we demonstrate proof of concept of the kernel measurement method devised by Duvall, Gizon & Birch (2006). The balance between the randomness of the locations of these elements and the determinism of the sense of the perturbation (all sources are reduced) seems to result in an average structure in the travel times that looks remarkably like the source perturbation kernel from Gizon & Birch (2002), as seen in panels (a) through (d) of Figure 3.5.

The technique through which the SNR of data is improved by enough that it becomes possible to see the travel times associated with these small features is described in detail by Duvall, Gizon & Birch (2006). Firstly, the data is phase-speed filtered to either restrict the acoustic spectrum to waves that travel a given distance, Δ, between bounces or to isolate the f-mode ridge. For all points $\mathbf{r} = (x, y)$ in the domain of interest (Eq. [3.8]), the temporal cross-correlation is obtained by inverse Fourier transforming $\tilde{C}$, where

$$\tilde{C}(\omega, x + \delta x/2, y + \delta y/2) = \tilde{v}^*(\omega, x, y)\tilde{v}(\omega, x + \delta x, y + \delta y), \tag{3.9}$$

which is subsequently fitted to obtain travel times. In equation (3.9), ω is the frequency, $v(t, x, y)$ is the velocity signal at time t and spatial location (x, y), with $\tilde{v}(\omega, x, y)$ representing the Fourier transform of $v(t, x, y)$, $\tilde{v}^*$ the complex conjugate of $\tilde{v}$, and $\arctan(\delta\mathrm{y}/\delta\mathrm{x})$ the orientation of the travel-time map. Within the limits of spatial resolution, there were 77 possible orientations for the simulation that contained the sound-speed perturbation (120×120 Mm^2 in the (x, y) plane, resolved with 144^2 points) and 83 orientations for the source perturbation case (200×200 Mm^2 in the (x, y) plane, resolved with 512^2 points). Subsequently, the resulting two-point travel times were de-rotated by an angle $\arctan(\delta\mathrm{y}/\delta\mathrm{x})$ and averaged. For the simulation with the 1000 suppressions, the image is not only de-rotated but averaged around each feature, corresponding to a net total of 83,000 averages. The SNR is still not high enough with this degree of averaging; only after the travel times of the quiet datacube, obtained through the same averaging process, are subtracted, do the hyperbolae of the kernel become clearly visible. A similar averaging algorithm is used to produce the sound-speed kernel (Figure 3.12), albeit the wavefield was simulated in the presence of only one anomaly.

3.5.1 Source Kernels

Although the magnitudes and the hyperbolic features are somewhat different, kernels obtained from simulation and theory (Figure 3.5), possess a strong resemblance. It is

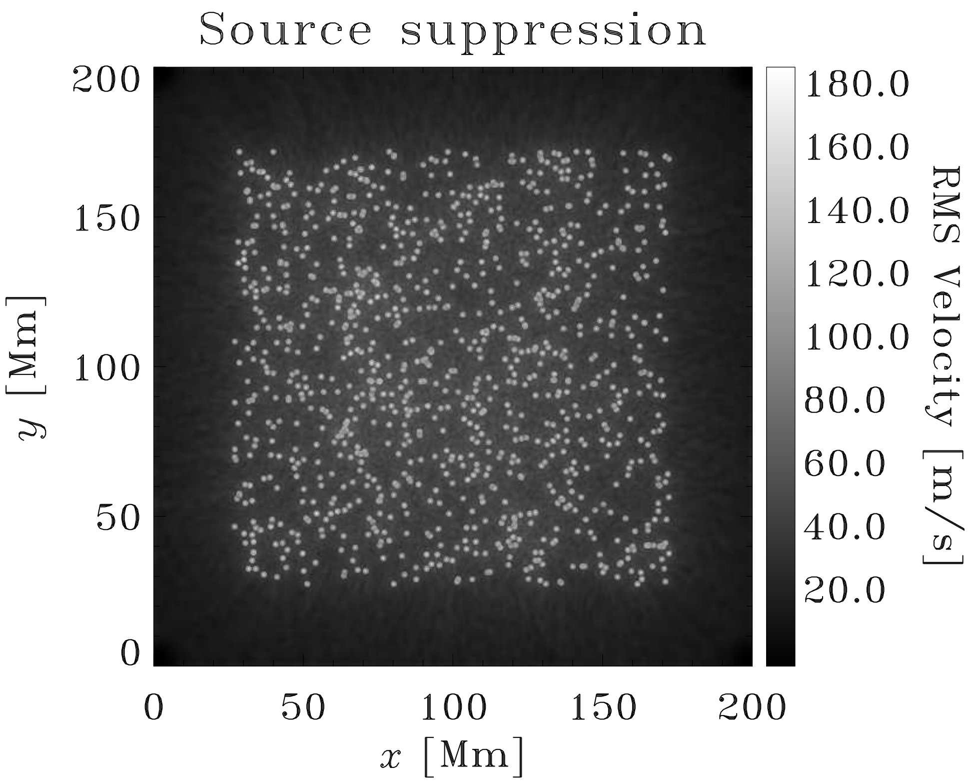

Figure 3.9 The time averaged RMS of the difference in velocities from a simulation with one thousand randomly located 1 Mm-sized source suppressions and its unperturbed counterpart. In the vicinity of a source suppression, acoustic velocities are altered; therefore, the hundreds of local maxima in this difference map show where the sources are diminished. The perturbations are approximately limited to a 150×150 Mm^2 interior square, allowing for travel-time shifts associated with all the anomalies to be computed.

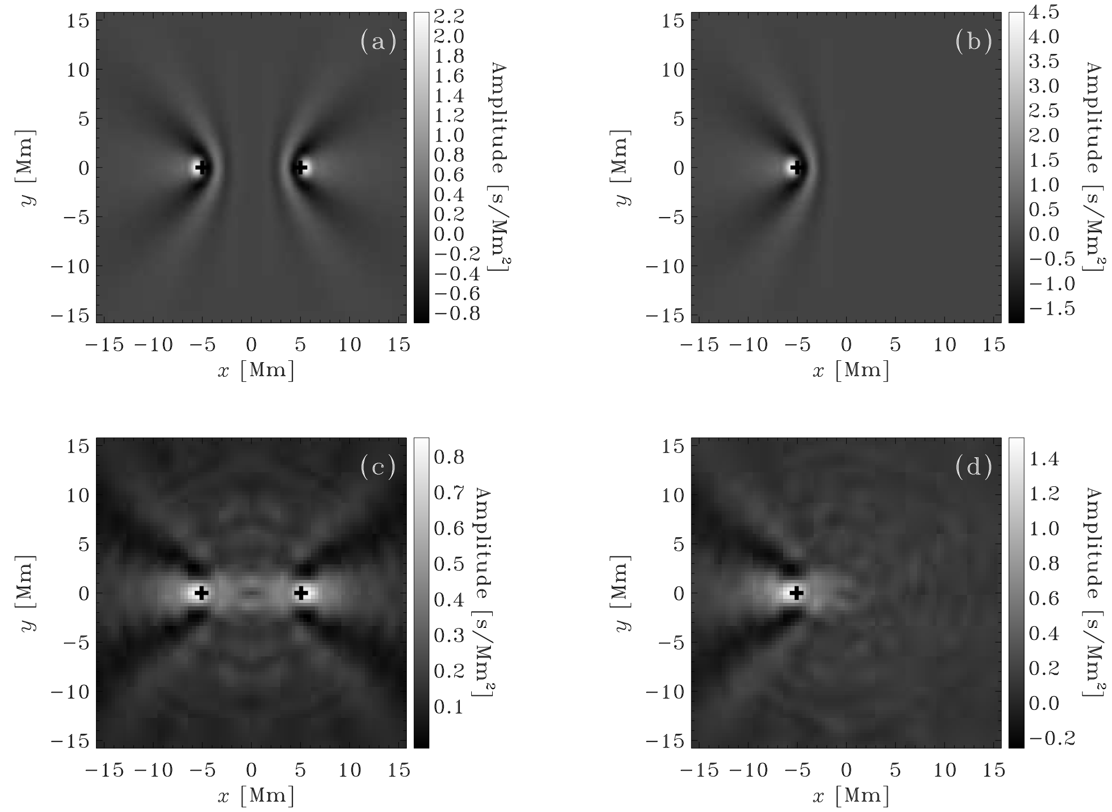

Figure 3.10 Source perturbations kernels for the *f*-mode. The panels (a) and (b) show the mean and left to right one-way kernels from Gizon & Birch (2002) respectively. Crosses show the measurement points. Upon systematically de-rotating and averaging the travel-time shifts associated with the thousand locally deactivated sources from Figure 3.9, subtracting the noise and scaling the travel times as described in appendix C.1, the kernels in panels (c) and (d) emerge. The lack of elliptical features in these kernels is perhaps explained by the independence of the sources from the wavefield, in the theory of Gizon & Birch (2002) and in the simulations. Panel (d) is especially compelling because according to theory, left to right one-way travel-times should only be shifted for those points which lie closer to the left measurement point. The power profile of the f-ridge used to recover the travel-time shifts is shown in Figure 3.1.

seen from Figure 3.1 that the f-mode power distribution is able to match the observations (and the excitation model of Gizon & Birch (2002)) quite well, so frequency effects are not significant contributors to the differences in the hyperbolic structures. One possible explanation could be the damping, included in theory but not in the simulations. The absence of solar-like damping has two important effects: (1) mode power distribution and line-widths differ from the solar counterparts and (2) waves are correlated across larger distances. The latter implies that travel-time shifts of waves remain coherent over longer length scales than in the Sun or the model of e.g., Gizon & Birch (2002). The other issue concerns the differing magnitudes of the kernels; perhaps the method described in appendix C.1 to scale the travel times is only approximate. Moreover, the theoretical kernel of Gizon & Birch (2002) has a spatial integral of zero, while the kernel obtained from the simulation has a positive bias of 0.5 seconds (calculated as the mean travel-time shift of a small off-center region).

The travel-time shifts observed in this case are due to reductions in the cross correlation amplitude because of local depressions in source strengths. The cross correlations are biased in the sense of decreased amplitude because all the sources have been suppressed, possibly leading to a non-zero value of the integral of the kernel. In an attempt to correct for this, we tried another case where approximately half the perturbed sources were suppressed and the other half amplified. To obtain a meaningful average kernel (shown in Figure 3.11), the sign of the travel times for the source suppressions was flipped while the source amplification counterparts were left untouched. In this case, the integral of the kernel is much smaller than the amplitude, indicating that the bias in the kernel of Figure 3.5(c) is most probably caused by the systematic sense in the perturbation (suppression).

3.5.2 Sound-Speed Kernels

The sound-speed kernel of Figure 3.12(a) was derived for the same measurement distance (12.4 Mm) as the one in Figure 3.12(b) (reproduced from the lower right panel of Figure 10 from Birch, Kosovichev & Duvall (2004)). Although there are many differences in the approaches, not the least being the background model and

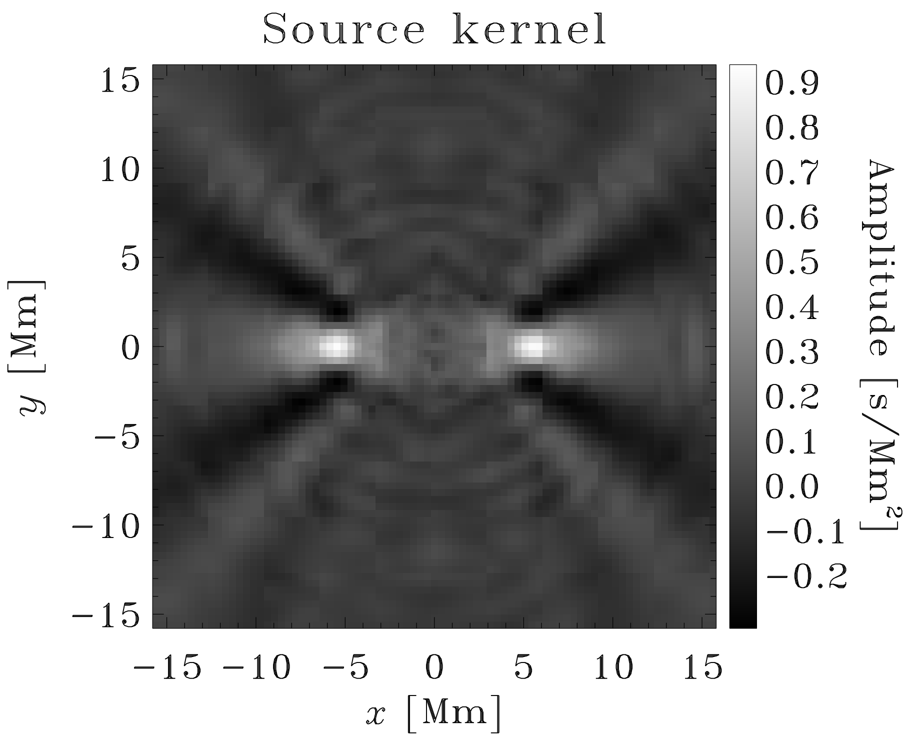

Figure 3.11 The source kernel obtained by the suppressing approximately half the sources and doubling the strengths of the rest. The integral of the kernel is an order of magnitude smaller than the amplitude of the kernel.

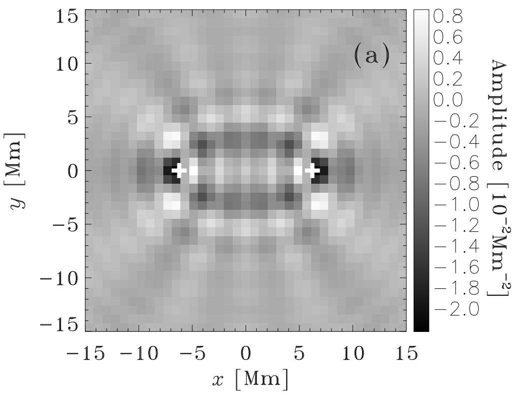

Figure 3.12 Panel (a): sound-speed kernel from 24 hours of simulated data (12 perturbed + 12 quiet). Panel (b): sound-speed kernel reproduced from the lower-right panel of Figure (10) of Birch, Kosovichev & Duvall (2004). The crosses mark the measurement points. The kernels have been multiplied by the sound speed at the photospheric level in both cases; units are in $10^{-2}\mathrm{Mm}^{-2}$. The agreement is striking. The circular features in panel (a) are generated by the repeated de-rotation of travel-time shifts and hence are mainly noise. Both hyperbolic and elliptic features are visible in this kernel. The power profile of the modes utilized to construct the kernel in panel (a) is shown in Figure 3.1(b).

damping rates, the agreement is excellent. This result also illustrates the ability of the method of noise subtraction to remove the noise without affecting the signal itself. Although not shown here, we have noticed that as the central frequency of the wavepacket used to construct the kernel increases, the ellipses become even more ‘elliptical’, an indicator of ray-like behavior. In general, there is a definite dependence of the shape of the kernel on the filter parameters.

3.6 Conclusions

A numerical method to compute the 3D wavefield in a solar-like medium was discussed and implemented. The concept of noise subtraction, a technique whereby the realization noise can be significantly reduced was introduced. This method is quite useful in reducing computational cost by making it possible to achieve large SNR even with short simulations. Results from the simulations were validated using comparisons between the travel times obtained (1) from the surface focusing method of time-distance helioseismology, (2) through the application of approximate Born sensitivity kernels, and (3) ray theory. The results agree rather well, showing the validity of these independent approaches for this particular situation.

We ran a simulation with a thousand randomly located suppressed sources which subsequently was analyzed by the feature method of Duvall, Gizon & Birch (2006) to obtain travel-time shifts associated with the average diminished source. The result closely resembles the source perturbation kernel of Gizon & Birch (2002). A sound-speed kernel for parameters similar to a case considered by Birch, Kosovichev & Duvall (2004) was derived. The agreement between Born theory and simulations in conjunction with time-distance helioseismology is impressive. It lends greater confidence in the technique of direct measurements of kernels from data (Duvall, Gizon & Birch, 2006) and the method of noise subtraction. It is interesting to note that the structure of the kernels is quite sensitive to the relevant frequency bandpass; high-frequency wave kernels have pronounced elliptic features displaying ray-like behavior. The source and sound-speed kernels shown here contain aspects of multiple scattering and in general, are not bound by the assumptions of the Born approximation. We can also derive sensitivity kernels for various types of perturbations like anomalies in density, pressure, Γ_1 etc., that are relatively difficult to compute in the Born limit.

The price we currently pay for the ability to perform these simulations is reduced realism. Damping, not accounted for in our computations, is an important contributor, affecting travel times (e.g., Woodard, 1997) and in general changing the distribution of modal power and the linewidths. A further approximation in our simulations is the use of an altered background state; the standard solar model S makes it difficult to perform linear simulations due to the inherent convective instability of the near-surface layers. It is important for sophisticated forward models to be able to incorporate damping and an accurate solar model.

The effects of diffractive or wavefront healing, a hotly contested phenomenon in geophysics, are currently being investigated in the context of helioseismology through these simulations. We will be able to place bounds on detectability, the accuracy of inversions and study vector effects like flows. It will also be very exciting to disentangle magnetic field effects and determine if we have a reasonable understanding of the interior structure of sunspots.

Chapter 4

The Born approximation for magnetic fields

4.1 Introduction‡

Time-distance helioseismology (Duvall et al., 1993) has been used to measure wave travel times in and around magnetic active regions and sunspots to estimate subsurface flows and wave-speed perturbations (e.g. Duvall et al., 1996; Kosovichev et al., 2000). A challenging problem is to estimate the subsurface magnetic field from travel times. In order to do so, one must understand the dependence of the travel times on the magnetic field.

As discussed by e.g. Cally (2005) the interaction of acoustic waves with sunspot magnetic fields is strong in the near surface layers. As a result, the effect of the magnetic field on the travel times is not expected to be small near the surface. Deeper inside the Sun, however, the ratio of the magnetic pressure to the gas pressure becomes small, and it is tempting to treat the effects of the magnetic field on the waves using perturbation theory. The hope is to eventually develop a linear inversion to estimate the subsurface magnetic field from travel times measured between surface locations

‡ *The results of this chapter are reproduced from Gizon, Hanasoge, & Birch (2006). I wrote a part of the paper and did much of the analysis presented here. The graphs were produced L. Gizon and A. C. Birch.*

that are free of magnetic field. Of particular interest is the search for a magnetic field at the bottom of the convection zone. Such a linear inversion scheme has been proposed by Kosovichev & Duvall (1997) for time-distance helioseismology using the ray approximation, but it needs to be extended to finite wavelengths.

As a first step, in this chapter, we consider the scattering of small amplitude acoustic plane waves by a magnetic cylinder embedded in a uniform medium. This simple problem has a known exact solution for arbitrary magnetic field strengths (Wilson, 1980). The first-order Born and Rytov approximations have proved useful in the context of time-distance helioseismology to model the effects of small local perturbations in sound speed and flows (e.g. Birch et al., 2001; Jensen & Pijpers, 2003; Birch & Felder, 2004). Here we use the Born approximation to compute the scattering of a wave by a weak magnetic field. The validity of the Born approximation is not a priori obvious in this case, since the magnetic field allows additional wave modes. Because we have an exact solution, however, we can study the validity of the linearization of travel times on the square of the magnetic field. We note that the problem of the scattering of waves by a non-magnetic cylinder with a sound speed that differs from the surrounding medium was investigated by Fan et al. (1995).

The outline of the chapter is as follows. In Section 4.2 we specify the problem and write the equations of motion for small amplitude waves. In Section 4.3 we review the exact solution to the scattering problem. In Section 4.4 we apply the first Born approximation to obtain the complex scattering amplitudes. In Section 4.5 we show that the Born approximation is an asymptote of the exact solution in the limit of infinitesimal magnetic field strength. In Section 4.6 we compare travel times computed exactly, in the Born approximation, and in the ray approximation. In Section 4.7 we provide a brief summary of our results and also discuss the limit when the magnetic tube radius tends to zero.

4.2 The Problem

4.2.1 Governing equations

We start with the ideal equations of magnetohydrodynamics. The equations of continuity, momentum, magnetic induction, and Gauss' law for the magnetic field are:

$$
\begin{aligned}
D_t\rho + \rho\boldsymbol{\nabla}\cdot\boldsymbol{v} &= 0, && (4.1)\\
\rho D_t\boldsymbol{v} + \boldsymbol{\nabla}p - \frac{1}{4\pi}(\boldsymbol{\nabla}\times\boldsymbol{B})\times\boldsymbol{B} &= 0, && (4.2)\\
\partial_t\boldsymbol{B} - \boldsymbol{\nabla}\times(\boldsymbol{v}\times\boldsymbol{B}) &= 0, && (4.3)\\
\boldsymbol{\nabla}\cdot\boldsymbol{B} &= 0, && (4.4)
\end{aligned}
$$

where $D_t = \partial_t + \boldsymbol{v}\cdot\boldsymbol{\nabla}$ is the material derivative, ρ the density, $\boldsymbol{v}$ the velocity, p the pressure, and $\boldsymbol{B}$ the magnetic field. For the sake of simplicity, we use the simple energy equation

$$\rho C_v D_t T + p\boldsymbol{\nabla}\cdot\boldsymbol{v} = 0, \tag{4.5}$$

where T is the temperature, $C_v = R/(\gamma - 1)$ the uniform specific heat at constant volume, R the gas constant, and γ the ratio of specific heats. This equation neglects all forms of heat losses. In addition we use the ideal gas equation of state

$$p = \rho R T. \tag{4.6}$$

4.2.2 Steady background state

We consider a magnetic cylinder with radius R and uniform magnetic field strength B_t embedded in an infinite, otherwise uniform, gravity free medium with constant density ρ_0, gas pressure p_0, and temperature T_0. We use a cylindrical coordinate system (r, θ, z) where r is the radial coordinate, θ is the azimuthal angle, and z is the vertical coordinate in the direction of the cylinder axis. We denote the corresponding unit vectors by $\hat{\mathbf{r}}$, $\hat{\boldsymbol{\theta}}$, and $\hat{\boldsymbol{z}}$. All steady physical quantities are denoted with an overbar. In particular, we have

$$
\begin{aligned}
\overline{\boldsymbol{B}} &= B_t\Theta(R-r)\hat{\boldsymbol{z}}, && (4.7)\\
\overline{\rho} &= \rho_t\Theta(R-r)+\rho_0\Theta(r-R), && (4.8)\\
\overline{p} &= p_t\Theta(R-r)+p_0\Theta(r-R), && (4.9)
\end{aligned}
$$

where the Heaviside step function is defined by $\Theta(r) = 0$ if $r < 0$ and $\Theta(r) = 1$ if $r > 0$. The density and pressure inside the tube are ρ_t and p_t respectively. We assume that there is no mean flow in this problem, i.e. $\overline{\boldsymbol{v}} = 0$.

We choose to study the case where the background temperature is the same inside and outside the magnetized region, i.e. $\overline{T} = T_t = T_0$. As a result, the sound speed, $c = (\gamma R\overline{T})^{1/2}$, is constant everywhere. This choice is motivated by our desire to restrict ourselves, as much as possible, to the study of the effect of the Lorentz force on waves, rather than the effect of a sound speed variation. Pressure balance across the magnetic tube boundary implies

$$p_t + B_t^2/8\pi = p_0, \qquad (4.10)$$

where p_t is the background gas pressure inside the tube. The density inside the tube is given by $\rho_t = \rho_0 p_t/p_0$, as the temperature is the same inside and outside the tube.

4.2.3 Linear waves

We want to study the propagation of linear waves on the steady background state defined above. Toward this end, we expand each physical quantity that appears in equations (4.1)-(4.6) into a time-varying component, denoted by a prime, and the steady component, denoted with an overbar. For example, we write $p = \overline{p} + p'$. After subtraction of the steady state, we obtain:

$$
\begin{aligned}
\partial_t\rho' &= -\boldsymbol{\nabla}\cdot(\overline{\rho}\boldsymbol{v}'), && (4.11)\\
\overline{\rho}\partial_t\boldsymbol{v}' + \boldsymbol{\nabla}p' &= \frac{1}{4\pi}\left[(\boldsymbol{\nabla}\times\boldsymbol{B}')\times\overline{\boldsymbol{B}} + (\boldsymbol{\nabla}\times\overline{\boldsymbol{B}})\times\boldsymbol{B}'\right], && (4.12)\\
\partial_t\boldsymbol{B}' &= \boldsymbol{\nabla}\times\left(\boldsymbol{v}'\times\overline{\boldsymbol{B}}\right), && (4.13)
\end{aligned}
$$

$$\nabla \cdot \boldsymbol{B}' = 0. \tag{4.14}$$

The linearized energy equation, in combination with equation (4.11) and the linearized equation of state, may be simplified to

$$\partial_t p' - c^2 \partial_t \rho' = \frac{\gamma - 1}{\gamma} c^2 \boldsymbol{v}' \cdot \nabla \overline{p}, \tag{4.15}$$

which describes adiabatic wave motion.

As we study linear waves on a steady background, we can consider one temporal Fourier mode at a time. The magnetic field $\overline{\boldsymbol{B}}$ and all other background quantities do not depend on z. Thus, a wave with a z dependence of the form $e^{ik_z z}$ will have the same z dependence after interacting with the magnetic cylinder. As a result, we study solutions where the pressure fluctuations are of the form

$$p'(\mathbf{r}, z, t) = \tilde{p}(\mathbf{r}) \exp(ik_z z - i\omega t), \tag{4.16}$$

where $\mathbf{r} = (r, \theta)$ is a position vector perpendicular to the tube axis. All the other wave variables, ρ', $\boldsymbol{v}'$, and $\boldsymbol{B}'$ are written in the same form as equation (4.16). Quantities with a tilde only depend on $\mathbf{r}$.

4.3 Exact Solution

For the sake of completeness, we briefly review an exact solution obtained by Wilson (1980) to equations (4.11)-(4.15). We consider a plane wave incident on the magnetic tube, with pressure fluctuations of the form

$$\tilde{p}_{\text{inc}}(\mathbf{r}) = P \exp(i\boldsymbol{k} \cdot \mathbf{r}), \tag{4.17}$$

where P is an amplitude and $\boldsymbol{k}$ is the component of the wave vector perpendicular to the tube axis. In order for the incident wave to be a solution to the non-magnetic problem, the horizontal wavenumber $k = \|\boldsymbol{k}\|$ must satisfy

$$k(\omega) = \sqrt{\omega^2/c^2 - k_z^2}\,. \tag{4.18}$$

In the rest of this chapter, unless otherwise stated, we will use k to denote $k(\omega)$. In cylindrical coordinates, this plane wave can be expanded as a sum over azimuthal components (index m) according to (e.g. Bogdan, 1989):

$$\tilde{p}_{\rm inc}(\mathbf{r}) = P \sum_{m=-\infty}^{\infty} i^m J_m(kr) e^{im\phi}, \tag{4.19}$$

where J_m denotes the Bessel function of order m and ϕ is the angle between $\boldsymbol{k}$ and $\mathbf{r}$.

The total wave pressure, hydrodynamic plus magnetic, and the radial velocity must be continuous across the tube boundary. Applying these boundary conditions, Wilson (1980) showed that the total pressure wave field is

$$\tilde{p}(\mathbf{r}) = \begin{cases} P \sum_m i^m B_m J_m(k_t r) e^{im\phi} & r < R \\ \tilde{p}_{\rm inc} + P \sum_m i^m A_m H_m(kr) e^{im\phi} & r > R \end{cases} \tag{4.20}$$

where $H_m = H_m^{(1)}$ is the Hankel function of the first kind of order m. The quantity k_t is the horizontal wavenumber inside the tube, given by

$$k_t = k \left[\frac{(\omega^2 - k_z^2 a^2)}{(1 + a^2/c^2)(\omega^2 - s^2 k_z^2)} \right]^{1/2}, \tag{4.21}$$

where $a = B_t/\sqrt{4\pi\rho_t}$ is the Alfvèn wave speed and $s = ac\,(a^2 + c^2)^{-1/2}$ is the tube velocity. The coefficients A_m and B_m are given in Appendix D.1. This exact solution is valid for arbitrarily large values of B_t and R. We note that the gas pressure fluctuations are discontinuous at the tube boundary.

Not all azimuthal components m contribute at the same level. Figure 4.1 shows the amplitudes of the A_m as a function of m for two different values of the tube radius, R. In this particular example, $\rho_0 = 5 \times 10^{-7}$ cgs, $c = 11$ km/s, and $B = 1$ kG are fixed. For $R = 0.5$ Mm, which is less than the wavelength ($kR = 0.86$), only the

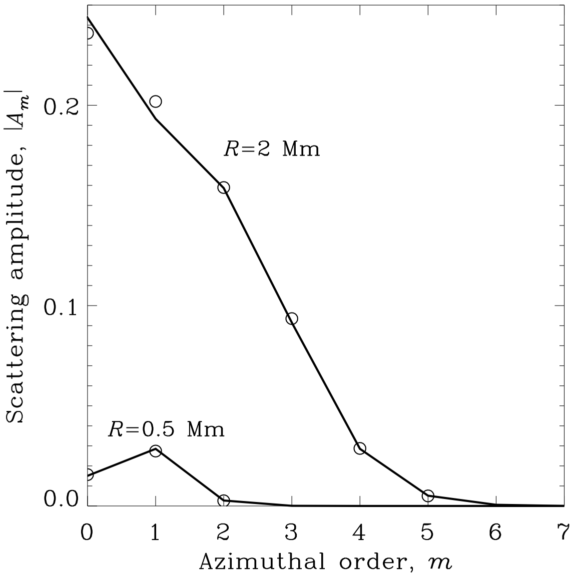

Figure 4.1 Coefficients $|A_m|$ as a function of m for $R = 2$ Mm and $R = 0.5$ Mm (thick lines). Only the $m > 0$ values are shown since $|A_{-m}| = |A_m|$. The magnetic field is $B = 1$ kG, $\omega/2\pi = 3$ mHz, and $k_z = 0$. The coefficients A_m are negligible for $m > 5$ in the case $R = 2$ Mm and for $m > 2$ in the case $R = 0.5$ Mm. The open circles are the Born approximation to these coefficients ($|A_m^{\rm Born}|$, see section 4.4).

$m = 0, \pm 1$ azimuthal components contribute. For tubes with larger radii the higher order components have larger amplitudes, as can be seen in the case $R = 2$ Mm ($kR = 3.43$).

4.4 First Born approximation

Magnetic effects cause perturbations to both the steady background state and the wavefield. In this section we use the Born approximation to derive an approximate solution to equations (4.11)-(4.15) based on the assumption that magnetic effects are small (see e.g. Rosenthal, 1995). The Lorentz force is quadratic in the magnetic field. As a result we introduce a small parameter that is second order in the magnetic field.

We choose to expand all quantities in powers of the small dimensionless parameter

$$\epsilon = \frac{B_t^2}{4\pi\rho_0 c^2}\,. \tag{4.22}$$

In this expansion framework the magnetic field appears at order $\epsilon^{1/2}$. In particular, we write the steady background magnetic field as

$$\overline{\boldsymbol{B}} = \epsilon^{1/2}\boldsymbol{B}_1. \tag{4.23}$$

The magnetic field causes a shift, $\epsilon\rho_1$, in the steady component of the density inside the tube relative to the steady component of the density outside the tube, ρ_0:

$$\overline{\rho} = \rho_0 + \epsilon\rho_1. \tag{4.24}$$

Likewise, we write the steady component of pressure as

$$\overline{p} = p_0 + \epsilon p_1. \tag{4.25}$$

These changes are related to the magnetic field through equation (4.10) and the equation of state:

$$p_1 = -\frac{\rho_0 c^2}{2}\Theta(R-r), \tag{4.26}$$

$$\rho_1 = -\frac{\gamma\rho_0}{2}\Theta(R-r). \tag{4.27}$$

We expand each of the wave-field variables into an incident component (subscript "inc") and a scattered component (subscript "sc"):

$$p' = p'_{\rm inc} + \epsilon p'_{\rm sc}, \tag{4.28}$$

$$\rho' = \rho'_{\rm inc} + \epsilon\rho'_{\rm sc}, \tag{4.29}$$

$$\boldsymbol{v}' = \boldsymbol{v}'_{\rm inc} + \epsilon\boldsymbol{v}'_{\rm sc}, \tag{4.30}$$

$$\boldsymbol{B}' = \epsilon^{1/2}\boldsymbol{B}'_{\rm sc}. \tag{4.31}$$

By inserting the above expansions into equations (4.11)-(4.15) and retaining the terms of order ϵ we obtain

$$\begin{aligned}
-i\omega\rho'_{\rm sc} + \rho_0 \boldsymbol{\nabla}\cdot\boldsymbol{v}'_{\rm sc} &= -\boldsymbol{\nabla}\cdot(\rho_1\boldsymbol{v}'_{\rm inc}), && (4.32)\\
-i\omega\rho_0\boldsymbol{v}'_{\rm sc} + \boldsymbol{\nabla}p'_{\rm sc} &= i\omega\rho_1\boldsymbol{v}'_{\rm inc} + \frac{1}{4\pi}(\boldsymbol{\nabla}\times\boldsymbol{B}_1)\times\boldsymbol{B}'_{\rm sc} \\
&\quad + \frac{1}{4\pi}(\boldsymbol{\nabla}\times\boldsymbol{B}'_{\rm sc})\times\boldsymbol{B}_1, && (4.33)\\
-i\omega\left(p'_{\rm sc} - c^2\rho'_{\rm sc}\right) &= \frac{(\gamma-1)c^2}{\gamma}\boldsymbol{v}'_{\rm inc}\cdot\boldsymbol{\nabla}\rho_1, && (4.34)\\
-i\omega\boldsymbol{B}'_{\rm sc} &= \boldsymbol{\nabla}\times(\boldsymbol{v}'_{\rm inc}\times\boldsymbol{B}_1). && (4.35)
\end{aligned}$$

The terms on the right-hand side of the above equations act as sources for the scattered waves: this is the Born approximation. Writing all wave variables in the form of equation (4.16) and using the fact that the magnetic field is solenoidal, the above equations reduce to a forced Helmholtz equation for the (k_z, ω) Fourier component of the scattered pressure field, $\tilde{p}_{\rm sc}$:

$$\left(\Delta_{\mathbf{r}} + k^2\right)\tilde{p}_{\rm sc}(\mathbf{r}) = \tilde{S}(\mathbf{r}), \tag{4.36}$$

where $\Delta_{\mathbf{r}}$ is the two-dimensional Laplacian with respect to $\mathbf{r}$ and the source function $\tilde{S}(\mathbf{r})$ is given by

$$\begin{aligned}
\tilde{S}(\mathbf{r}) &= \frac{\gamma-1}{2}\delta(r-R)\partial_r\tilde{p}_{\rm inc}(\mathbf{r}) \\
&\quad - \frac{c^2k^2}{\omega^2}(\Delta_{\mathbf{r}} - k_z^2)[\Theta(r-R)\tilde{p}_{\rm inc}(\mathbf{r})] \\
&\quad - \frac{c^2}{2\omega^2}(\Delta_{\mathbf{r}} - 3k_z^2)\left[\delta(r-R)\partial_r\tilde{p}_{\rm inc}(\mathbf{r})\right]. && (4.37)
\end{aligned}$$

The first term in $\tilde{S}$ is due to the density jump at the tube boundary and the other two terms are due to the direct effect of the Lorentz force on the wave. For the incoming wave, $\tilde{p}_{\rm inc}$, we take the same plane wave as in the exact solution (Eq. [4.17]).

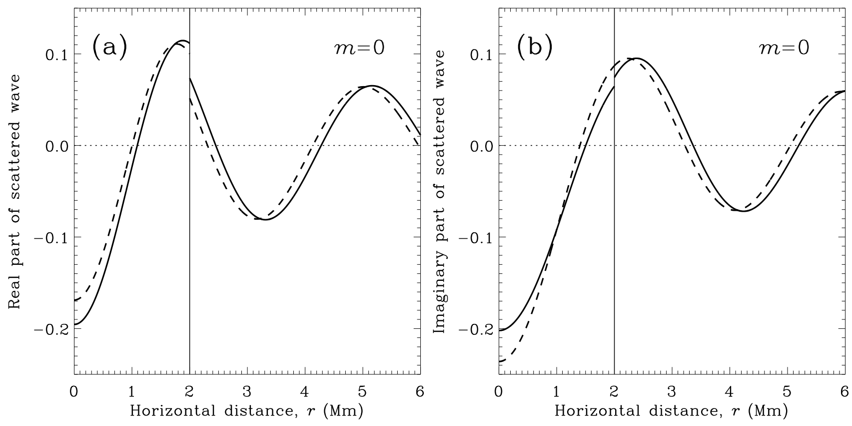

Figure 4.2 a) Real and b) imaginary parts of the scattered pressure field in the Born approximation (dashed line) and the exact solution (solid line). In this case the incoming wave is of the form $\tilde{p}_{\rm inc} = J_0(kr)$ $(m = 0)$ and we used $B = 1$ kG, $R = 2$ Mm, $k_z = 0$, and $\omega/2\pi = 3$ mHz.

The solution to the inhomogeneous Helmholtz equation (4.36) is

$$\tilde{p}_{\rm sc}(\mathbf{r}) = \iint G(\mathbf{r}|\mathbf{r}')\tilde{S}(\mathbf{r}')\,d\mathbf{r}' \tag{4.38}$$

where $G(\mathbf{r}|\mathbf{r}')$ is the Green's function defined by

$$\left(\Delta_{\mathbf{r}} + k^2\right) G(\mathbf{r}|\mathbf{r}') = \delta(\mathbf{r} - \mathbf{r}') \tag{4.39}$$

and explicitly given by (e.g. Morse & Ingard, 1986)

$$G(\mathbf{r}|\mathbf{r}') = -\frac{i}{4}\sum_{m=-\infty}^{\infty} H_m(kr_>)J_m(kr_<)e^{im(\theta-\theta')}, \tag{4.40}$$

where $\mathbf{r} = (r, \theta)$, $\mathbf{r}' = (r', \theta')$, and $r_> = \max(r, r')$ and $r_< = \min(r, r')$.

We insert this expression for G into equation (4.38) and use integration by parts as appropriate. The solution can be written in terms of integrals over bilinear combinations of Bessel and Hankel functions. These integrals can be evaluated using equations (D.3) and (D.4). Upon simplification, we find that the pressure of the scattered wave is

$$
\begin{aligned}
\epsilon\tilde{p}_{\mathrm{sc}}(\mathbf{r}) &= P \sum_{m=-\infty}^{\infty} i^m e^{im\phi} \\
&\times \begin{cases} C_m J_m(kr) - \epsilon \frac{kr}{2} J'_m(kr) & r < R \\ A_m^{\mathrm{Born}} H_m(kr) & r > R, \end{cases}
\end{aligned}
\tag{4.41}
$$

where the coefficients A_m^{Born} and C_m are given in Appendix D.3.

Figure 4.2 shows the real and imaginary parts of the Born approximation for the scattered pressure field, $\epsilon\tilde{p}_{\mathrm{sc}}$, for the case $\tilde{p}_{\mathrm{inc}} = J_0(kr)$, i.e. when $m = 0$ and $P = 1$. In this example, $\epsilon = 0.13$. On the same figure, we also show the exact calculation of the scattered pressure field obtained by subtracting $\tilde{p}_{\mathrm{inc}}$ from the complete exact pressure field, $\tilde{p}$, computed as in Section 4.3. The amplitude of the scattered wave is of order ϵ of the amplitude of the incoming wave, as expected. The Born approximation is everywhere accurate to about 10%.

For a direct comparison with the exact solution (Eq. [4.20]), we remind the reader that the total pressure wave field in the Born approximation is given by $\tilde{p} = \tilde{p}_{\mathrm{inc}} + \epsilon\tilde{p}_{\mathrm{sc}}$, according to equation (4.28).

4.5 Born tends to the exact solution as $\epsilon \to 0$

In this section we show that to first order in ϵ, the exact solution (Sec. 4.3) and the Born solution (Sec. 4.4) are identical. We expand the exact solution (Eqs.[4.20], [D.1], and [D.2]) in a Taylor series up to first order in ϵ. To do this, we use

$$
\frac{a^2}{c^2} = \frac{\epsilon}{1 - \gamma\epsilon/2}
\tag{4.42}
$$

which, together with equation (4.21), gives the first-order perturbation to the wavenumber inside the tube,

$$
k_t(\epsilon) = k(1 - \epsilon/2) + \mathrm{O}(\epsilon^2).
\tag{4.43}
$$

Let us first consider the exact scattering coefficient A_m outside the tube ($r > R$) given by equation (D.1). Denoting the numerator and denominator of A_m by N and D respectively and performing a Taylor expansion, we obtain

$$\begin{aligned} N &= \frac{1}{2}\epsilon\left[(\gamma + 2\frac{c^2 k_z^2}{\omega^2})J'_m(kR)J_m(kR) + kRJ_m^2(kR)\right. \\ &\quad \left. -kRJ_{m-1}(kR)J_{m+1}(kR)\right] + \mathrm{O}(\epsilon^2) \end{aligned} \tag{4.44}$$

and

$$\begin{aligned} D &= J_m(kR)H'_m(kR) - J'_m(kR)H_m(kR) + \mathrm{O}(\epsilon) \\ &= \frac{2i}{\pi kR} + \mathrm{O}(\epsilon). \end{aligned} \tag{4.45}$$

Hence, the exact and Born coefficients outside the tube match to first order in ϵ:

$$A_m = A_m^{\mathrm{Born}} + \mathrm{O}(\epsilon^2). \tag{4.46}$$

Similarly, it can be demonstrated that the coefficient B_m that gives the exact total wave field inside the tube ($r < R$) is

$$B_m - 1 = C_m + \mathrm{O}(\epsilon^2). \tag{4.47}$$

The minus one on the left-hand side comes from the fact that the B_m coefficient relates to the full wavefield, whereas C_m is for the scattered wavefield only. Together, equations (4.46) and (4.47) imply that the Born approximation is identical to the exact solution outside and inside the magnetic tube, to first order in ϵ. Figure 4.3 shows the fractional error $\eta_m = |A_m^{\mathrm{Born}} - A_m|/|A_m|$ as a function of ϵ for $m = 0$, $m = 1$, and $m = 2$. We see that the fractional error of the Born approximation tends to zero as ϵ tends to zero.

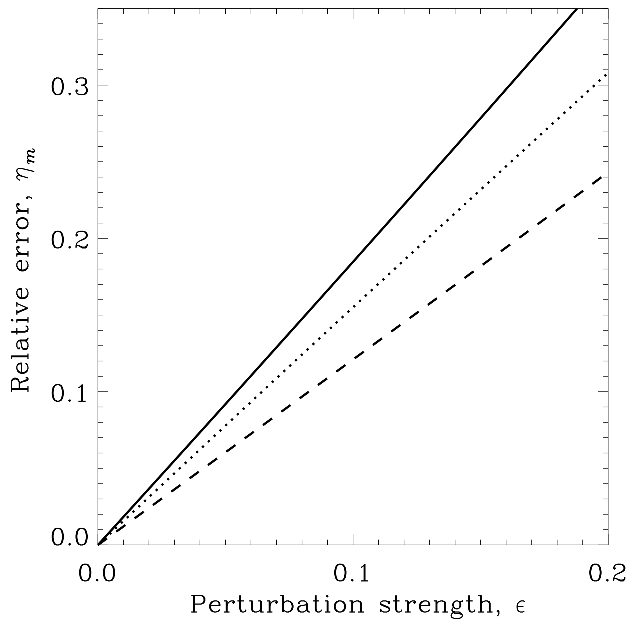

Figure 4.3 The fractional error $\eta_m = |A_m^{\text{Born}} - A_m|/|A_m|$ as a function of ϵ for $m = 0$ (solid line), $m = 1$ (dotted line), and $m = 2$ (dashed line) for the case $R = 2$ Mm, $\omega/2\pi = 3$ mHz, and $k_z = 0$.

4.6 Travel Times

In this section, we study the interaction of solar-like wave packets with the magnetic cylinder. The aim is to compare seismic travel-time shifts computed in the Born approximation and from the exact solution. For the sake of simplicity, we fix $k_z = 0$. Using Cartesian coordinates $\mathbf{r} = (x, y)$ for the horizontal plane, we choose an incoming Gaussian wavepacket propagating in the $+\boldsymbol{x}$ horizontal direction:

$$p'_{\rm inc}(\mathbf{r}, t) = \int_0^\infty e^{-(\omega-\omega_*)^2/(2\sigma^2)} \cos[k(\omega)x - \omega t]\, d\omega. \tag{4.48}$$

where $\omega_*/2\pi = 3$ mHz is the dominant frequency of solar oscillations and $\sigma/2\pi =$ 1 mHz is the dispersion. Since we chose $k_z = 0$, we have $k(\omega) = \omega/c$. The wavepacket is centered on the magnetic tube at time $t = 0$. The scattered wave packet can be calculated, exactly or in the Born approximation, from the previous sections.

The three panels in Figure 4.4 show snapshots of the incoming and scattered pressure fields at time $t = 8.9$ min. The parameters of the steady background at infinity are $\rho_0 = 5 \times 10^{-7}$ cgs and $c = 11$ km/s, which are roughly the conditions at a depth of 250 km below the solar photosphere. The incident wavepacket is shown in Figure 4.4a. Figure 4.4b shows the scattered wave which results from a 1-kG magnetic flux tube with radius $R = 0.2$ Mm. The smaller tube produces relatively more back scattering than the large tube in comparison with the forward scattering. The amplitude of the scattered wave is roughly three orders of magnitude smaller than the incoming wave. Figure 4.4c shows the scattered wave for a larger tube radius of 2 Mm; the scattering is dominantly in the forward direction and has an amplitude only an order of magnitude smaller than the incident wave.

We now define the travel-time shifts that are caused by the magnetic cylinder. By definition, the travel-time shift at location $\mathbf{r}$ is the time $\delta t(\mathbf{r})$ which minimizes the function

$$X(t) = \int dt' \left[p'(\mathbf{r}, t') - p'_{\rm inc}(\mathbf{r}, t' - t)\right]^2, \tag{4.49}$$

where p' is the full wavefield that includes both the incident wavepacket and the scattered wave packet caused by the magnetic field. The travel-time shifts can be

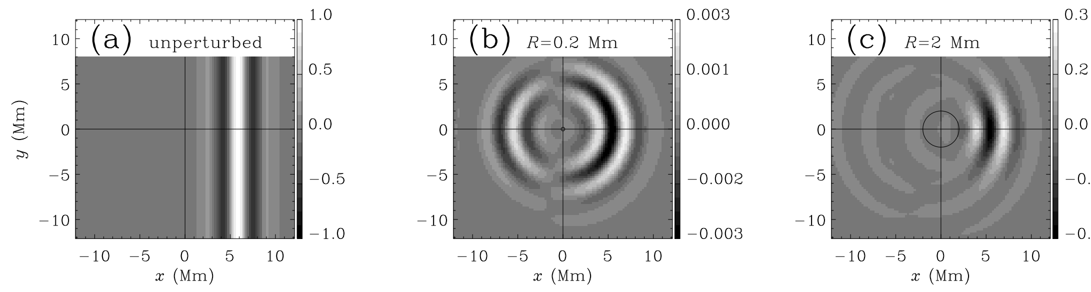

Figure 4.4 Plots of the pressure field of the unperturbed (a) and scattered (b - c) wavepackets at time $t = 8.9$ min after the unperturbed wavepacket has crossed the center of the magnetic cylinder. The wavepacket parameters are described in the text. The wavevector is normal to the axis of the magnetic cylinder and in the $+\hat{\mathbf{x}}$ direction. The strength of the magnetic perturbation is $\epsilon = 0.13$. In panel (b) the tube radius is $R = 0.2$ Mm and in panel (c) is the tube radius is $R = 2$ Mm. The circles outline the cross-section of the tube. Notice that the gray scales are different in each panel. The backscattered wave is more prominent for the tube with the smaller radius (panel b).

computed in this way for either the exact solution or the Born-approximation.

In addition, it is also interesting to compare with the ray approximation as given by equation (14) from Kosovichev & Duvall (1997). In our case, where $\boldsymbol{k} \cdot \overline{\boldsymbol{B}} = 0$ and the magnetic field strength is constant inside the tube, the ray approximation becomes $\delta t(\mathbf{r}) = -L(\mathbf{r})a^2/(2c^3)$ where $L(\mathbf{r})$ is the path length through the tube along the ray which goes from coordinates $(-\infty, y)$ to $\mathbf{r} = (x, y)$.

Figure 4.5 shows travel-time shifts resulting from a flux tube of radius 2 Mm and field strength of 1 kG ($\epsilon = 0.13$). Figure 4.5a shows the exact, Born-, and ray-approximation travel times as a function of x at fixed y. Inside the flux tube, both the Born- and ray-approximation travel times reproduce the exact travel times at a good level of accuracy. As x increases to the right of the tube, wavefront healing (e.g. Nolet & Dahlen, 2000) is seen in the exact and Born approximation travel times. Wavefront healing, however, is not seen in the ray approximation travel times. Figure 4.5b shows the travel times as a function of y at fixed $x = 10$ Mm. The Born approximation reproduces the exact travel times to within 20%. The ray approximation does not

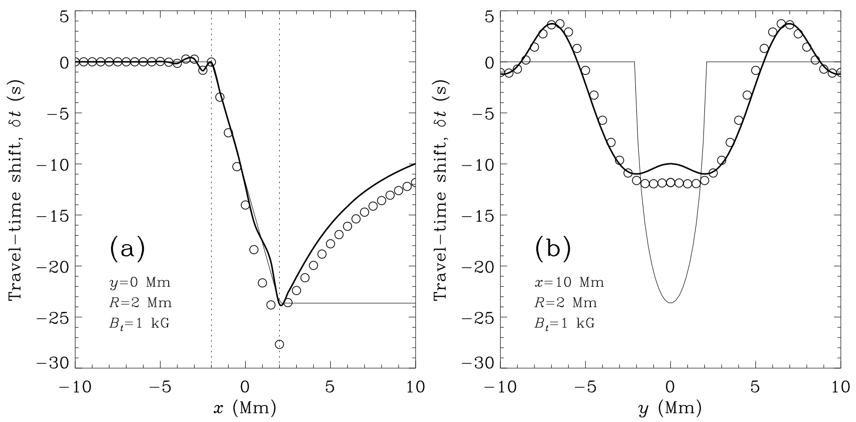

Figure 4.5 Local travel-time shifts $\delta t(\mathbf{r})$ caused by the magnetic cylinder ($\epsilon = 0.13$). The travel times are measured at positions $\mathbf{r}$ in a plane perpendicular to both the cylinder axis. The incoming wavepacket, which moves in the $+\hat{\mathbf{x}}$ direction, is the same as in figure 4.4a. The radius of the tube is $R = 2$ Mm and the tube axis is $(x, y) = (0, 0)$, as shown in figure 4.4c. In both panels the heavy solid line is the exact travel-time shifts, the circles are the Born travel-time shifts, and the light line gives the ray approximation. The left panel shows the travel-time shifts as a function of x at fixed $y = 0$. The right panel shows the travel-time shifts as a function of y at fixed $x = 10$ Mm. The Born approximation is reasonable for this value of ϵ. The ray-approximation does not capture finite-wavelength effects and fails to describe wavefront healing (Nolet & Dahlen, 2000).

capture finite wavelength effects and does not capture the basic behavior of the travel times; it can be inaccurate by many orders of magnitude for $kR \ll 1$. We note that, in Figure 4.5, the contribution of the density jump (first term in Eq. [4.37]) to the travel-time shifts is negligible compared to the contribution from the Lorentz force.

4.7 Discussion

We have computed, in the first Born approximation, the scattering of acoustic waves from a magnetic cylinder embedded in a homogeneous background medium. We showed that in the limit of weak magnetic field, the Born approximation to the scattered wavefield is correct to first order in the parameter $\epsilon = B^2/4\pi\rho c^2$. For typical values of the solar magnetic flux, the Born approximation should be good at depths larger than a few hundred km below the photosphere. The condition $\epsilon << 1$ is satisfied for a 1-kG magnetic fibril at a depth of 250 km ($\epsilon \approx 0.1$) and for a 10^5 G magnetic flux tube at the base of the convection zone ($\epsilon \approx 10^{-7}$). Since the errors introduced by the Rytov and Born approximations are very similar (e.g. Woodward, 1989), we suspect that a travel-time shift computed in the Rytov approximation would also tend to the exact solution as ϵ tends to zero.

Near the photosphere, ϵ is not small. It has been suggested by many authors (e.g. Lindsey & Braun, 2004) that in this case the Born approximation will fail. An exception is the claim by Rosenthal (1995) that the Born approximation will remain valid for kG magnetic fibrils in the limit where the radius of the magnetic element is much smaller than the wavelength. We wish to test this last statement in our simple problem.

Assuming $k_z = 0$ for the sake of simplicity and taking the limit $kR \to 0$, we find that for all ϵ we have

$$\lim_{kR\to 0} \frac{A_m^{\mathrm{Born}}}{A_m} = \begin{cases} 1 + (1-\gamma/2)\epsilon & \text{if } m = 0, \\ 1 - \gamma\epsilon/4 & \text{otherwise.} \end{cases} \tag{4.50}$$

This shows that the Born approximation is not valid in the limit of small tube radius. Figure 4.6 shows the ratio A_m^{Born}/A_m, for $0 \leq m \leq 5$, as a function of R when $\epsilon = 1$ and $k = 3.7$ Mm^{-1}. We see that, in the limit of small kR, the fractional error in the Born approximation is of order ϵ (the absolute error is of order ϵ^2). The Born approximation applied to completely evacuated solar magnetic fibrils in the photosphere is likely to be invalid by roughly a factor of two. Note that the sign of the relative error in A_m^{Born} is different for $m = 0$ and $m > 0$.

The sensitivity of travel times to local perturbations in internal solar properties can be described through linear sensitivity functions, also called travel-time kernels. Gizon & Birch (2002) gave a general recipe for computing such travel-time kernels using the Born approximation, which has been applied to the case of sound-speed perturbations by Birch, Kosovichev & Duvall (2004). The present work suggests that travel-time kernels for the subsurface magnetic field will be useful for probing depths

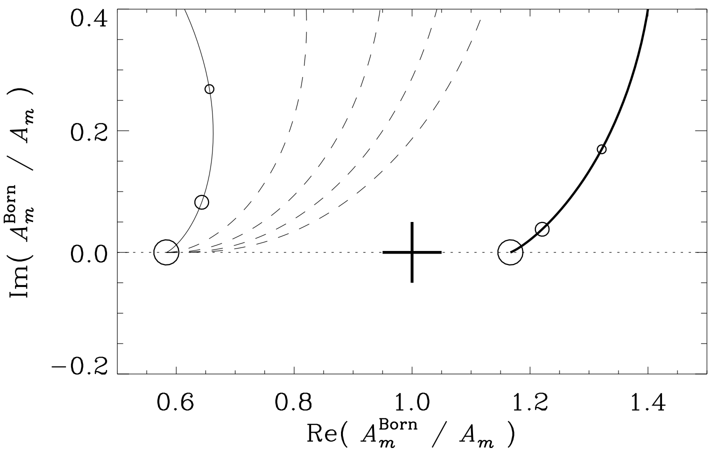

Figure 4.6 Ratio A_m^{Born}/A_m in the complex plane at fixed $\epsilon = 1$ and $k_z = 0$. The ratio is plotted for varying values of the tube radius in the cases $m = 0$ (thick line), $m = 1$ (thin line), and $2 \leq m \leq 5$ (dashed lines). The big circles show the limit $kR \to 0$ given by equation (4.50). If the Born approximation were correct for small tube radii, the big circles would coincide with the cross. The small and medium-size circles are for $kR = 1$ and $kR = 1/2$ respectively.

greater than a few hundred km beneath the photosphere, at least in the case when the travel times are measured between surface points that are not in magnetic regions. One should be careful, however, not to draw definitive conclusions from the simple model we have studied, given the complexity of the real solar problem.

Chapter 5

Scattering by a flux tube

5.1 Introduction[§]

A problem of considerable interest and more recently, controversy, relates to the influence of magnetic fields on acoustic waves in the near surface regions of the Sun. In these sub-photospheric magnetic regions, the ratio of magnetic to gas pressure is very close to unity, leading to the contention that magnetic field effects are systematic and significant. However, due to the difficulties involved in modeling magnetic field effects, most helioseismic analyses tend to ignore these effects, lumping them all into a 'surface term'. The scientific merit of results that invoke this assumption have come into question and in particular, inversions of sunspots have attracted much debate. Owing to the intense magnetic field strengths and the inclination of the field in the penumbra (e.g. Schunker et al., 2003), sunspot structure and dynamics inversions (e.g. Duvall et al., 1996; Couvidat, Birch, & Kosovichev, 2006) have been a source of considerable discussion. Some of these inversions (Couvidat, Birch, & Kosovichev, 2006) use finite-wavelength descriptions of the acoustic wavefield derived from the approximated constituent equations in the Born limit (Birch, Kosovichev & Duvall, 2004). Gizon, Hanasoge, & Birch (2006) showed that although the first

[§] *The results of this chapter are reproduced from Hanasoge, Birch, Bogdan, & Gizon (2007). I wrote this paper, produced all the graphs and did all the calculations. This is work in progress and some sections will be added before submitting it to a journal.*

Born approximation may be valid in regions where the magnetic to gas pressure ratio is much less than unity, its applicability in regions of high magnetic to gas pressure ratios such as sunspots is highly debatable.

Mode conversion (e.g. Barnes & Cally, 2000) is a phenomenon commonly associated with magnetic field induced scattering. From one acoustic mode to another, from acoustic modes to Alfvèn waves and so on, it is estimated that acoustic energy is somewhat redistributed and otherwise lost (in the conversion to Alfvèn waves), contributing perhaps to p-mode absorption observed in sunspots (Braun, 1995). The mode absorption in sunspots detected by Braun (1995) is substantial and until the causal factors are conclusively determined, the relatively simplistic pure acoustic approach in the handling of active regions and sunspots is further threatened.

Kernels are functions that relate perturbations to the consequent travel-time anomalies. Birch, Kosovichev & Duvall (2004) introduced kernels that account for finite wavelength effects to invert for interior sound-speed perturbations. However, obtaining finite-wavelength kernels that invert for magnetic fields has long been a problem of interest for the reason that they allow us to recover the interior magnetic structure. Mathematically speaking, it is a difficult proposition to construct such a kernel from the wave equations because of the complex nature of the Lorentz force term and the induction equation. Applying techniques of time-distance helioseismology (Duvall et al., 1993) on f modes, Duvall, Gizon & Birch (2006), have a extracted kernel for thin magnetic elements from careful measurements of thousands of isolated, small magnetic features. This kernel contains the experimental scattering properties of an 'average' flux tube, information that can be used to establish the effectiveness of theoretical models.

In an attempt to construct an analytical framework to decipher the nature of wave interaction with magnetic regions, Bogdan & Cally (1995), Bogdan et al. (1996) and Barnes & Cally (2000) model a magnetic flux concentration in the thin tube limit placed in a truncated polytrope. Essentially, the flux tube is assumed to be thin enough that variations across its interior are neglected; moreover the tube must be a sub-wavelength feature and the radius small in comparison to the pressure scale height. The parameters of the polytrope are selected so as to mimic the solar sub-photospheric layers as closely as possible and is truncated a little below the photosphere because the rapidly diminishing density makes the thin tube approximation inapplicable very close to the surface.

Bogdan et al. (1996) have demonstrated that the dominant flux tube mode is the kink mode and that the f mode couples strongly with the flux tube. Moreover, measurements of Duvall, Gizon & Birch (2006) are for f modes. Consequently, the focus of this chapter will be to quantify the interaction between an incoming f mode and the resulting kink mode exhibited by the flux tube. Over the next few sections, we describe the analytical model in greater detail, followed by a discussion of the numerical method we apply to extract the scattering coefficients. We then compute the traveltime shifts associated with the flux tube using the method described in Gizon, Hanasoge, & Birch (2006) and compare the phase and amplitudes of the scattered waves with those obtained by Duvall, Gizon & Birch (2006). We conclude with a summary of our calculations and a discussion of the relevance and importance of these results.

5.2 The model

The background model is chosen to be an adiabatically stratified, truncated polytrope with index $m = 1.5$, gravity $\mathbf{g} = -2.775 \times 10^4$ cm s$^{-2}\mathbf{e_z}$, reference pressure $p_0 = 1.21 \times 10^5$ g cm^{-1} s^{-2} and reference density $\rho_0 = 2.78 \times 10^{-7}$ g cm^{-3}, such that the pressure and density variations are given by,

$$p(z) = p_0 \left(-\frac{z}{z_0}\right)^{m+1}, \tag{5.1}$$

and

$$\rho(z) = \rho_0 \left(-\frac{z}{z_0}\right)^{m}. \tag{5.2}$$

We utilize a right-handed cylindrical co-ordinate system in our calculations, with co-ordinates $\mathbf{x} = (r, \theta, z)$ and corresponding unit vectors $(\mathbf{e_r}, \mathbf{e_\theta}, \mathbf{e_z})$. The photospheric level of the background model is at $z = 0$, with the upper boundary placed at a depth of $z_0 = 392$ km. Applying the model of Barnes & Cally (2000), a lower boundary is placed at a depth of 98 Mm. The displacement potential $\Psi(\mathbf{x}, t)$ describing the oscillation modes (t is time) is required to enforce zero Lagrangian pressure perturbation boundary conditions at both boundaries, and is given by:

$$\Psi(\mathbf{x}, t) = \sum_{m=-\infty}^{\infty} i^m N_n s^{-1/2-\mu} J_m(k_n r) e^{i[m\theta - \omega t]} \left[\zeta_n^p M_{\kappa_n^p,\mu}\left(\frac{s\nu^2}{\kappa_n^p}\right) + M_{\kappa_n^p,-\mu}\left(\frac{s\nu^2}{\kappa_n^p}\right)\right]. \tag{5.3}$$

In equation 5.3, we introduce a slew of new symbols,

$$\mu = \frac{m-1}{2}, \quad \nu^2 = \frac{m\omega^2 z_0}{g}, \quad k_n^p = \frac{\nu^2}{2\kappa_n^p z_0}, \tag{5.4}$$

ω the circular frequency of oscillation, $s = -z/z_0$, $J_m(w)$, the Bessel function of order m and argument w and $M_{\kappa,\mu}(w)$, the Whittaker function (e.g. Whittaker & Watson, 1980) with indices κ, μ and argument w. The eigenvalue $\kappa_n^p > 0$ and constant ζ_n^p characterizing the mode are obtained through the procedure described in appendix E. The $n = 0$ mode corresponds to the surface gravity or f mode, while $n > 0$ represents the acoustic p_n mode. The term N_n is the normalization constant for the mode, defined as

$$N_n = \left[\int_1^{\infty} \left[\zeta_n^p M_{\kappa_n^p,\mu}\left(\frac{\nu^2 s}{\kappa_n^p}\right) + M_{\kappa_n^p,-\mu}\left(\frac{\nu^2 s}{\kappa_n^p}\right)\right]^2 ds\right]^{-1/2}. \tag{5.5}$$

5.2.1 Flux tube

Applying the approximations listed in cf. 2 of Bogdan et al. (1996), a thin flux tube carrying a magnetic flux of $\Phi_f = 3.88 \times 10^{17}$Mx, with plasma-$\beta = 1$ everywhere inside the tube is placed in the polytrope. The thin flux tube approximation,

$$b(s) \approx \sqrt{\frac{8\pi p(s)}{1+\beta}}, \quad \pi R^2(s) \approx \frac{\Phi_f}{b(s)}, \tag{5.6}$$

where $b(s)$ and $R(s)$ are the magnetic field and the radius of the tube at depth s, is shown to be accurate to better than a percent in the truncated polytrope situated below $z = -z_0$ or $s = 1$ (Bogdan et al., 1996).

5.2.2 Oscillations of the tube: the kink mode

Motions of the flux tube created by the impinging modes (whose displacement potential is given by $\Psi(\mathbf{x}, t)$) are described by $\xi(s, t)$, a solution to the differential equation

$$\left[z_0 \frac{\partial^2}{\partial t^2} + \frac{2gs}{(1+2\beta)(m+1)} \frac{\partial^2}{\partial s^2} - \frac{g}{1+2\beta} \frac{\partial}{\partial s}\right] \xi = \frac{2(1+\beta)}{1+2\beta} z_0 \frac{\partial^3 \Psi}{\partial x \partial t^2}, \tag{5.7}$$

where $x = r\cos\theta$. Following Bogdan et al. (1996), we define $\xi_\perp = -i\tilde{\xi}(s)$, where $\xi(s, t) = \tilde{\xi}(s)e^{-i\omega t}$, and $\tilde{\xi}(s)$ is the purely spatial component of the tube displacement. The function $\xi_\perp$ contains all of the scattering information that is needed to understand the interaction of the wavefield with the flux tube.

5.2.3 Jacket modes and a lower boundary

Bogdan & Cally (1995) showed that scattered waves created as a consequence of magnetic interactions are a mixture of modal and evanescent components. The scattering process results in not only a redistribution (and loss) of modal energies but also in the production of a continuous spectrum of evanescent 'modes' called *jacket modes*. Mathematically, this uncountable infinity of jacket modes arises as a consequence of the lower boundary being placed at $s = \infty$. A description of jacket modes requires extensive use of Whittaker functions, which are relatively difficult and expensive to compute accurately. Moreover, the jacket mode equations listed in Bogdan & Cally (1995) contain integrals over running indices that pose significant numerical hurdles because of the poor convergence properties of the integral. In order to circumvent any calculations involving these continuous jacket modes, we employ a lower boundary placed at a depth $s = D = 250$ to reduce this uncountably infinite set of evanescent modes to a more manageable discrete countably infinite counterpart in the manner described in Barnes & Cally (2000).

Only modes whose inner turning points are in the vicinity of the lower boundary are affected by its presence and therefore, placing it at a depth of 98 Mm means that the f- and first few p modes remain untouched. Moreover, we expect the scattering amplitude to decay sharply with increasing radial order. Consequently, the high order p modes which interact with the lower boundary are largely unimportant in any case because of their weak contribution to the scattering process studied here. With the introduction of the boundary, the problem becomes numerically well defined as well.

In order to obtain the p- and jacket mode eigenfunctions, we apply a zero Lagrangian pressure perturbation lower boundary condition for the sake of simplicity (see the appendix in Barnes & Cally, 2000). We also assume that the tube oscillations ($\xi_\perp$ in Eq. [5.7]) are oblivious to the lower boundary. This condition is necessary because energy loss in the form of propagating Alfvèn waves along the tube can only occur when the lower boundary is transparent (not the case with zero Lagrangian pressure perturbation).

To summarize, we use the formalism and model of Bogdan et al. (1996) but unable to carry out calculations of the necessary jacket modes described in Bogdan & Cally (1995), we replace this uncommonly difficult continuous set of modes by its more tractable discrete cousin (Barnes & Cally, 2000). Next, we describe the tube radius boundary condition that allows us to begin the task of estimating the scattering coefficients.

5.2.4 The tube boundary

Since we are mainly interested in the interaction of the f mode with the flux tube, the velocity potential of the incident wave, denoted by $\Psi_{\rm inc}$ is given by:

$$\Psi_{\rm inc} = \sum_{m=-\infty}^{\infty} i^m J_m(k_0^p r)\Phi_p(\kappa_0^p; s)e^{i[m\theta-\omega t]}. \tag{5.8}$$

The resonant wavenumber of the p_n mode is denoted by k_n^p (including the $n = 0$ f mode), while wavenumbers corresponding to jacket modes are labelled k_n^J. The eigenvalues $\kappa_n^J > 0$ and κ_n^p are related to k_n^J and k_n^p respectively, according to equation (5.4) (replace p by J in Eq. 5.4). In equation 5.8,

$$\Phi_p(\kappa_n^p; s) = s^{-1/2-\mu}\left[\zeta_n^p M_{\kappa_n^p,\mu}\left(\frac{s\nu^2}{\kappa_n^p}\right) + M_{\kappa_n^p,-\mu}\left(\frac{s\nu^2}{\kappa_n^p}\right)\right]. \tag{5.9}$$

The scattered wave is given by (e.g. Bogdan & Cally, 1995)

$$\Psi_{\mathrm{sc}} = -\sum_{n=0}^{\infty}\sum_{m=-\infty}^{\infty} i^m \left[\alpha_{mn}^p H_m^{(1)}(k_n^p r)\Phi_p(\kappa_n^p; s) + \beta_{mn}^J K_m(k_n^J r)\Phi_J(\kappa_n^J; s)\right] e^{i[m\theta-\omega t]}, \tag{5.10}$$

where α_{mn}^p are the p-mode scattering coefficients, β_{mn}^J are the jacket mode coefficients and $K_m(w)$ is the K-Bessel function of order m and argument w. The un-normalized jacket mode eigenfunction, $\Phi_J(\kappa_n^J; s)$, is given by

$$\Phi_J(\kappa_n^J; s) = s^{-1/2-\mu}\left[\eta_n^J M_{-i\kappa_n^J,\mu}\left(\frac{i\nu^2}{\kappa_n^J}s\right) + M_{-i\kappa_n^J,-\mu}\left(\frac{i\nu^2}{\kappa_n^J}s\right)\right], \tag{5.11}$$

where η_n^J, a parameter and κ_n^J, the jacket mode eigenvalue are determined by the boundary conditions (see appendix A for details) and $M_{\kappa,\mu}(w)$ is the Whittaker function (Whittaker & Watson, 1980). The normal to the tube boundary at a given depth s is given by

$$\hat{\mathbf{n}} = \frac{\mathbf{e_r} - \frac{1}{z_0}\frac{dR}{ds}\mathbf{e_z}}{\left[1 + \left(\frac{1}{z_0}\frac{dR}{ds}\right)^2\right]^{1/2}}. \tag{5.12}$$

The boundary condition is then obtained by matching radial velocities across the tube boundary, $r = R(s)$,

$$\hat{\mathbf{n}} \cdot \boldsymbol{\nabla}\left[\Psi_{\mathrm{inc}} + \Psi_{\mathrm{sc}}\right]_{r=R(s)} = \hat{\mathbf{x}} \cdot \hat{\mathbf{r}}\xi_\perp(s)e^{-i\omega t}, \tag{5.13}$$

where $\hat{\mathbf{x}}$ is the unit vector along the x-axis. Simplifying equation (5.13), we obtain

$$\left[\frac{\partial}{\partial r}(\Psi_{\mathrm{inc}} + \Psi_{\mathrm{sc}}) - \frac{1}{z_0^2}\frac{dR}{ds}\frac{\partial}{\partial s}(\Psi_{\mathrm{inc}} + \Psi_{\mathrm{sc}})\right]_{r=R(s)} = e^{-i\omega t}\xi_\perp(s)\cos\theta\left[1 + \left(\frac{1}{z_0}\frac{dR}{ds}\right)^2\right]^{1/2}. \tag{5.14}$$

Using a least squares approach, equation (5.14) is then solved to obtain an estimate for the scattering coefficients α^p_{mn} and subsequently, the kernel.

5.3 Solution procedure

By only retaining the $|m| = 1$ coefficients and cancelling the $e^{-i\omega t}$ term in equation (5.14), time and angular dependencies may be eliminated. Because we are only dealing with a single m, the scattering coefficients introduced in equation (5.10) are rewritten as α^p_n, β^J_n. We define the following functions

$$f(s) = \frac{i\xi_\perp(s)}{2}\sqrt{1+\left(\frac{1}{z_0}\frac{dR}{ds}\right)^2} + \left(\frac{\partial}{\partial r} - \frac{1}{z_0^2}\frac{dR}{ds}\frac{\partial}{\partial s}\right)[J_1(k^p_0 r)\Phi_p(\kappa^p_0; s)]\,|_{r=R(s)}, \quad (5.15)$$

$$g^p_n(s) = \left(\frac{\partial}{\partial r} - \frac{1}{z_0^2}\frac{dR}{ds}\frac{\partial}{\partial s}\right)\left[H^{(1)}_1(k^p_n r)\Phi_p(\kappa^p_n; s)\right]|_{r=R(s)}, \quad (5.16)$$

$$g^J_n(s) = \left(\frac{\partial}{\partial r} - \frac{1}{z_0^2}\frac{dR}{ds}\frac{\partial}{\partial s}\right)\left[K_1(k^J_n r)\Phi_J(\kappa^J_n; s)\right]|_{r=R(s)}, \quad (5.17)$$

and arrive at the least-squares problem:

$$A\begin{pmatrix}[\alpha]\\ [\beta]\end{pmatrix} = \begin{pmatrix} f(s_1) \\ ... \\ f(s_M)\end{pmatrix}. \quad (5.18)$$

In equation (5.18), s_1 and s_M (M is the number of grid-points in depth) are the start and end of the finite vertical domain, $[\alpha], [\beta]$ are column vectors of the scattering coefficients, α^p_n and β^J_n and the $M \times (N_1 + N_2 + 1)$ matrix A is given by:

$$A = \begin{pmatrix} g^p_0(s_1) & ... & g^p_{N_1}(s_1) & g^J_1(s_1) & ... & g^J_{N_2}(s_1) \\ ... & ... & ... & ... & ... & ... \\ g^p_0(s_M) & ... & g^p_{N_1}(s_M) & g^J_1(s_M) & ... & g^J_{N_2}(s_M)\end{pmatrix}, \quad (5.19)$$

where $N_1 + 1, N_2$ are the number of p- and jacket modes included in this calculation, respectively. The grid spacing in the s space was set at $\Delta s = 0.249$ or correspondingly,

Table 5.1. Scattering coefficients

Mode	Amplitude	Phase
f	0.00757	39.6
p_1	0.00042	74.7
p_2	0.00021	33.0
p_3	0.00020	12.6
p_4	0.00016	7.40
p_5	0.00011	5.93
p_6	0.00012	2.96

$\Delta z = 97$ km. For physical parameters, we utilize the model described in Bogdan et al. (1996), wherein $m = 1.5$, $\Phi = 3.88 \times 10^{17}$ Mx, $R(s = 1) = 100$ km, $z_0 = 392$ km, and incident modes of frequency, $\omega = 2\pi\nu, \nu = 2, 3, 4, 5$ mHz, and $\beta = 0.1, 1, 10$. The lower boundary of the box is set at $D = 250$ or 98 Mm. The thin flux tube approximation may be invoked to ignore the dependence of various terms on derivatives with respect to s in this calculation. Although not shown here, we verified the validity of this approximation by demonstrating the invariance of the scattering coefficients by calculating and comparing them with and without the derivative terms. The coefficients for the first 4 modes were seen to be stable to changes in the depth of the lower boundary, as discussed in §5.2.3.

A large number of jacket modes (463, 675, 820, 900 for $\nu = 2, 3, 4, 5$ mHz respectively) is required to fit the right hand side with the accuracy of Figure 5.1. The least squares fitting was performed using the backslash command in MATLAB. The various complementary and standard Whittaker functions were computed using CERNLIB, a freely available suite of mathematical functions. The absolute values of a sample of the scattering coefficients, $|\alpha_n^p|$ and corresponding phases, $\arg(\alpha_n^p)$ for plasma-$\beta = 1$ and $\nu = 3$ mHz are listed in the second and third columns of table 5.1. We do not display the jacket mode coefficients here.

Our confidence in these values is strengthened by the consistency of these scattering coefficients over a large number of numerical experiments. We show in the upper panels of figure 5.1 that the combination of resonant and jacket modes captures the right hand side very well. In the lower panels, the contributions of the jacket and resonant modes are separated to illustrate that jacket modes are a non-trivial component of the scattering process. Shown in figure 5.2 is the agreement with intuitive expectation that the higher the radial order of the p mode, the lower the contribution. This is in line with the idea that the scattering matrix (Braun, 1995) is nearly diagonal with weak off-diagonal terms that decay very rapidly. In Figure 5.4, we show the phases as a function of frequency, mode number and plasma-β associated the scattering.

5.4 Comparison

There is a definite dependence of the magnitude of the scattering coefficients on the plasma-β and the frequency of the incident wave. It emerges from our calculations that the wave - flux tube coupling becomes stronger as the frequency increases (see Figure 5.2 and 5.3). Moreover, as the flux tube becomes magnetically dominated ($\beta = 0.1$), the scattering is enhanced, as emphasized by the magnitudes of the scattering coefficients. Correspondingly, the flux tube becomes relatively stiff and the tube kink mode is more resistant to the buffeting forces of the interacting modes (upper panel of Figure 5.5). The reverse effect is observed for $\beta = 10$, where the tube is hydrodynamically dominated (lowest panel of Figure 5.5).

5.5 Discussion

We have presented a model of acoustic scattering off a magnetic flux concentration. Earlier efforts to model magneto-acoustic interactions (e.g. Gizon, Hanasoge, & Birch, 2006) have been under less realistic conditions because of the related mathematical difficulties. However, it is noted that this model is not as complex as in the solar case where phenomena such as radiative heat transfer, azimuthal asymmetries in the tube, the lack of applicability of the thin tube approximation, local changes in source properties, downflows, etc. probably play an important role in affecting the wavefield.

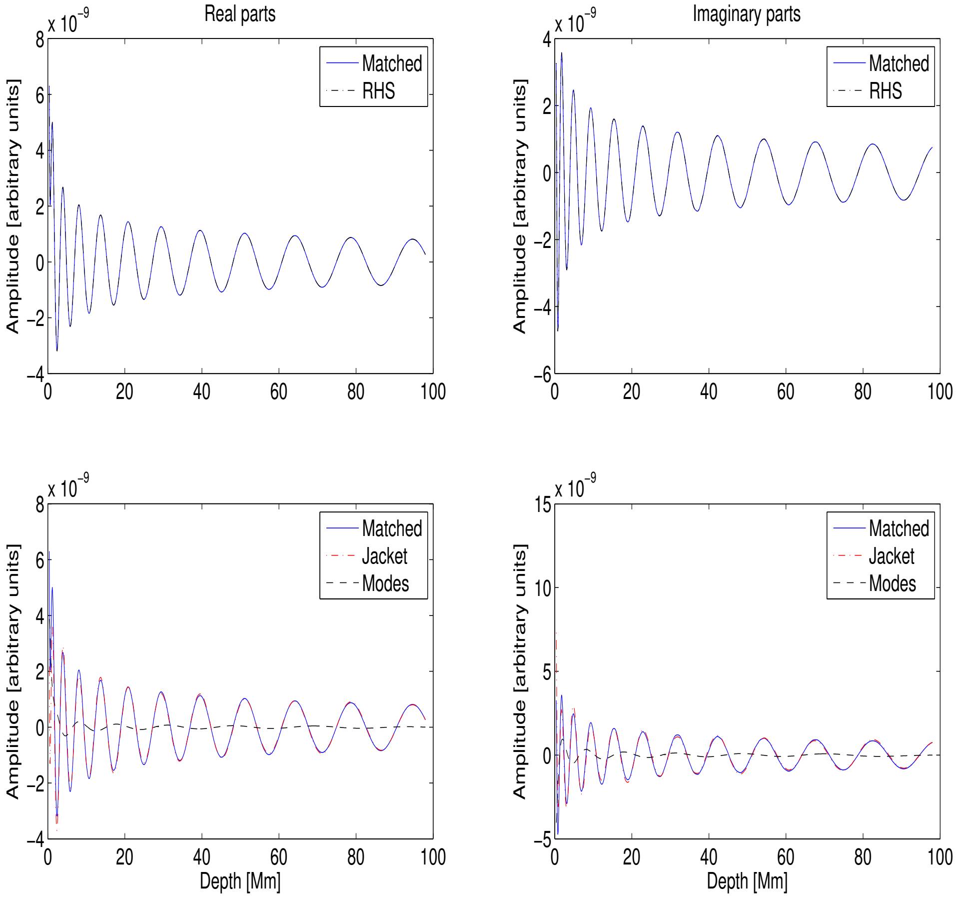

Figure 5.1 The upper panels show comparisons of real and imaginary parts of the fit (labeled 'matched' in the figure) to the corresponding real and imaginary parts of the right hand side (RHS) for $\beta = 1$ and $\nu = 5$ mHz. Contributions to the real and imaginary parts of the right hand side (RHS) respectively from the jacket and resonant modes are shown in the lower panels. The lower boundary was placed at a depth of 98 Mm; the surface gravity mode with 13 acoustic and 857 jacket modes were used in this matching.

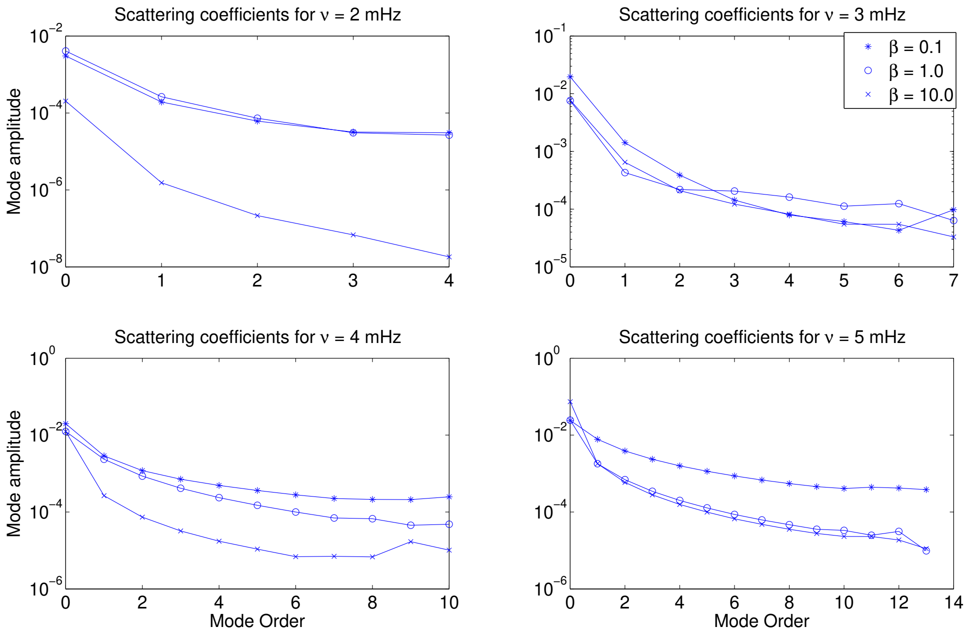

Figure 5.2 The amplitudes of the scattered resonant modes as a function of mode number shown for various values of plasma-β and frequency, ν. The legend applies to all panels.

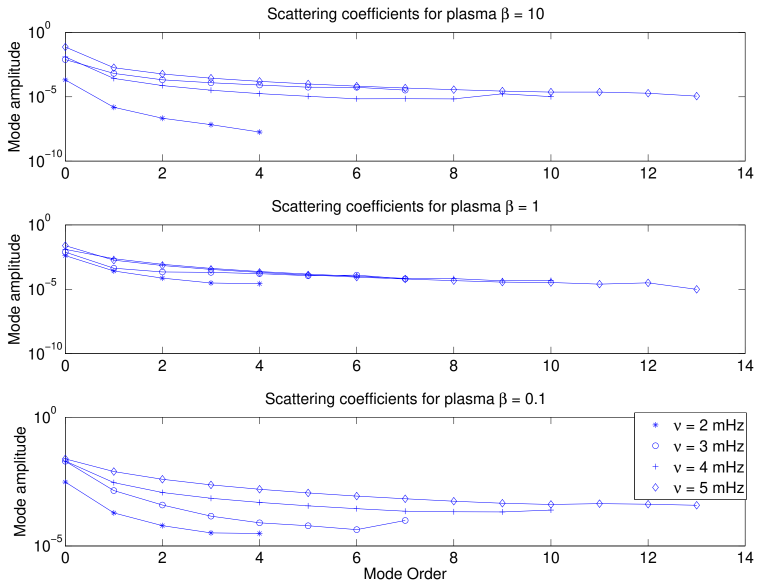

Figure 5.3 The amplitudes of the scattered resonant modes as a function of mode number shown for various values of plasma-β and frequency, ν. The legend applies to all panels.

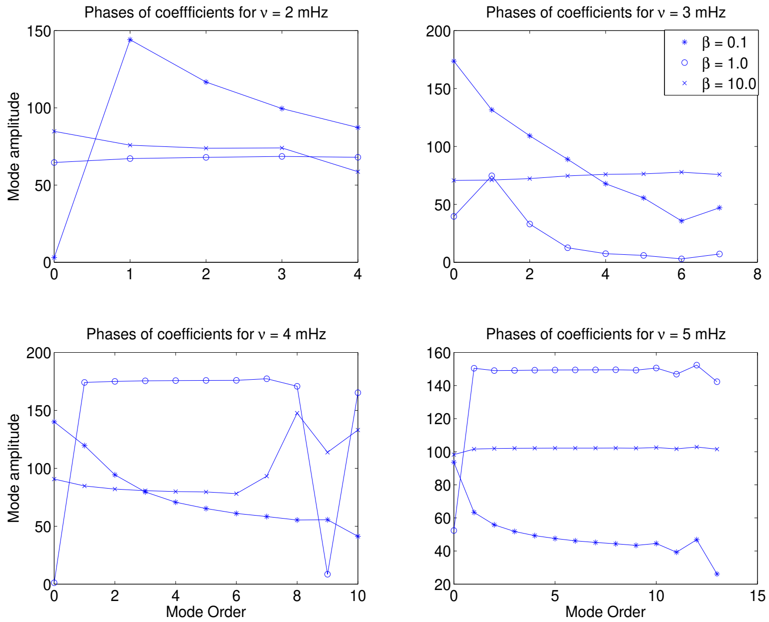

Figure 5.4 The phases of the scattered resonant modes a function of mode number shown for various values of plasma-β and frequency, ν. The legend applies to all panels.

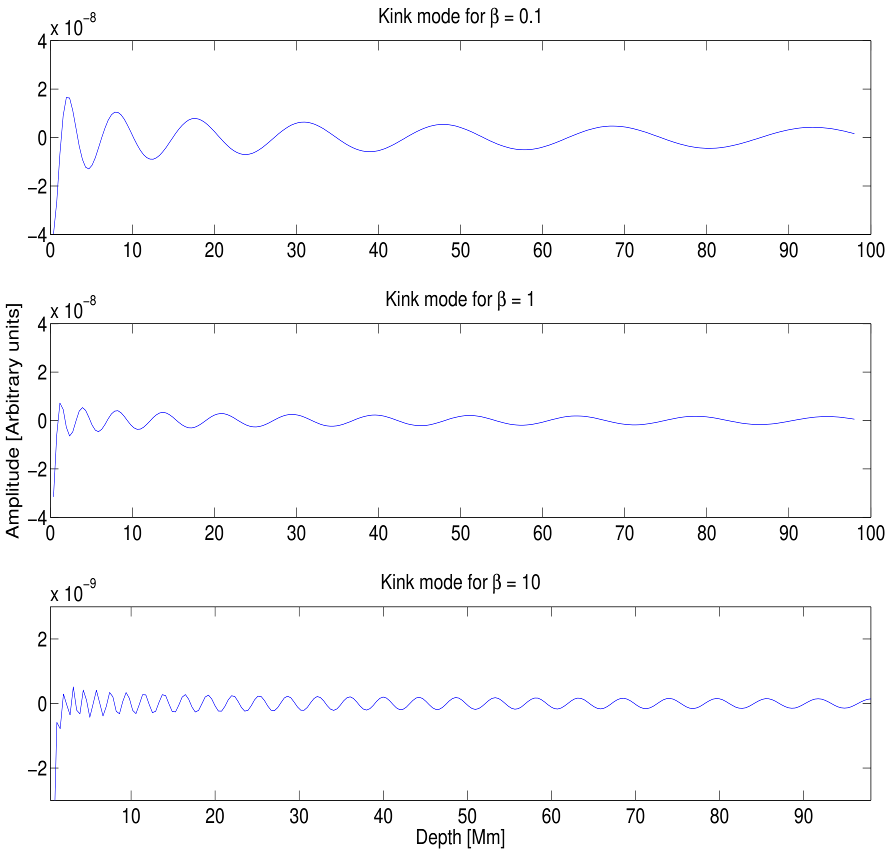

Figure 5.5 The kink mode for $\nu = 5$mHz. The magnetically dominated case with $\beta = 0.1$ is seen to be very stiff, as opposed to the $\beta = 10$ case.

Even under relatively idealized conditions as in this model, the manipulations required to recover the scattering properties are non-trivial.

Assuming that the scattering magnitude goes linearly with the number of these model flux tubes, our calculations seem to indicate that two flux tubes are perhaps sufficient to mimic the extent of the scatter. However, it must be said that the phases of the f mode coefficient differs significantly from data. We do not have an explanation for the poor phase agreement. Perhaps full blown numerical simulations are the only way to progress in this regard.

The various additional complexities apart, it is important to have a theoretical understanding and a model to appreciate the process of magneto-acoustic interactions. While numerical simulations are powerful tools to approach a more general set of problems, it is quite useful to develop an analytical treatment of a comparable situation, as we have attempted to do in this chapter. Such results can provide benchmarks to direct computations of these complex interactions.

Chapter 6

Concluding remarks

The main focus of this work was on developing numerical methods to simulate the acoustic wavefield of the Sun. These calculations are important from the viewpoints of interpreting some results of global and local helioseismology and constructing a clearer picture of acoustic wave propagation and interaction. In terms of helioseismology, there are two significant regimes in the Sun, the deep interior and the near-surface envelope, where the operating physical principles are dramatically different. Just underneath the photosphere lies a seething bed of complexity made so by the competing forces of magnetic fields, plummeting pressure and density, radiation, turbulence, ionization, etc. Things seem to change much more slowly and with less drama in the deep interior, creating this putative natural separation of scales (spatial and temporal). Two different methods, one incorporating spherical geometry to study global phenomena and another to tackle near-surface, approximately Cartesian regions were developed to address these questions.

The ultimate purpose of this study would be construct a full forward acoustically imaged model of the Sun. To do so will presumably require the gradual accumulation of various aspects of solar dynamics and structure. Taking into account all these phenomena at once would defeat the purpose of the work presented here, since the main goal of the effort is to investigate acoustic wave interactions in the Sun. The numerical procedures discussed in chapters 2 and 3 can be used to address a large number of the questions listed herein.

6.1 Forward modeling and helioseismology

There are numerous questions of interest and importance in the context of global resonant modes and their evolution with the solar cycle, their sensitivities to local changes in the background structure of the Sun etc. Merely placing bounds on detectability and quantifying the diagnostic ability of the mechanical modes of the Sun are very instructive tasks. Forward modeling of the near-surface layers of the Sun in the context of seismology is an extremely useful task, firstly because waves spend most of their time in these regions (low sound speed) and secondly, the complexity embedded in these layers are significant contributors to shifts in helioseismic metrics. Various systematics such as the center-to-limb travel-time variation, the strange day to day correlation of noise (Duvall, 2003), foreshortening, the washing machine effect are some problems that can be addressed to some degree with these forward models. Calibration of far-side seismology (Lindsey & Braun, 2000) is a task of relevance to the wider space weather community.

Meridional circulation is thought to play an important role in the solar dynamo and measuring it accurately is linked to understanding the processes of angular momentum exchange. Meridional flow velocities are small ($\sim 20 - 30$ m $\cdot$ s^{-1}) and consequently, they are difficult to measure accurately. By computing the interaction of the acoustic wavefield with various models of meridional flow, the helioseismic signatures obtained thereof can be compared to the solar counterpart to determine which models are most representative. Such a calculation can also give us insight into the signatures associated with a deeper return flow. Controversies associated with the depth of the return flow and the multiple cell meridional flow theory also still remain to be resolved.

The tachocline is a thin layer of intense radial shear across which the solar rotation switches from rigid body to differential. The tachocline is located at roughly 0.70 $R_\odot$ and is considered to be the seat of the solar dynamo. Acoustic signals that penetrate deep enough to sample the tachocline are quite weak when measured at the surface (due to various reasons mentioned in chapter 1), which makes it hard to infer properties of the tachocline accurately. An estimate of the kind of signal to noise required to image this depth and the resolution of the acoustic waves at this depth are important parameters in observational studies of the tachocline.

The impact of diffractive healing on the detectability of perturbations in the solar interior is still an open and unanswered question. Because finite frequency waves possess the curious property of *wavefront healing*, a diffractive effect, some memory of the interactions of waves with perturbations is lost, especially when the wave must propagate large distances (compared to the wavelength) before detection. The size of a perturbation in comparison to the wavelength is quite an important parameter since the wave is likely to heal much more rapidly after it interacts with a small perturbation as opposed to large sized perturbations. Moreover, the ray approximation departs significantly from wave theory as the perturbation becomes sub-wavelength in size. Such studies, especially in the case of global helioseismology, are instructive because we will be able to characterize the inferential ability of waves and obtain estimates on the quantity of data required to probe the deep interior of the Sun.

The interaction of waves with deep convection to see if convective structures have a measurable effect on acoustic wave travel times is an interesting question. Convection in the deep interior is believed to be possess large-scale coherence, lending them the name 'Giant Cells'. These cells have never been convincingly detected; analyses of the helioseismic signatures of the convective flows might lend some insight into the future possibility of giant-cell detection. Initial calculations of travel time shifts of waves with the ASH (Miesch et. al., 2000) convection profiles are somewhat encouraging, although much work needs to be done to characterize the observational effort required to detect interior convection. Because of the large wave-lengths of the propagating acoustic waves at this depth, the resolution with which the convective activity can be imaged is highly limited. Therefore, it would seem that numerical calculations (Miesch et. al., 2000) in conjunction with observational support of the statistical aspects of the interior convection are the only way to proceed, thus highlighting the importance of these measurements.

The realization noise associated with stochastic excitation of acoustic waves interferes with the ability of helioseismology to infer the subsurface solar properties.

Although with current setup, realization noise subtraction is only viable in the numerical case, the possibility of extending it to actual solar data is very tantalizing and no doubt, a scientifically rewarding task. With the constant improvement in the quality of observational data, it seems that the next significant advance would be to model away this realization noise.

6.2 Magnetic field effects

Sunspots are a class of solar phenomena that seem to possess formidable complexity whose structure and dynamics still elude clear comprehension. From the so-called dynamical disconnection of sunspots and their seeming irreverence for neighbouring convective activity (Schüssler & Rempel, 2005) to the strange behemoth that is the penumbra, sunspots are a source of major controversy. Such significant magnetic activity is not related to just the Sun; quite contrarily, some stars exhibit giant spots that grow to occupy a large fraction of the surface area, rendering sunspot seismology relevant to the larger astrophysical community. Ever since the discovery by Thomas, Cram, & Nye (1982) that waves could be used to investigate the structure and dynamics of sunspots, much effort has gone into modeling magnetic effects on waves. Mode conversion and strong near-surface dispersive mechanisms pose non-trivial analytical and modeling hurdles that have yet to be crossed successfully. Truly, a menagerie of magnetically coupled waves (magnetosonic, slow and fast) are presumably unleashed, especially in near-surface regions where the magnetic and hydrodynamic effects are quite comparable. Because analytical techniques are not general in their applicability, the development of numerical methods (Cameron, Gizon, & Daifallah, 2007; Hanasoge, 2007) to study this problem is much required. Questions that relate to the extent of mode conversion and the somewhat controversial theories of mode absorption (e.g., Braun, Duvall, & Labonte, 1987; Bogdan et al., 1993; Braun, 1995; Parchevsky & Kosovichev, 2006), the presence of flows underneath sunspots, the accuracy of the inversion results etc. are very interesting and remain open.

Appendix A

Altering the background state

Here, we describe the artificially convectively stabilized model used in our computations. The dimensionless radial co-ordinate is denoted by r, where r expresses fractions of the solar radius $R_\odot = 6.959894677 \times 10^{10}$ cm. For $r < 0.98$, background properties as prescribed by model S (Christensen-Dalsgaard et al., 1996) are used. In the range $0.9998 \geq r \geq 0.98$, the empirical formulae:

$$
\begin{aligned}
\rho_0 &= 4.1522194 \left[0.998989 - r + 4.36138(r-0.98)^{2.1}\right]^{2.009828}, &\text{(A.1)}\\
p_0 &= 2.7392767 \times 10^{15} \left[0.998989 - r + 4.36138(r-0.98)^{2.1}\right]^{3.009828}, &\text{(A.2)}\\
g &= -\frac{1}{\rho_0 R_\odot}\frac{dp_0}{dr}, &\text{(A.3)}\\
\Gamma_1 &= \max(\Gamma_1^S, 1.507550), &\text{(A.4)}
\end{aligned}
$$

where Γ_1^S is the first adiabtic index of model S, are implemented. In the region $1.002 \geq r \geq 0.9998$, an isothermal layer is utilized:

$$
\begin{aligned}
\rho_0 &= 4.5260638 \times 10^{-7} \exp[7690.7995(0.9998 - r)] &\text{(A.5)}\\
p_0 &= 1.0252267 \times 10^{5} \exp[7690.7995(0.9998 - r)] &\text{(A.6)}\\
g &= 24998.23 &\text{(A.7)}
\end{aligned}
$$

Density (ρ_0) is expressed in units of g cm^{-3}, pressure (p_0) in dynes cm^{-2}, gravity (g) in cm s^{-2}, the first adiabatic index (Γ_1) is dimensionless, and the sound speed (c) in units of cm s^{-1} is given by:

$$c = \sqrt{\frac{\Gamma_1 p_0}{\rho_0}}. \tag{A.8}$$

Appendix B

Code verification

We demonstrate the accuracy of the pseudo-spectral spatio-temporal numerical scheme using a number of tests. Before delving into the verification details, it is important to understand the parameter regimes of the waves and the limiting factors controlling the simulation timestep. The highest frequency of waves of interest to us are of the order of 6 mHz, corresponding to a timescale of about 167 seconds. The simulation timesteps - 4 seconds for the spherical calculations and 2 seconds for the Cartesian case, are significantly smaller than the period of the oscillations. The calculations are evidently temporally highly over resolved; compared to the 4-10 points per wavelength (ppw) quoted by Hu et al. (1996) and Berland et al. (2006), the simulations operate at between 40-80 ppw. Similarly, as shown in Figure B.1, radial resolution is quite sufficient. In fact, the eigenfunctions of the modes contain a rather small number of nodes (10 - 30 depending on the mode) in comparison to the actual number of grid points. The reason for the excessive spatial resolution is the need to capture the rapid density (pressure) variation with radius. Therefore, the limiting factor in terms of the timestep or CFL number is the large number of density (pressure) scale heights in the computational domain, which is why the spatial and temporal resolutions are so high.

Having stated this, it is important to demonstrate that we are indeed in a high-accuracy regime. Firstly, we demonstrate in Figure B.2 that the boundary conditions cause the error convergence rate of the compact finite differences to drop to fifth

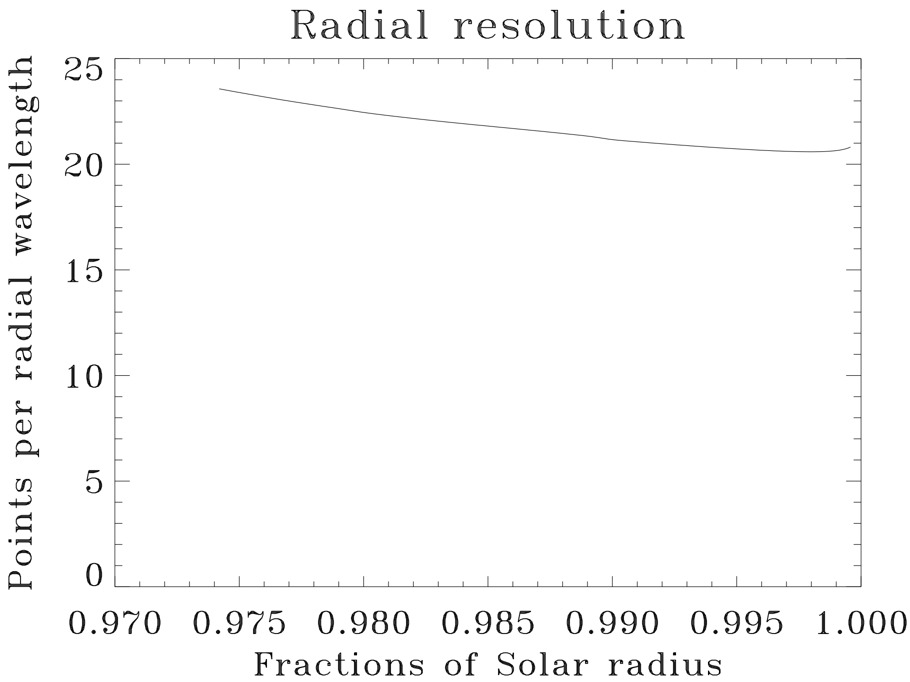

Figure B.1 Resolution in the radial direction as a function of the non-dimensional radius; the solid line shows the grid spacing of the simulation. The wavelength in the radial direction is calculated from equation 2.7. We only display the grid spacing of a small fraction of the solar model, which actually extends from $r = 0.2R_\odot$ to $1.002R_\odot$ ($n_{rad} = 400$). The wavelength becomes a non-trivial fraction of the solar radius by about $r = 0.8R_\odot$, and the resolution monotonically increases with decreasing radius.

order. Although not shown here, the convergence rate is entirely unchanged when the radial de-aliasing filter, described in § 2.5.2, is applied in conjunction with the finite differences. Next, to demonstrate the accuracy of the spatial scheme in its entirety (i.e., when used with radial de-aliasing and the temporal scheme), we simulate the 1-D propagation of a Gaussian wavelet in a box with reflecting boundary conditions. The grid-spacing in the calculation follows the constant travel-time criterion developed in § 2.5.1. The background model is chosen to be an adiabatically stratified, truncated polytrope with index $m = 1.5$, gravity $\mathbf{g} = -2.775 \times 10^4$ cm s$^{-2}\mathbf{e_z}$, reference pressure $p_{ref} = 1.21 \times 10^5$ g cm^{-1} s^{-2} and reference density $\rho_{ref} = 2.78 \times 10^{-7}$ g cm^{-3}, such that the pressure and density variations are given by,

$$p_0(z) = p_{ref}\left(-\frac{z}{z_0}\right)^{m+1}, \tag{B.1}$$

and

$$\rho_0(z) = \rho_{ref}\left(-\frac{z}{z_0}\right)^{m}. \tag{B.2}$$

The photospheric level of the background model is at $z = 0$, with the upper boundary placed at a depth of $z_0 = 768$ km. This model is similar to the stratification prevalent in the outer layers of the Sun (e.g., Bogdan et al., 1996). Because error convergence rates are very sensitive and easily masked by small errors such as the locations of the comparison points of solutions, we start with a highly resolved 721 point grid and downsample by successively higher rates (every second point, every third point, and so on). The solutions obtained on this sequence of grids are compared with the highly resolved case to obtain the error convergence rate. The lower boundary of the simulation is placed at $z = -20.876$ Mm, with wall-like boundary conditions on both ends ($v = 0, \partial_z p = -\rho g$, at the boundaries). The timestep of the simulation was chosen to be $\Delta t = 0.05$ seconds. The experiment is graphically displayed in Figure B.3 and the error convergence rate is shown in Figure B.4.

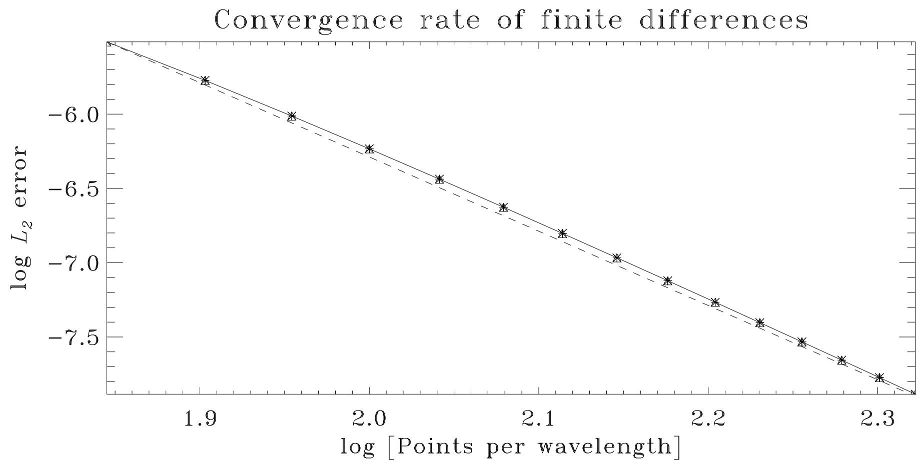

Figure B.2 Spatial convergence rate of the compact finite differences with fifth-order accurate boundary conditions. The solid line shows the accuracy of the scheme, while the dashed line is the theoretical fifth-order accuracy curve.

B.0.1 Eigenfunctions

For the polytrope described above, it is possible to determine the eigenfunctions analytically (e.g., Bogdan & Cally, 1995). This will assist us in verifying that the spatial scheme is able to recover the eigenfunctions accurately. The first step is to set down the equations to be solved:

$$\partial_t \rho(z,t) = -\partial_z(\rho_0 v) \tag{B.3}$$

$$\rho_0 \partial_t v(z,t) = -\partial_z p - \rho g \tag{B.4}$$

$$\partial_t p(z,t) = -c_0^2 \rho_0 \partial_z v + \rho_0 v g, \tag{B.5}$$

where ρ refers to density, c refers to sound speed, the 0 subscript refers to background properties of the model, z is the spatial coordinate and t time. Differentiating equation (B.4) with respect to time and substituting for time derivatives of density and pressure from equations (B.3) and (B.5) respectively, we obtain the following:

$$\rho_0 \partial_t^2 v(z,t) = -\partial_z(-c_0^2 \rho_0 \partial_z v + \rho_0 v g) + \partial_z(\rho_0 g v). \tag{B.6}$$

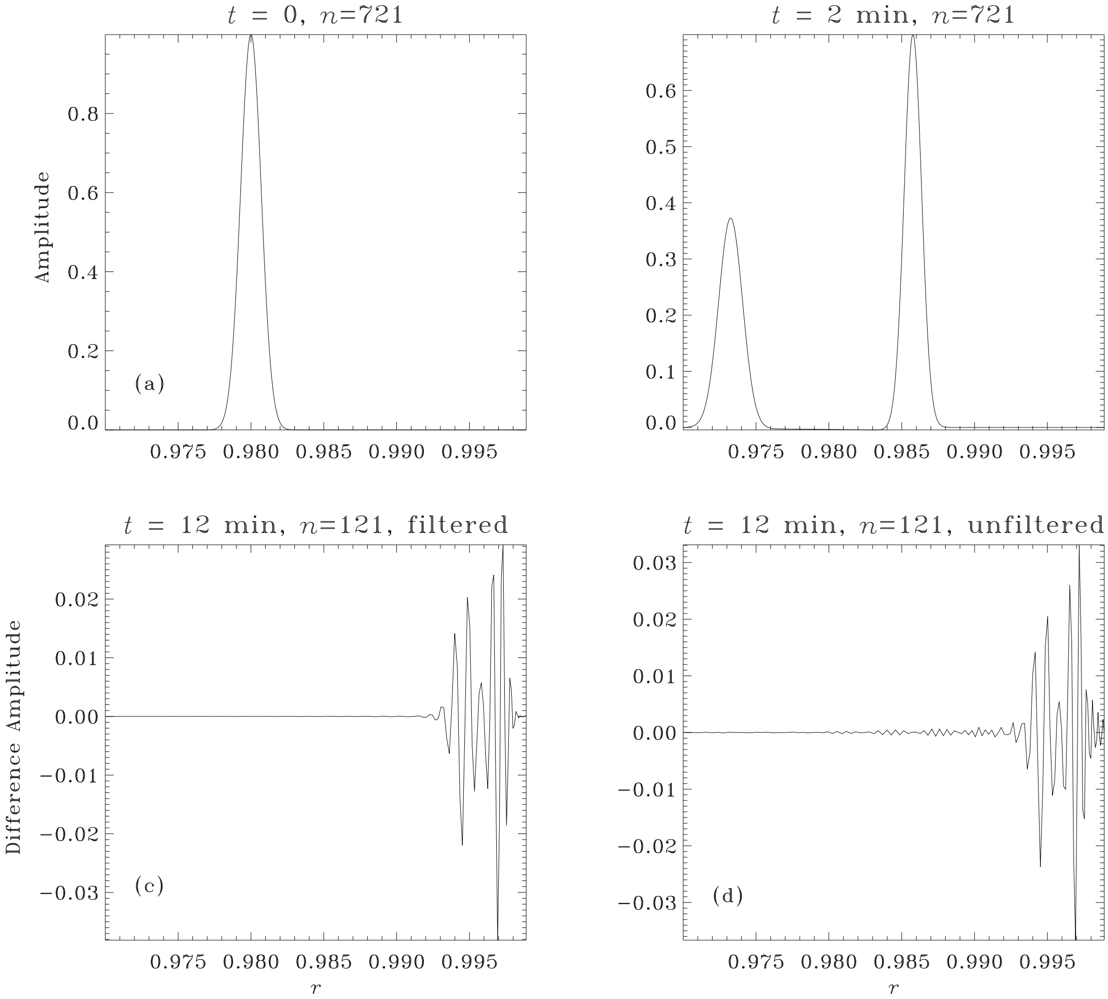

Figure B.3 Experiment to determine the spatial error convergence rate. The initial condition, a Gaussian wavelet in velocity, is shown in panel (a). In (b), the temporally evolved wavelet at time $t = 2$ min is displayed. Simulations are performed with varying numbers of grid points, $n = 721, 361, 181, 145$, and 121, so that each grid is a downsampled version (i.e., every other point, every third point etc.) of the $n = 721$ case. Errors are computed at $t = 2$ min using a downsampled version of the $n = 721, t = 2$ min solution as a template (panel b). In panels (c) and (d), the differences between the $n = 121$ solution and the downsampled $n = 721$ template at $t = 12$ min are displayed; it is seen that the difference, interpreted as the error, is greater in the unfiltered case in panel (d) than in the filtered version in panel (c), where the filter is applied to dealias variables in the radial direction (§ 2.5.2). The difference between (c) and (d), which although appears harmless, continues to grow, eventually overwhelming the simulation unless a de-aliasing filter is applied frequently.

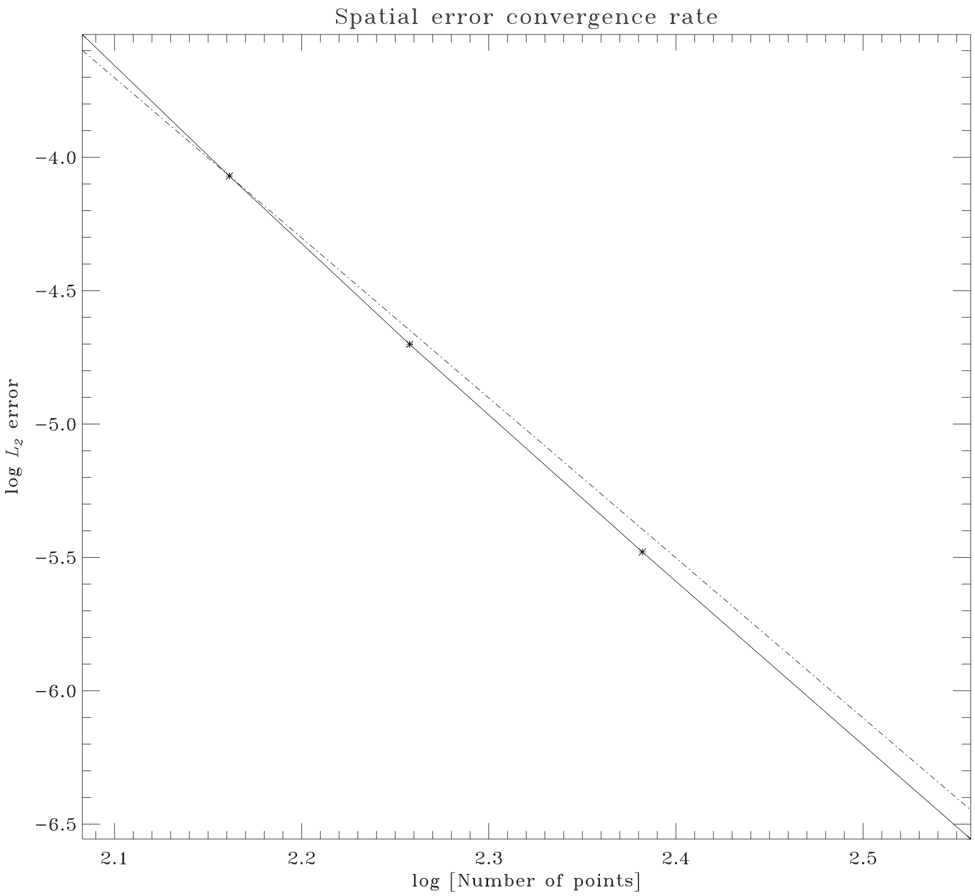

Figure B.4 Spatial error convergence rate (with radial dealiasing) based on the experiment of Figure B.3; the time step was $\Delta t = 0.05$ seconds. The solid line is the error of the compact finite differences and the dashed line is a theoretical sixth-order accuracy accuracy curve. It is somewhat surprising that the scheme obeys a sixth-order accuracy law despite the use of fifth-order boundary conditions. Partly, the reason could be that the problem is a consistent initial-boundary value problem, i.e. $v = 0$ and $\partial_z p = -\rho g$ at the boundaries.

Next we define the Eulerian pressure and velocity fluctuations to be, respectively:

$$p(z,t) = \int_{-\infty}^{\infty} d\omega \tilde{P}(z,\omega) e^{-i\omega t} \tag{B.7}$$

$$v(z,t) = \int_{-\infty}^{\infty} d\omega \tilde{V}(z,\omega) e^{-i\omega t}, \tag{B.8}$$

where,

$$\tilde{P}(z,\omega) = e^{-\frac{(\omega-\omega_0)^2}{2\Omega^2}} p^*(z,\omega), \tag{B.9}$$

$$\tilde{V}(z,\omega) = e^{-\frac{(\omega-\omega_0)^2}{2\Omega^2}} v^*(z,\omega). \tag{B.10}$$

Substituting these expressions into equation (B.6), we have:

$$-\omega^2 \rho_0 z_0^2 v^* = \partial_s (c_0^2 \rho_0 \partial_s v^*), \tag{B.11}$$

where once again, $s = -z/z_0$, $\rho_0 = \rho_c s^m$, $p_0 = p_c s^{m+1}$, $c_0^2 = \tilde{c^2} s$, and $\rho_c, p_c, \tilde{c^2}$ are the density, pressure and sound speed square at $s = 1$. Equation (B.11) is simplified to obtain:

$$s\partial_s^2 v^* + (m+1)\partial_s v^* + \frac{\alpha^2}{4} v^* = 0, \tag{B.12}$$

where $\alpha = 2\omega z_0/\tilde{c}$. Equation (B.12) is solved to obtain the analytical expression for the eigenfunction:

$$v^* = A s^{-m/2} J_m(\alpha s^{1/2}) + B s^{-m/2} Y_m(\alpha s^{1/2}). \tag{B.13}$$

The constants A and B are determined by enforcing the boundary conditions $v^*(s = 1) = 0$ and $v^*(s = D) = 0$. From these conditions emerge a sequence of resonant frequencies, α, which can then be used to obtain the eigenfunctions of the resonant modes. The eigenfunction for pressure is related to the one for velocity according to:

$$p^* = \frac{i}{\omega} \left[\rho_0 v^* g + \frac{c_0^2 \rho_0}{z_0} \partial_s v^* \right] \tag{B.14}$$

$$p^* = \frac{2i\rho_c \tilde{c}}{\alpha} s^m [m v^* + s\partial_s v^*]. \tag{B.15}$$

To obtain eigenfunctions from the calculations, we first excite and simulate wave propagation in the above-described cavity. Temporal transforms of the entire dataset are computed at each spatial location; resonant modes are then isolated by analyzing large amplitude regions in the power spectrum. These frequencies are compared to the analytically predicted values to ensure that these are indeed resonant modes. Having done so, the temporal spectrum is multiplied by a frequency-window function to retain power only in the region of interest and inverse Fourier transformed. The spatial extent of the eigenfunction of interest is then observed at temporal points that correspond closely to the period of the mode. However, spatial error convergence rates are difficult to measure from this experiment because the eigenfunction signal is diluted by neighbouring modes due to the finite temporal window of the simulations. Moreover the accuracy with which the resonant frequency can be measured is bounded by the time length of the calculation. For the eigenfunction shown in Figure B.5, a resonant mode with $\nu = 6.6111$ mHz was isolated using an extremely narrow, four-point box-car type frequency filter. Simulations with varying grid spacings all showed a peak in the power spectrum at frequency of 9 μHz away from the analytical prediction (frequency resolution $\sim 22\mu$Hz, from a 12-hour simulation).

B.0.2 Efficacy of the transmitting boundary

As described in § 2.2, we use the transmitting boundary conditions of Thompson (1990) with an adjoining sponge (e.g., Lui, 2003) to 'prepare' the waves for the boundary. The main reason for using this prescription as opposed to other possibilities (Giles (1990); Poinsot & Lele (1992); see Colonius (2004) for a review) is the ease of implementation and efficiency of the method.

To test if these boundary conditions change the eigenfunction in any significant manner and to ensure that to large extent, they are indeed non reflecting, we perform 1D calculations of wave propagation through a background similar to that of § B.0.1. Tests of eigenfunctions corresponding to the full 3D spherical case are made difficult by the lack of analytical solutions, especially for those corresponding high-l, high frequency wave modes. Moreover, since ADIPACK allows a specific set of boundary

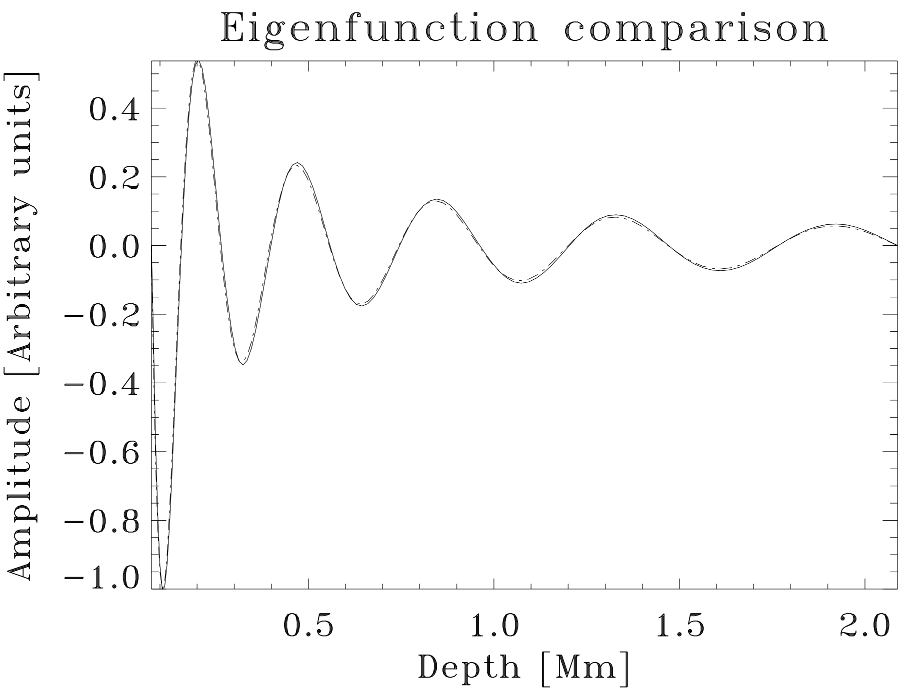

Figure B.5 Comparison of eigenfunctions for a resonant mode of frequency $\nu = 6.6111$ mHz, obtained analytically (solid line) and through simulation (dot-dash line) with $n = 121$. At higher resolutions, the two curves are virtually indistinguishable and hence are not shown here. Including the two boundaries, the eigenfunction contains only eleven nodes, far smaller than the number of grid points. With fewer ($\lesssim 80$) points, the system develops instabilities because of the steep density gradient.

condition options (different from the ones implemented in § 2.2), we are unable to place bounds on the error in capturing these modes in simulations that use a solar-like model as the background state in conjunction with the sponge.

However, in the 1-D situation discussed above, we give the problem a realistic spin by stitching an isothermal atmosphere to the polytrope so that the acoustic cut-off frequency is raised, providing a natural reflection region for the waves. Moreover, having computed the eigenfunctions of the interior (Eq.[B.13]), we relax the zero-velocity condition on the upper boundary while still enforcing a zero-velocity condition on the lower boundary. Waves whose frequencies are lower than the acoustic cutoff are reflected back into the interior while an evanescent non-propagating region develops in the isothermal atmosphere. Thus, we can determine the effect of the boundary conditions on the simulated eigenfunctions by comparing them with their analytical counterparts.

B.0.3 Evanescent behaviour

Let us assume an isothermal evanescent region with constant sound-speed c_0 with exponentially decaying density and pressure profiles:

$$\begin{aligned} \rho_e &= \rho_c e^{-(z_0+z)/H}, && \text{(B.16)} \\ p_e &= p_c e^{-(z_0+z)/H}, && \text{(B.17)} \\ T_e &= T_c, && \text{(B.18)} \end{aligned}$$

with $x = 0$ corresponding to the 'photosphere' of this model, and H to the scale height in the atmosphere. Differentiating equation (B.4) w.r.t. time and substituting for time derivatives of density and pressure from equations (B.3) and (B.5),

$$\begin{aligned} \rho_e \partial_t^2 v &= -\partial_z \left[\rho_e g v - c_0^2 \rho_e \partial_z v\right] + \partial_z(\rho_e g') && \text{(B.19)} \\ -\omega^2 v &= \frac{c_0^2}{\rho_e}(\partial_z \rho_e)(\partial_z v) + c_0^2 \partial_z^2 v. && \text{(B.20)} \\ & && \text{(B.21)} \end{aligned}$$

Again, we define $v(z,t), p(z,t)$ as:

$$p(z,t) = \int_{-\infty}^{\infty} d\omega \tilde{P}_e(\omega,t) e^{-i\omega t} \tag{B.22}$$

$$v(z,t) = \int_{-\infty}^{\infty} d\omega \tilde{V}_e(\omega,t) e^{-i\omega t}, \tag{B.23}$$

$$\tag{B.24}$$

where $\tilde{P}_e(\omega,t)$ and $\tilde{V}_e(\omega,t)$ are given by

$$\tilde{P}_e(\omega,t) = e^{-\frac{(\omega-\omega_0)^2}{2\Omega^2}} p_e^*(\omega,z) \tag{B.25}$$

$$\tilde{V}_e(\omega,t) = e^{-\frac{(\omega-\omega_0)^2}{2\Omega^2}} v_e^*(\omega,z) \tag{B.26}$$

$$p_e^* = Be^{\lambda z - z/H} \tag{B.27}$$

$$v_e^* = Be^{\lambda z} \tag{B.28}$$

we obtain the following solution for λ,

$$\lambda^2 - \frac{\lambda}{H} + \frac{\omega^2}{c_0^2} = 0 \tag{B.29}$$

$$\lambda = \frac{1}{2H}\left[1 - \sqrt{1 - \frac{\omega^2}{\omega_a^2}}\right] \tag{B.30}$$

$$\omega_a = \frac{c_0}{2H} \tag{B.31}$$

We obtain two solutions while determining λ, and we reject the solution whose energy density $\propto \rho v^2$ grows without bound. In this situation, the relation between $\tilde{P}_e(\omega,t)$ and $\tilde{V}_e(\omega,t)$ is given by:

$$\tilde{V}_e(\omega,t) = \frac{i\omega}{\rho_c \eta} \tilde{P}_e(\omega,t) \tag{B.32}$$

$$\eta = c_0^2 \lambda - g. \tag{B.33}$$

For boundary conditions, we use normal velocity and Eulerian pressure matching across the boundary:

$$
\begin{aligned}
v^* &= v_e^* && \text{(B.34)}\\
p^* + \frac{\rho_c g}{i\omega} v^* &= p_e^* + \frac{\rho_c g}{i\omega} v_e^* && \text{(B.35)}\\
p^* &= p_e^*. && \text{(B.36)}
\end{aligned}
$$

When writing the velocities in the following form, we will have only the pressure equation to solve:

$$
\begin{aligned}
v^* &= A\frac{i\omega}{\rho_c \eta} e^{-\lambda z_0} s^{-m/2}[J_m(\alpha s^{1/2}) + \beta Y_m(\alpha s^{1/2})] && \text{(B.37)}\\
v_e^* &= A\frac{i\omega}{\rho_c \eta} e^{-\lambda s z_0}[J_m(\alpha) + \beta Y_m(\alpha)], && \text{(B.38)}\\
p_e^* &= A e^{-\lambda s z_0 + s z_0/H}[J_m(\alpha) + \beta Y_m(\alpha)], && \text{(B.39)}\\
& && \text{(B.40)}
\end{aligned}
$$

where β, A are the unknown constants we must determine. Matching $p_e^* = p^*$ at $s = 1$ gives us the following equations:

$$
\begin{aligned}
p^* &= A e^{-\lambda z_0} \frac{2i\rho_c \tilde{c}}{\alpha} \frac{i\omega}{\rho_c \eta} \left[m J_m(\alpha) + m\beta Y_m(\alpha) \right.\\
&\quad \left. + \frac{1}{2}(-m J_m(\alpha) + \alpha J_m'(\alpha)) + \frac{\beta}{2}(-m Y_m(\alpha) + \alpha Y_m'(\alpha)) \right], && \text{(B.41)}\\
p^* &= -A e^{-\lambda z_0} \frac{\omega \tilde{c}}{\alpha \eta} \left[m J_m(\alpha) + \alpha J_m'(\alpha) + \beta(m Y_m(\alpha) + \alpha Y_m'(\alpha)) \right], && \text{(B.42)}\\
\beta &= -\left[\frac{J_m(\alpha) + \frac{\omega \tilde{c}}{\alpha \eta} e^{-z_0/H}[m J_m(\alpha) + \alpha J_m'(\alpha)]}{Y_m(\alpha) + \frac{\omega \tilde{c}}{\alpha \eta} e^{-z_0/H}[m Y_m(\alpha) + \alpha Y_m'(\alpha)]} \right], && \text{(B.43)}\\
\beta &= -\left[\frac{J_m(\alpha) + \kappa J_{m-1}(\alpha)}{Y_m(\alpha) + \kappa Y_{m-1}(\alpha)} \right], && \text{(B.44)}\\
\kappa &= \frac{\omega c_0}{\alpha \eta} e^{-z_0/H}. && \text{(B.45)}
\end{aligned}
$$

To determine the resonant modes of this model, we use the definition of β from equation (B.43) and set equation (B.37) to zero at $s = D$. Having then recovered the resonant frequencies, the corresponding expressions for pressure and velocity in the interior (pure spatial components) may be obtained by evaluating:

$$v^* = A\frac{i\kappa}{\rho_c \tilde{c}} e^{-\lambda z_0 + z_0/H} s^{-m/2}[J_m(\alpha s^{1/2}) + \beta Y_m(\alpha s^{1/2})], \quad \text{(B.46)}$$

$$p^* = -A\kappa e^{-\lambda z_0 + z_0/H} s^{(m+1)/2}[J_{m-1}(\alpha s^{1/2}) + \beta Y_{m-1}(\alpha s^{1/2})]. \quad \text{(B.47)}$$

The acoustic-cutoff frequency, ω_c, of the model ($D \geq s \geq 1$) is given by:

$$\omega_c = \frac{c_0\sqrt{m^2+1}}{2z_0}\frac{1}{\sqrt{s}}. \quad \text{(B.48)}$$

The model for this particular test is parametrized by $m = 1.5$, $z_0 = 768$ km, $D = 90.6198, c_0 = 8.51715$ km/s, $p_0 = 1.21 \times 10^5$ dynes/cm^2, $\rho_0 = 2.78 \times 10^{-7}$ g/cm^3, $H = z_0/(m+1)$ km, and $g = 0.1416$ km/s^2. Plotted in Figure B.6 are the analytical (dotted line) and the simulated (solid line) eigenfunctions. The sponge is placed adjacent to the upper boundary (located 1232 km above z_0), shown in Figure B.7. As can be seen the presence of the sponge does not affect the interior parts of the acoustic eigenfunction. There is an amplitude error near the upper-most region of the polytrope due to the combined influence of the boundary condition and the sponge but the nodes remain mostly unaffected.

A rough test of the efficacy of the boundary conditions is shown in Figure B.8, where an initial Gaussian-shaped velocity impulse is allowed to propagate outward. Panel a shows the situation at $t = 10$ min, and the successive panels show the impulses at later instants in time. The amplitude in panel d is of the order of 10^{-6}, significantly smaller than in panels a through c. Together with the test of Figure B.6, the boundary condition seems to allow outward propagating waves to leave the computational domain while leaving the eigenfunctions relatively undisturbed. A check of this sort was applied to choose the sponge for the real simulations (quite similar in magnitude and structure to the one in Fig. B.7). Since the polytrope + isothermal stratification near the surface is very similar to the model used in the simulations, and since the sponges are quite similar in structure, we expect that the eigenfunctions in the simulations are also well retrieved while the sponge damps the outward propagating waves.

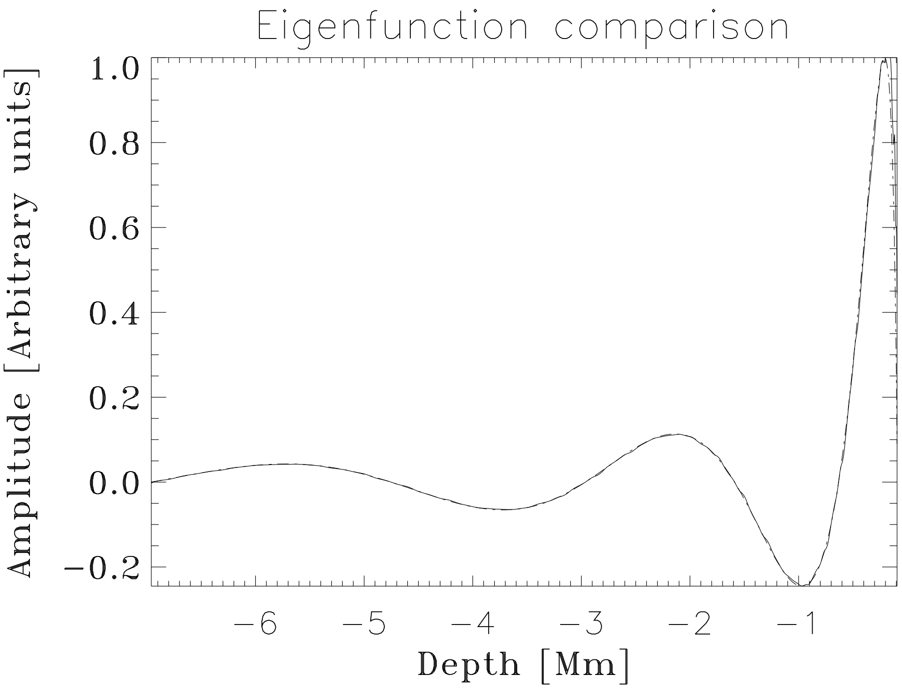

Figure B.6 Simulated (solid line) and analytical (dot-dash line) eigenfunctions for $\nu = 1.68$ mHz, for the model described above. It is seen that the boundary conditions and sponge do not affect the eigenfunction over the region of interest; although there is an amplitude error of a few % in the upper-most layers of the polytrope, the interior nodes are oblivious to the boundary conditions. This eigenfunction was obtained from a 24-hour simulation wherein the waves were constantly excited over a small region in the interior.

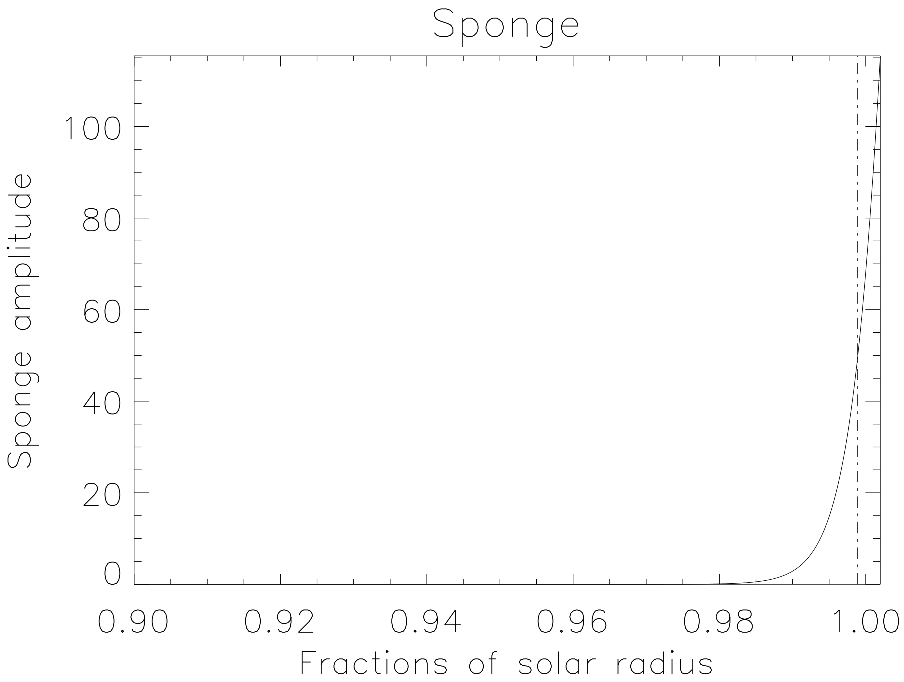

Figure B.7 The sponge (solid line) and the upper boundary of the polytrope (and lower boundary of the isothermal atmosphere) at $s = 1$ (dot-dash line). In simulations with the altered solar model, the sponge is slightly sharper (spatially) and pushed a little farther outward.

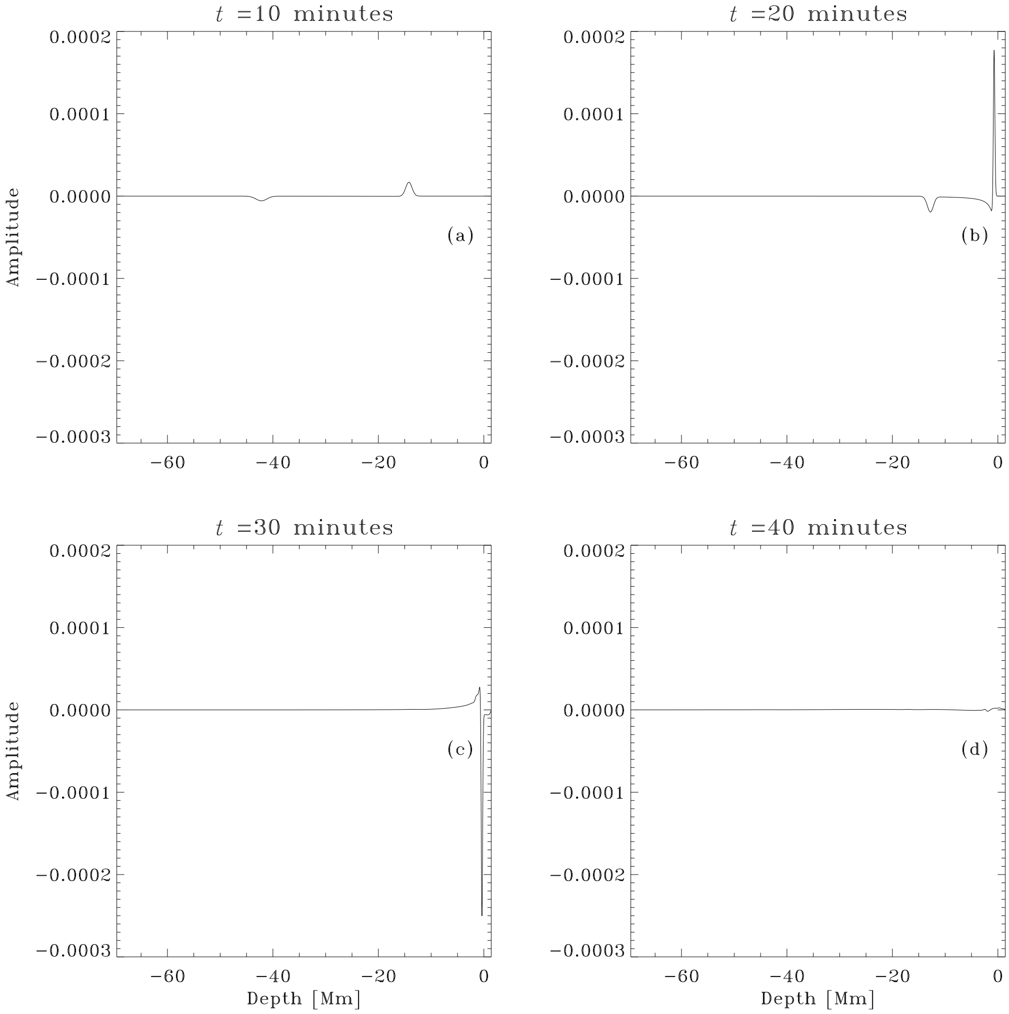

Figure B.8 Efficacy of the transmitting boundary. The initial condition is a Gaussian-shaped velocity impulse. Panel a shows the situation at $t = 10$ min, and the successive panels show the impulses at later instants in time. The amplitude in panel d is of the order of 10^{-6}, significantly smaller than in panels a through c. Together with the test of Figure B.6, the boundary seems to do a relatively good job of removing outward propagating waves while the interior portion of the eigenfunction is seen to be mostly undisturbed.

B.0.4 Spherical Harmonics and the optimized R-K scheme

Because analytical solutions in spherical geometry are difficult to come by, we constructed a simplified problem wherein wave propagation on the 2-D spherical surface (of radius $R = 1$) are studied. Provided background density, pressure are constant at all points on the surface, an analytical solution may be arrived at:

$$\partial_t \rho = -\boldsymbol{\nabla} \cdot \mathbf{v}, \tag{B.49}$$

$$\partial_t \mathbf{v} = -\boldsymbol{\nabla} p, \tag{B.50}$$

$$p = \rho c^2, \tag{B.51}$$

where the notation of the previous section applies here. The equations (B.49) to (B.51) are then simplified to obtain the following equations:

$$\partial_t^2 \rho - c^2 \nabla^2 \rho = 0, \tag{B.52}$$

$$\rho(\theta, \phi, t = 0) = \sum_0^{l_{max}} a_{lm} Y_l^m(\theta, \phi), \tag{B.53}$$

$$\rho(\theta, \phi, t) = \sum_0^{l_{max}} a_{lm} Y_l^m(\theta, \phi) cos(\omega_{lm} t), \tag{B.54}$$

$$\omega_{lm} = c\sqrt{l(l+1)}. \tag{B.55}$$

Thus, the prescribed initial condition, first decomposed into the spherical-harmonic domain in equation (B.53), is evolved in time according to equation (B.54), where each spherical-harmonic coefficient oscillates at the frequency given by equation (B.55). Then, by choosing an initial condition that is completely captured by the spherical harmonics (in this case, $\rho(\theta, \phi, 0) = \cos\theta$), one can demonstrate the temporal error convergence rate, as shown in Figure B.9.

Finally, to show that spherical-harmonic error convergence turns exponential when a function is fully represented, we take the function $f(\theta, \phi) = \cos^{12}\theta \sin^6\phi$ and estimate the L_2 error in computing the latitudinal derivative $(-12\cos^{11}\theta \sin\theta \sin^6\phi)$ at various spherical-harmonic bandwidths (see Figure B.10).

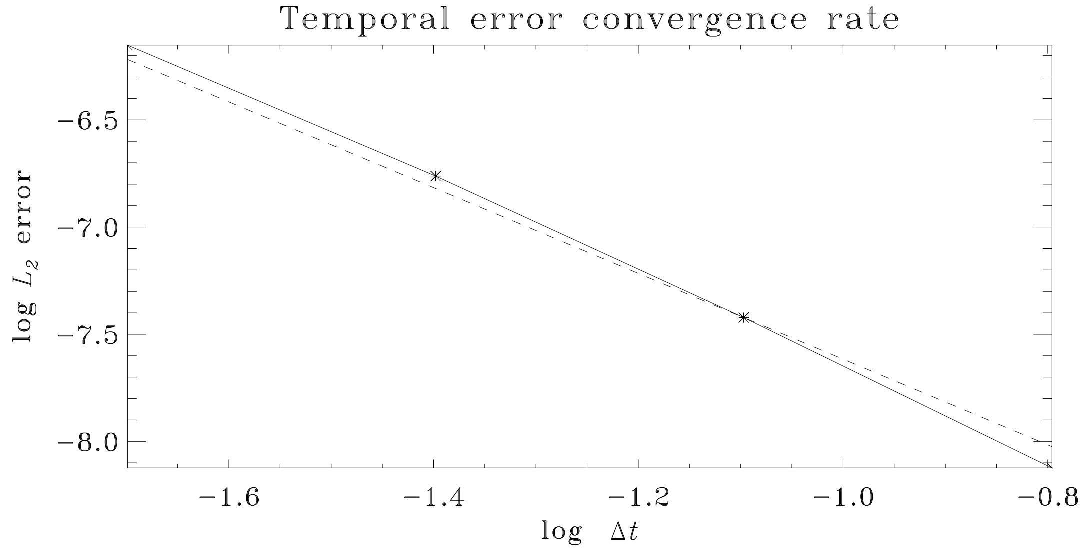

Figure B.9 Error convergence rate of the temporal scheme. The solid line is the error of the second-order five-stage scheme of Hu et al. (1996) and the dashed line is the theoretical second-order accuracy curve.

B.0.5 Measuring reflection phases

A concern with altering the background solar model is the extent of change in reflection phases and the size of the acoustic cavities. In order to measure the phases from simulations, we invoke Duvall's law (Duvall, 1982) which is an observational method to characterize the dispersion relation of the p modes. Because it is a difficult procedure to directly estimate the resonant frequencies from the simulations (requirements of temporally lengthy simulations), we use the frequencies produced by ADIPACK (Christensen-Dalsgaard & Berthomieu, 1991) as a proxy. Because ADIPACK has only a limited set of boundary condition options, the modes at higher frequencies which are more sensitive to the type of upper boundary condition are not represented well. We show in Figure B.11 that the modes with frequencies $\nu \lesssim 3.5$ mHz lie on the p-mode ridges while there are systematic errors at higher frequencies. Based on the results of (Duvall, 1982), we expect resonant modes of different n, l, and ω to collapse on to a single curve. A full theoretical treatment of this result may be found in (e.g.,

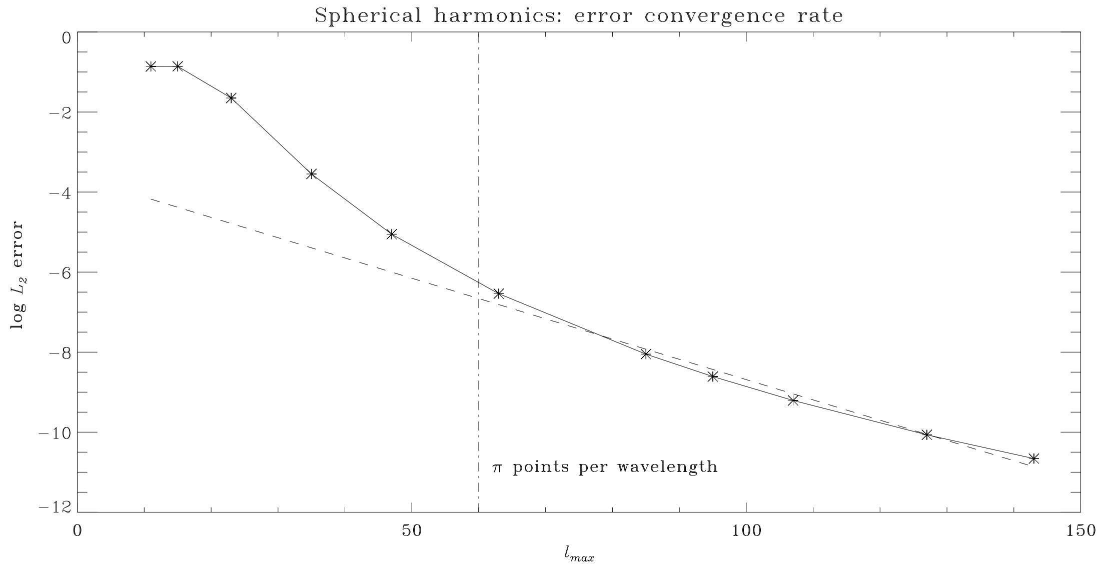

Figure B.10 Error convergence rate plotted against the spherical-harmonic bandwidth, l_{max}. The solid line displays the spherical-harmonic error in evaluating the latitudinal derivative and the dashed line shows the exponential convergence behaviour at high bandwidth. The onset of exponential convergence in the case of (sine/cosine) Fourier series occurs when the grid resolution reaches approximately π points per wavelength. We expect a similar effect to apply to the spherical harmonic basis. Since the number of latitudes n_{lat} must satisfy $n_{lat} \geq l_{max}$, and because $l_{max} = 19$ is sufficient to capture the function $-12\cos^{11}\theta\sin\theta\sin^{6}\phi$, we expect the onset of exponential convergence to occur at $n_{lat} = l_{max} \sim 60$. The vertical dot-dash line indicates this location in the figure.

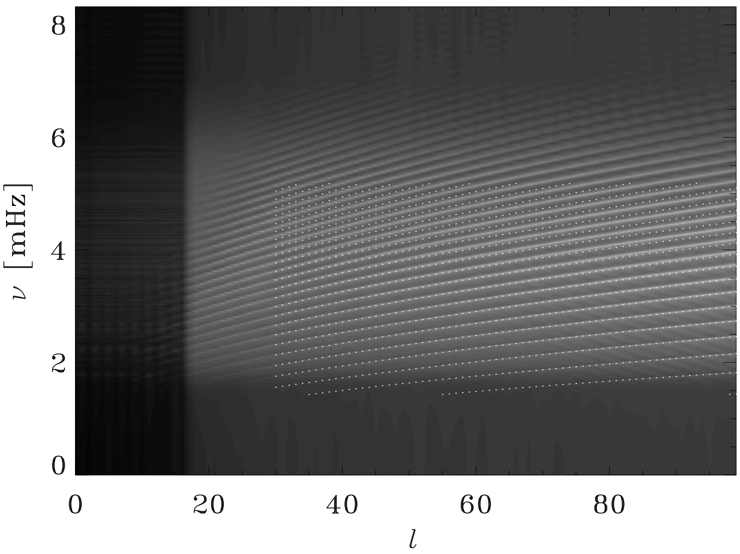

Figure B.11 Power spectrum from a simulation. The dots show frequencies as estimated by ADIPACK (Christensen-Dalsgaard & Berthomieu, 1991). At lower frequencies, we observe a good match between the predicted and simulated dispersion relations, while the agreement is not quite so good at higher frequencies.

Christensen-Dalsgaard, 2003). In Figure B.12 b, we see that indeed, the modes do collapse onto a curve, but with a reflection-phase constant α of 1.05, as compared to $\alpha = 1.13$ for the solar frequencies (panel a). The value of α in the solar case was chosen to minimize the spread between a fifth-order polynomial fit (the dot-dashed line in Figure B.12 a) to the frequencies; it appears that altering the solar model has changed the size of the acoustic cavity and shifted reflection phases to the tune of 0.08 radians or about 4.58°, contributing to a 7% error per reflection. These phase shifts result in systematic changes in the travel times of the p modes, as shown in Figure B.13 (private communication, Olga Burtseva and Shukur Kholikov). The error is small enough that conclusions drawn from these differential studies are probably valid.

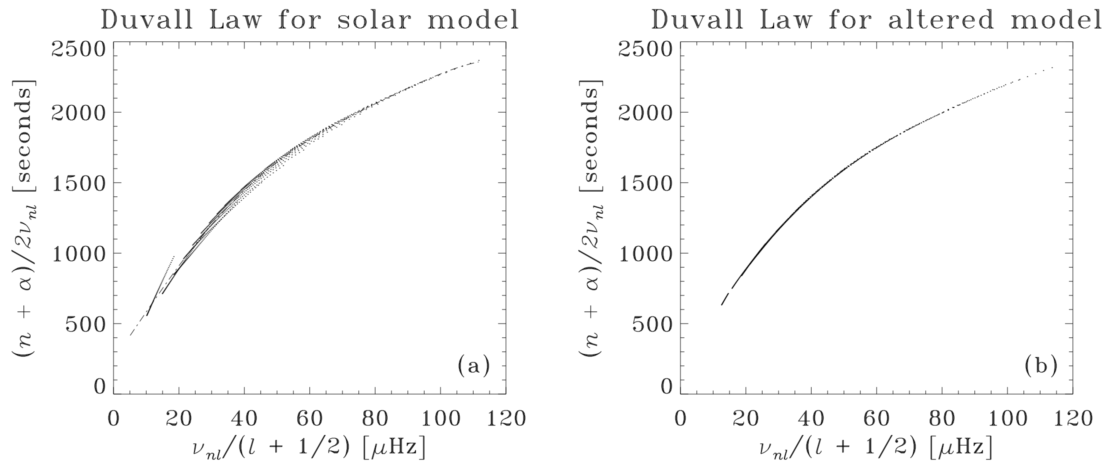

Figure B.12 Duvall's Law (Duvall, 1982) for a solar model (panel a) and the altered model (panel b). Resonant modes (obtained using ADIPACK) of the artificial model used in the simulations collapse onto a single curve as seen in b. $\alpha = 1.05$, minimizes the spread in the altered model, while $\alpha = 1.13$ is the optimal value for the solar frequencies (panel a). The spread in panel a is defined relative to a fifth-order polynomial fit (dot-dash line) to the solar frequencies. The error in the reflection phase is 7%.

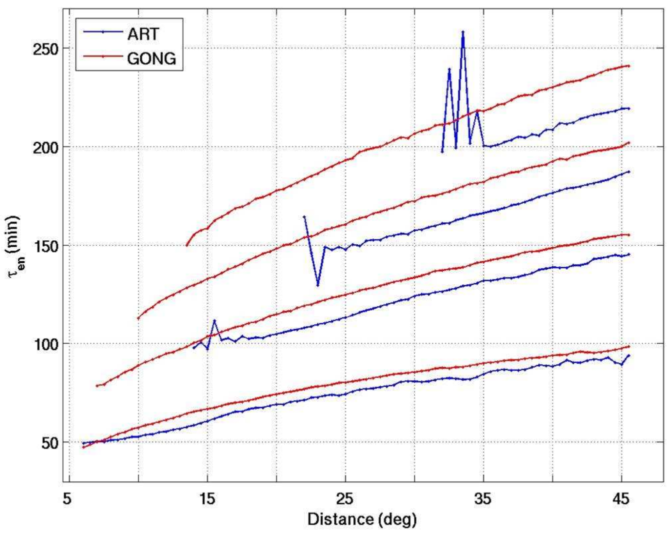

Figure B.13 Envelope (group) travel times for differing numbers of bounces; simulated or artificial data (ART) and GONG data (GONG). Due to the altered solar model, a systematic difference between the travel times associated with real and artificial data is observed. In each of the comparisons, the modes of the simulated data possess lower travel times (private communication, Olga Burtseva and Shukur Kholikov).

Appendix C

Kernels and Phase speeds

C.1 Scaling Kernels

Since it is numerically impossible to capture a delta function, we define the anomalies by the following sharply decaying functions,

$$\frac{\delta c^2}{c^2} = 0.1 \left\{ 1 - \frac{1}{1 + \exp[8.2(1-r)]} \right\}, \tag{C.1}$$

and

$$\frac{\delta a}{a} = -\left\{ 1 - \frac{1}{1 + \exp[8.9(1-\tilde{r})]} \right\}, \tag{C.2}$$

where $r = \sqrt{x^2 + y^2 + z^2}$ has units of Mm, and $(0, 0, 0)$ is the center of the perturbation (it is vertically localized at the level of the photosphere). We use the notation of Gizon & Birch (2002) to describe a source perturbation in equation (C.2), where a is the strength of the unperturbed source and the deactivated source is located around the point (x_0, y_0, z_0), with $\tilde{r} = \sqrt{(x-x_0)^2 + (y-y_0)^2}$ (units of Mm also) and $z_0 = -200$ km. Since the f mode is the diagnostic agent in this case, we assume that the anomaly is essentially 2D in nature. To transform travel-time shifts to kernel magnitudes for the sound-speed perturbation case, consider the function from equation (C.1) applied to equation (3.7). Assuming the kernel varies much slower than the perturbation, we can rewrite equation (3.7) as:

$$\delta\tau_{\mathrm{mean/diff}}(\mathbf{r}) = K_{\mathrm{mean/diff}}(\mathbf{r}, 0; \Delta) \int\int\int_{\odot} \frac{\delta c^2}{c^2}(\mathbf{r}', z) d\mathbf{r}' dz, \tag{C.3}$$

which when integrated merely becomes the finite volume of the perturbation in equation (C.1). A similar 2D area integration ($z = -200$ km) is carried out for the source perturbation. Calculating these integrals, the kernel for the sound-speed perturbation (in units of s/Mm^3) is

$$K_{\mathrm{mean/diff}}(\mathbf{r}, 0; \Delta) = 4.164\ \delta\tau_{\mathrm{mean/diff}}(\mathbf{r}), \tag{C.4}$$

and for the f-mode source kernel (in units of s/Mm^2),

$$K_{\mathrm{mean/diff}}(\mathbf{r}, 0; \Delta) = -0.3056\ \delta\tau_{\mathrm{mean/diff}}(\mathbf{r}). \tag{C.5}$$

C.2 Phase Speeds

Eleven filters of mean phase-speed v and width δv are used for different ranges of annulus radii Δ, shown in Table C.1. The first column gives the annulus index, the last column gives the center t_0 of the window function used to measure first-bounce travel times (see text).

Table C.1. Annuli and Phase-Speed Filter Parameters

index	mean Δ (Mm)	Δ (Mm)	v (km s^{-1})	δv (km s^{-1})	t_0 (min)
1	6.20	03.7, 04.95, 06.20, 07.45, 08.7	16.40	2.63	19.00
2	8.70	06.2, 07.45, 08.70, 09.95, 11.2	19.28	2.63	19.17
3	11.60	08.7, 10.15, 11.60, 13.05, 14.5	22.26	2.63	20.00
4	16.95	14.5, 15.72, 16.95, 18.17, 19.4	27.24	3.68	25.00
5	24.35	19.4, 21.87, 24.35, 26.82, 29.3	35.73	3.94	27.50
6	30.55	26.0, 28.27, 30.55, 32.82, 35.1	40.06	3.94	29.17
7	36.75	31.8, 34.27, 36.75, 39.22, 41.7	43.25	3.94	30.83
8	42.95	38.4, 40.67, 42.95, 45.22, 47.5	49.20	3.94	33.33
9	49.15	44.2, 46.67, 49.15, 51.62, 54.1	55.80	4.46	35.00
10	55.35	50.8, 53.07, 55.35, 57.62, 59.9	59.25	4.46	36.67
11	61.65	56.6, 59.12, 61.65, 64.18, 66.7	64.37	4.46	38.33

Appendix D

The scattering coefficients

D.1 Exact solution coefficients

The coefficients A_m and B_m are

$$A_m = \frac{-\left(1+\frac{\gamma}{2}\frac{a^2}{c^2}\right)\frac{k_t}{k}J'_m(k_tR)J_m(kR)+\left(1-\frac{a^2k_z^2}{\omega^2}\right)J_m(k_tR)J'_m(kR)}{\left(1+\frac{\gamma}{2}\frac{a^2}{c^2}\right)\frac{k_t}{k}J'_m(k_tR)H_m(kR)-\left(1-\frac{a^2k_z^2}{\omega^2}\right)J_m(k_tR)H'_m(kR)} \tag{D.1}$$

and

$$B_m = -\frac{2i}{\pi kR}\left[\frac{k}{k_t}\left(1+\frac{\gamma}{2}\frac{a^2}{c^2}\right)J'_m(k_tR)H_m(kR)-\frac{k^2}{k_t^2}\left(1-\frac{a^2k_z^2}{\omega^2}\right)J_m(k_tR)H'_m(kR)\right]^{-1}. \tag{D.2}$$

In equations (D.1) and (D.2), the functions J'_m and H'_m denote the first derivative of J_m and $H_m = H_m^{(1)}$ respectively.

D.2 Useful Integrals

In order to compute scattering amplitudes in the Born approximation, we used (Watson, 1944, chap. 5)

$$\int^x x' J_m^2(kx')\,dx' = \frac{x^2}{2}\left[J_m^2(kx) - J_{m-1}(kx)J_{m+1}(kx)\right] \tag{D.3}$$

and

$$\int^x x' H_m(kx') J_m(kx')\, dx' = \frac{x^2}{4}[2J_m(kx)H_m(kx) - J_{m-1}(kx)H_{m+1}(kx) - J_{m+1}(kx)H_{m-1}(kx)]. \tag{D.4}$$

D.3 Born approximation coefficients

The coefficients A_m^{Born} and C_m for the Born solution are

$$A_m^{\mathrm{Born}} = -\epsilon \frac{i\pi kR}{4} \left[\left(\gamma + 2\frac{c^2 k_z^2}{\omega^2} \right) J_m'(kR) J_m(kR) + kR J_m^2(kR) - kR J_{m-1}(kR) J_{m+1}(kR) \right] \tag{D.5}$$

and

$$\begin{aligned} C_m \;=\; & -\epsilon \frac{c^2 k^2}{\omega^2} - \epsilon \frac{i\pi kR}{4} \left(\gamma + 2\frac{c^2 k_z^2}{\omega^2} \right) J_m'(kR) H_m(kR) \\ & -\epsilon \frac{i\pi (kR)^2}{8} \left[2J_m(kR)H_m(kR) - J_{m-1}(kR)H_{m+1}(kR) - J_{m+1}(kR)H_{m-1}(kR) \right]. \end{aligned} \tag{D.6}$$

Appendix E

Eigenvalues

E.1 Jacket mode eigenvalues

The functional form of jacket modes used in our calculations is given by equation (5.11). These functions are forced to satisfy the boundary conditions,

$$\frac{\partial \Phi_J}{\partial s} + \frac{\nu^2}{m}\Phi_J = 0 \tag{E.1}$$

at $s = 1$ and $s = D$. Defining

$$N_J(\kappa_n^J, \mu, s) = \frac{1/2+\mu}{s} M_{-i\kappa_n^J,-\mu}\left(\frac{i\nu^2}{\kappa_n^J}s\right) - \frac{i\nu^2}{\kappa_n^J} M'_{-i\kappa_n^J,-\mu}\left(\frac{i\nu^2}{\kappa_n^J}s\right) - \frac{\nu^2}{m} M_{-i\kappa_n^J,-\mu}\left(\frac{i\nu^2}{\kappa_n^J}s\right), \tag{E.2}$$

and

$$D_J(\kappa_n^J, \mu, s) = -\frac{1/2+\mu}{s} M_{-i\kappa_n^J,\mu}\left(\frac{i\nu^2}{\kappa_n^J}s\right) + \frac{i\nu^2}{\kappa_n^J} M'_{-i\kappa_n^J,\mu}\left(\frac{i\nu^2}{\kappa_n^J}s\right) + \frac{\nu^2}{m} M_{-i\kappa_n^J,\mu}\left(\frac{i\nu^2}{\kappa_n^J}s\right), \tag{E.3}$$

the eigenvalues κ_n^J are determined through the relation

$$N_J(\kappa_n^J, \mu, 1) D_J(\kappa_n^J, \mu, D) = N_J(\kappa_n^J, \mu, D) D_J(\kappa_n^J, \mu, 1). \tag{E.4}$$

Subsequently, the constant η_n^J in equation (5.11) is obtained:

$$\eta_n^J = \frac{N_J(\kappa_n^J,\mu,1)}{D_J(\kappa_n^J,\mu,1)} = \frac{N_J(\kappa_n^J,\mu,D)}{D_J(\kappa_n^J,\mu,D)}. \tag{E.5}$$

E.2 p-mode eigenvalues

The functional form of p-modes, given by equation (5.9), has to satisfy

$$\frac{\partial \Phi_p}{\partial s} + \frac{\nu^2}{m}\Phi_p = 0, \tag{E.6}$$

at $s = 1, D$. Following the formulism in the appendix E.1, we define N_p, D_p as:

$$N_p(\kappa_n^p,\mu,s) = \frac{1/2+\mu}{s} M_{\kappa_n^p,-\mu}\left(\frac{\nu^2}{\kappa_n^p}s\right) - \frac{\nu^2}{\kappa_n^p} M'_{\kappa_n^p,-\mu}\left(\frac{\nu^2}{\kappa_n^p}s\right) - \frac{\nu^2}{m} M_{\kappa_n^p,-\mu}\left(\frac{\nu^2}{\kappa_n^p}s\right), \tag{E.7}$$

and

$$D_p(\kappa_n^p,\mu,s) = -\frac{1/2+\mu}{s} M_{\kappa_n^p,\mu}\left(\frac{\nu^2}{\kappa_n^p}s\right) + \frac{\nu^2}{\kappa_n^p} M'_{\kappa_n^p,\mu}\left(\frac{\nu^2}{\kappa_n^p}s\right) + \frac{\nu^2}{m} M_{\kappa_n^p,\mu}\left(\frac{i\nu^2}{\kappa_n^p}s\right), \tag{E.8}$$

and determine the eigenvalue κ_n^p and constant ζ_n^p in equation (5.9) through the following relations, respectively:

$$N_p(\kappa_n^p,\mu,1)D_p(\kappa_n^p,\mu,D) = N_p(\kappa_n^p,\mu,D)D_p(\kappa_n^p,\mu,1), \tag{E.9}$$

$$\zeta_n^p = \frac{N_p(\kappa_n^p,\mu,1)}{D_p(\kappa_n^p,\mu,1)} = \frac{N_p(\kappa_n^p,\mu,D)}{D_p(\kappa_n^p,\mu,D)}. \tag{E.10}$$

Bibliography

Barnes, G., & Cally, P. S. 2000, The Astrophysical Journal, 193, 373

Beck, J. G., Duvall, T. L., Jr., & Scherrer, P. H. 1998, Nature, 394, 653

Berland, J. et al. 2006, Computers and Fluids, 35, 1459

Belousov, S. L. 1962, Tables of Normalized Associated Legendre Polynomials, Macmillan, New York.

Birch, A. C. & Kosovichev, A. G. 2000, The Astrophysical Journal, 192, 193

Birch, A. C., Kosovichev, A. G., Price, G. H., & Schlottmann, R. B. 2001, Letters to the Astrophysical Journal, 561, L229

Birch, A. C., & Felder, G. 2004, Astrophysical Journal, 616, 1261

Birch, A. C., Kosovichev, A. G., & Duvall, T. L., Jr. 2004, The Astrophysical Journal, 608, 580

Bogdan, T. J. 1989, Astrophysical Journal, 345, 1042

Bogdan, T. J., Brown, T. M., Lites, B. W., & Thomas, J. H. 1993, ApJ, 406, 723

Bogdan, T. J., & Cally, P. S. 1995, The Astrophysical Journal, 453, 919

Braun, D. C. 1995, ApJ, 451, 859

Bogdan, T. J., Hindman, B. W., Cally, P. S., & Charbonneau, P. 1996, The Astrophysical Journal, 465, 406

Braun, D. C., Duvall, T. L., Jr., & Labonte, B. J. 1987, The Astrophysical Journal, 319L, 27B

Braun, D. C. 1995, The Astrophysical Journal, 451, 859

Cameron, R., Gizon, L., & Daifallah, K. 2007, Astronomische Nachrichten, 328, 313

Cally, P. S. 2005, Monthly Notices of the Royal Astronomical Society, 358, 353

Chou, D.-Y. & Duvall, T. L., Jr. 2000, The Astrophysical Journal, 533, 568

Christensen-Dalsgaard, J. & Berthomieu, G. 1991, in Solar interior and atmosphere, ed. Cox A. N., Livingston, W. C., & Matthews, M., (Arizona: University of Arizona Press), 401

Christensen-Dalsgaard, J. et al. 1996, Science, 272, 1286

Christensen-Dalsgaard, J. 2002, Reviews of Modern Physics, 74, 1073

Christensen-Dalsgaard, J. 2003, Lecture notes on Stellar Oscillations, (5th ed.: http://astro.phys.au.dk/∼jcd/oscilnotes/)

Colonius, T. 2004, Annual Review of Fluid Mechanics, 36, 315

Colonius, T. & Lele, S. K. 2004, Progress in Aerospace Sciences, 40, 345

Couvidat, S., Birch, A. C., Kosovichev, A. G., & Zhao, J. 2004, The Astrophysical Journal, 607, 554

Couvidat, S., Birch, A. C., & Kosovichev, A. G. 2006, 640, 516

Dahlen, F. A., Hung, S.-H., & Nolet, G. 2000, Geophysics journal international, 141, 157

Deubner, F.-L. & Gough, D. O. 1984, Annual review of astronomy and astrophysics, 22, 593

Duvall, T. L., Jr. 1982, Nature, 242, 300

Duvall, T. L., Jr., Jefferies, S. M., Harvey, J. W., & Pomerantz, M. A. 1993, Nature, 362, 430

Duvall, T. L., Jr., D'Silva, S., Jefferies, S. M., Harvey, J. W., & Schou, J. 1996, Nature, 379, 235

Duvall, T. L., Jr. et al. 1997, Solar Physics, 170, 63

Duvall, T. L., Jr. 2003, in: H. Sawaya-Lacoste (eds.), Local and global helioseismology: the present and future, Proc. SOHO 12 /GONG+ 2002 (Netherlands: ESA), p. 259

Duvall, T. L., Jr., Gizon, L., & Birch, A. C. 2006, The Astrophysical Journal, 646, 553

Fan, Y., Braun, D. C., & Chou, D.-Y., 1995, Astrophysical Journal, 451, 877

Foster, I. T., & Worley, P. H. 1997, SIAM Journal on Scientific Computation, 18, 806

Georgobiani, D., Stein, R. F., & Nordlund, Å. 2003, Astrophysical Journal, 596, 698

Giles, M. B. 1990, AIAA Journal, 28, 2050

Giles, P. M. 2000, Ph.D. Thesis, Stanford University

Gizon, L., & Birch, A. C. 2002, Astrophysical Journal, 571, 966

Gizon, L., & Birch, A. C. 2005, LRSP, 2, 6

Gizon, L., Hanasoge, S. M., & Birch, A. C. 2006, The Astrophysical Journal, 643, 549

Hanasoge, S. M. 2006, ILWS conference proceedings

Hanasoge, S. M. et al. 2006, Astrophysical Journal, 648, 1268

Hanasoge, S. M. & Duvall, T. L., Jr. 2006, proceedings of SoHo 18/Gong 2006/Helas I, p.40.1

Hanasoge, S. M., Duvall, T. L., Jr., & Couvidat, S., The Astrophysical Journal, 664, 1234

Hanasoge, S. M., Duvall, T. L., Jr. et al. 2007, IAUS, 239, 364

Hanasoge, S. M. & Duvall, T. L., Jr. 2007, Astronomische Nachrichten, 328, 319

Hanasoge, S. M., *in prep*

Hanasoge, S. M., Birch, A. C., Bogdan, T. J., & Gizon, L., *to be submitted*

Hanasoge, S. M., Couvidat, S., Rajaguru, S. P., & Birch, A. C. 2007, arXiv:0707.1369, *accepted by the Astrophysical Journal*

Hill, F. 1988, The Astrophysical Journal, 333, 996

Hu, F. Q., Hussaini, M. Y., & Manthey, J. L. 1996, Journal of Computational Physics, 124, 177

Hung, S.-H., Nolet, G., & Dahlen, F. A. 2001, Geophysics journal international, 146, 289

Jensen, J. M., Olsen, K. B., Duvall, T. L., Jacobsen, B. H., 2003, Soho 12/ Gong 12 proceedings, p.319 - 320

Jensen, J. M. & Pijpers, F. P. 2003, Astronomy & Astrophysics, 412, 257

Kosovichev, A. G., & Duvall, T. L. 1997, in ASSL Vol. 225: Solar Convection and Oscillations and their Relationship, 241

Kosovichev, A. G., Duvall, T. L., & Scherrer, P. H. 2000, Solar Physics, 192, 159

Leighton, J. W., Noyes, R. W., & Simon, G. W. 1962, Astrophysical Journal, 135, 474

Lele, S. K. 1992, Journal of Computational Physics, 103, 16

Lindsey, C. & Braun, D. C. 1997, Astrophysical Journal, 485, 895

Lindsey, C. & Braun, D. C. 2000, Science, 287, 1799

Lindsey, C., & Braun, D. C. 2004, Astrophysical Journal Supplement Series, 155, 209

Lui, C. 2003, A Numerical Investigation of Shock-Associated Noise, Ph.D thesis, Department of Mechanical Engineering, Stanford University

Miesch, M. S., Elliott, J. R., Toomre, J., Clune, T. L., Glatzmaier, G. A., Gilman, P. A. 2000, Astrophysical Journal, 532, 593

Morse, P. M., & Ingard, K. U. 1986, Theoretical Acoustics (Princeton, NJ: Princeton University Press)

Nolet, G., & Dahlen, F. A. 2000, Journal of Geophysical Reseach, 105, 19043

Orszag, S. A. 1970, Journal of Fluid Mechanics, 41, 363

Parchevsky, K. & Kosovichev, A. G. 2006, proceedings of SoHo 18/Gong 2006/Helas I, p.39.1

Poinsot, T. J. & Lele, S. K. 1992, Journal of Computational Physics, 101, 29

Rosenthal, C. S. 1995, Astrophysical Journal, 438, 434

Rosenthal, C. S. et al. 1999, Astronomy and Astrophysics, 351, 689

Scherrer, P. H. et al. 1995, Solar Physics, 162, 129

Schunker, H., Braun, D. C., Cally, P. S., & Lindsey, C. 2005, The Astrophysical Journal, 621, 149

Schrijver, C. et al., 1996, The Astrophysical Journal, 468, 921

Schüssler, M. & Rempel, M. 2005, Astronomy & Astrophysics, 441, 337

Skartlien, R. & Rast, M. P. 2000, The Astrophysical Journal, 535, 464

Shelyag, S. et al. 2006, Astrophysical Journal, 651, 576

Swisdak, M. & Zeibel, E. 1999, Astrophysical Journal, 512, 442

Thomas, J. H., Cram, L. E., & Nye, A. H. 1982, Nature, 297, 485

Thompson, K. W. 1990, Journal of Computational Physics, 89, 439

Tong, C. H. et al. 2003, Astrophysical Journal, 582, 121

Watson, B. N. 1944, A treatise on the theory of Bessel functions, 2nd ed. (New York: Cambridge University Press)

Wilson, P. R. 1980, Astrophysical Journal, 237, 1008

Woodward, M. J. 1989, Ph.D. Dissertation, Stanford University

Woodard, M. F. 1997, Astrophysical Journal, 485, 890

Whittaker, E. T., & Watson, G. N. 1980, A Course of Modern Analysis (Cambridge: Cambridge Univ. Press)

van Ballegooijen, A. A. 1986, Astrophysical Journal, 304, 828

Zhao, J.; Kosovichev, A. G. 2004, in: D. Danesy (eds.), Helio- and Asteroseismology: Towards a Golden Future, Proc. SOHO 14 /GONG 2004 (New Haven :ESA), p. 672